# Effect of Acid Strength on Spontaneous Imbibition in Calcareous and Siliceous Rocks

Muhammad Andiva Pratama[1] and Hasan Javed Khan[1]

[1]King Fahd University of Petroleum & Minerals

April 29, 2024

**Abstract**

Capillary rise experiments are conducted in a set of calcareous and siliceous rocks with varying mineralogy and petrophysical properties to understand the coupled impact of reactivity and spontaneous imbibition. A capillary rise experiment is performed in each sample: first with deionized water, then with a dilute acidic solution, and finally again with deionized water and the capillary rise profile for each is recorded. Pre- and post-acid petrophysical properties such as porosity, permeability, pore size distribution, and contact angle are measured for each sample.

The mineral makeup of the rocks significantly influences how the acidic fluids penetrate the samples. The primary reactions are the dissolution of Ca and Mg rich minerals which alter the pore network. The higher acid strength results in higher capillary rise in calcareous rocks and results in an increase in the average pore size. The same pH acid results in lower capillary rise in the siliceous rocks and a general decrease in the average pore size is observed. Changes in contact angle indicate increased water affinity in carbonate and reduced affinity in sandstone.

The link between capillary interactions and fluid reactivity is often overlooked in fluid flow studies and this research sheds light on the importance of reactivity during spontaneous imbibition, offering insights into dissolution and precipitation processes during capillary flow.

# Effect of Acid Strength on Spontaneous Imbibition in Calcareous and Siliceous Rocks

Muhammad Andiva Pratama and Hasan Javed Khan*

*Department of Petroleum Engineering, King Fahd University of Petroleum & Minerals, Eastern Province, Saudi Arabia 34464*

**Abstract**

Capillary rise experiments are conducted in a set of calcareous and siliceous rocks with varying mineralogy and petrophysical properties to understand the coupled impact of reactivity and spontaneous imbibition. A capillary rise experiment is performed in each sample: first with deionized water, then with a dilute acidic solution, and finally again with deionized water and the capillary rise profile for each is recorded. Pre- and post-acid petrophysical properties such as porosity, permeability, pore size distribution, and contact angle are measured for each sample. The mineral makeup of the rocks significantly influences how the acidic fluids penetrate the samples. The primary reactions are the dissolution of Ca and Mg rich minerals which alter the pore network. The higher acid strength results in higher capillary rise in calcareous rocks and results in an increase in the average pore size. The same pH acid results in lower capillary rise in the siliceous rocks and a general decrease in the average pore size is observed. Changes in contact angle indicate increased water affinity in carbonate and reduced affinity in sandstone. The link between capillary interactions and fluid reactivity is often overlooked in fluid flow studies and this research sheds light on the importance of reactivity during spontaneous imbibition, offering insights into dissolution and precipitation processes during capillary flow.

***Keywords*** — spontaneous imbibition; coupled reaction-imbibition; reactive imbibition; mineral dissolution;

*hasan.khan@kfupm.edu.sa

# 1 Introduction

Spontaneous imbibition is a natural occurrence within porous materials driven by fluid surface tension at the fluid-fluid interfaces (Hall and Allinson, 2010). It involves intricate molecular interactions between two fluids situated at a solid surface interface and is presented as the movement of fluids in empty spaces. It is a significant aspect of fluid dynamics (Lu and Likos, 2004) and is observed extensively during in flow in porous media, including but not limited to, hydrocarbon production in unconventional rocks Dehghanpour et al. (2013); Abd et al. (2019); Zhou et al. (2023), solute transport in the vadose zone (Kuhlman et al., 2022; Zahasky and Benson, 2022), CO2 storage (Zahasky and Benson, 2019; Haghi et al., 2021), and ink wicking on paper during inkjet printing (Aslannejad et al., 2017; Yin et al., 2018). Multiple factors influence spontaneous imbibition including fluid properties such as surface tension and density, the contact angle formed at the solid-liquid interface, and the cross-sectional area open to flow (Mason and Morrow, 2013). In a porous medium, the last is analogous to the size of the pore openings (Boduroglu and Bashir, 2022).

The main driver of the fluid during spontaneous imbibition is the capillary forces, which is related to the surface tension/energy, and the resistive force is the viscous force (Mason and Morrow, 2013). The earliest and simplest analytical solution that successfully characterized the capillary rise behavior were separately found by Lucas (1918) and Washburn (1921). These solutions were for a vertical capillary tube with a constant cross-sectional area and without the impact of gravity. A power law relationship was observed between the capillary height and the time, which is represented by the Lucas-Washburn equation (L-W equation):

$$x = \sqrt{\frac{r\sigma\cos\theta}{2\mu} \cdot t} \tag{1}$$

where $x$ is the capillary height $(m)$, $r$ is the pore radius $(m)$, $\sigma$ is the surface tension between the fluid-air interface *(N/m)*, $\theta$ is the contact angle $(^\circ)$, $\mu$ is the viscosity of the fluid $(Pa.s)$, and $t$ is the time $(s)$.

Over time, the L-W equation have been found to be insufficient to model spontaneous

imbibition in porous and permeable medium and different models have been proposed to overcome the specific issues including, but not limited to, addition of gravity force, non-constant cross-sectional area, inclined capillary tubes, and tortousity (Benavente et al., 2002; Fries and Dreyer, 2008a; Tsunazawa et al., 2016; Villagrán Zaccardi et al., 2018; Wang et al., 2022).

While spontaneous imbibition has been extensively studied, there is limited research focused on the reactivity occurring during spontaneous imbibition processes. In contrast, forced imbibition processes involving reactive fluids have been thoroughly observed and modeled. From an experimental perspective, studies have been conducted using reactive fluids in imbibition experiments. For example, Fan et al. (2018) observed that the increase in total dissolved solids resulting from the chemical leaching of brine-dissolved salts could mobilize hazardous radionuclides like radium. Similar to the imbibition process, chemical and biological leaching has also been extensively studied in the context of heavy metal extraction, metal-contaminated environments, and radionuclide-contaminated soils and rocks (Vachon et al., 1994; Avvaru et al., 2008; Bhargava et al., 2015; Córdoba et al., 2009). In the realm of modeling, extensive research has explored various techniques to simulate reactive imbibition processes. For instance, Li et al. (2020) developed a model to capture mineral dissolution and precipitation in shale matrices resulting from acidic hydraulic fracturing fluid imbibition. Meanwhile, Di Donato and Blunt (2004) utilized both analytical and numerical simulations to observe countercurrent imbibition during reactive flow and transport in fractured rocks.

In a previous study (Pratama and Khan, 2024), we studied the impact of fluid reactivity on spontaneous imbibition in calcareous rock samples by conducting a series of capillary rise experiments using deionized (DI) water and diluted HCl at pH 2 and tracking the capillary movement and the evolution of the rock's petrophysical properties. Here we extend the work by employing a combined experimental and modeling approach to investigate how fluid reactivity influences spontaneous imbibition in both carbonate and sandstone formations at different acid strength. We conduct capillary rise experiments using DI water and diluted HCl acid at two pH levels (2 and 4) and observe changes in the petrophysical properties before and after the acid-induced capillary rise as well as the physicochemical changes in the fluid resulting from the reactive interaction be-

tween the rocks and the fluid. Finally, we fit the capillary rise profiles using an extended Lucas-Washburn equation based on the Tsunazawa et al. (2016) model. Connecting capillary interactions with fluid reactivity is frequently overlooked in fluid transport analysis. This research presents new insights on the significance of reactivity concerning spontaneous imbibition timescales as this is crucial for understanding the movement of reactive contaminants through the vadose zone.

# 2 Methodology

## 2.1 Experimental methods

**Sample preparation and petrophysical characterization** Six cylindrical core samples, each measuring 3.8 cm in diameter and 7.6 cm in length, are extracted from different carbonate and sandstone blocks exhibiting diverse petrophysical properties. They are individually labeled according to their formation and the expected permeability value provided by the supplier. *AU* for Austin Chalk, *IL* for Indiana Limestone, *SC* for Sciotto Sandstones, *BB* for Berea Buff, and *BG* for Bandera Gray.

Surface x-ray diffraction (SXRD) is conducted for each sample to determine the mineralogy of the rock surface (Table 1). SXRD is used rather than bulk XRD, which is performed on a powder, to get a more representative mineralogy. All of the carbonate samples exhibit notably high calcite content. In contrast, the composition of the three sandstone samples varies with quartz content between 58 – 98% and the rest mostly feldspar and mica. SC and BB are categorized as pure-quartz sandstones, while BG displays a dolomite composition.

The standard petrophysical properties (porosity, permeability, contact angle, and pore size distribution) are measured twice for each sample: before and after an acid-based capillary rise experiment. Porosity is assessed via a helium porosimeter, liquid permeability using DI water injection, contact angle in a water-rock-air system via the sessile drop method, and pore size distribution via NMR $T_2$ relaxation time measured on a Geospec benchtop rock core analyzer. Each measurement is repeated for consistency, with the

**Table 1.** Mineral compositions for each core samples used in this study based on surface x-ray diffraction (SXRD) analysis.

| Sample Name | Mineral Composition (%) | | | | | | | |
|---|---|---|---|---|---|---|---|---|
| | Calcite | Dolomite | Quartz | Halite | Microcline | Orthoclase | Albite | Muscovite |
| AU | 99.9 | - | 0.1 | - | - | - | - | - |
| IL100 | 100.0 | - | - | - | - | - | - | - |
| IL2 | 100.0 | - | - | - | - | - | - | - |
| SC | - | - | 87.1 | - | - | 4.0 | 6.0 | 2.9 |
| BB | - | - | 97.8 | 0.1 | 1.4 | - | - | - |
| BG | - | 20.5 | 58.6 | - | - | - | 8.4 | 12.4 |

contact angle tested three times on different spots of the same rock surface. The $T_2$ relaxation time, reflecting $H^+$ relaxation in magnetic resonance and proportional to pore size, is estimated using an equation assuming spherical pores (Jaeger et al., 2009):

$$\frac{1}{T_2} = \rho_s \frac{S}{V} = \rho_s \frac{3}{r} \tag{2}$$

where $T_2$ is the spin-spin relaxation time ($\mu s$), $\rho_s$ is the surface relaxivity ($\mu s/s$), $S$ is the individual pore surface area ($m^2$), $V$ is the individual pore volume ($m^3$), $\phi$ is the porosity, and $r$ is the pore radius ($\mu m$).

Separately, two acidic solution was prepared by titrating 12M HCl with deionized (DI) water to get a dilute pH 2 and 4 solution. DI water was used as the baseline fluid.

**Capillary Rise** The capillary rise experiment involves two beakers of different sizes (2 L and 100 ml) connected by a siphon (Figure 1a). The larger beaker is open at the top while the smaller beaker has an aluminum wire mesh placed on the top. Initially, the smaller beaker is empty and the larger beaker is full. Water is siphoned from the larger beaker and flows into the smaller beaker where the fluid level rises. Once the fluid level reaches the top, it passes through the wire mesh and spills over whilst maintaining a constant level at the top of the small beaker. This system will continue until the water level in the larger beaker becomes equal to the height of the smaller beaker, which has

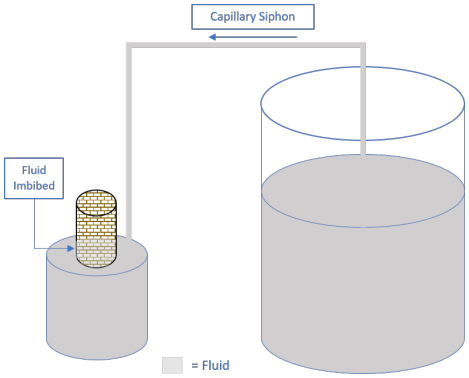


**(a)** Capillary rise experiment schematic

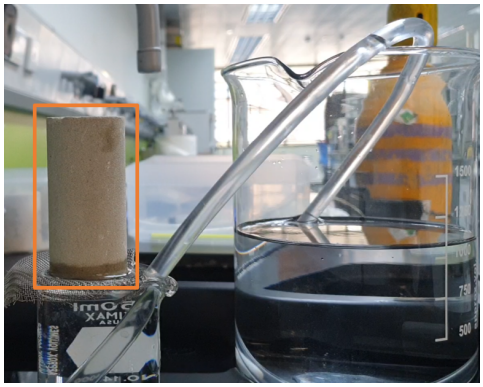

**(b)** Capillary rise experiment setup

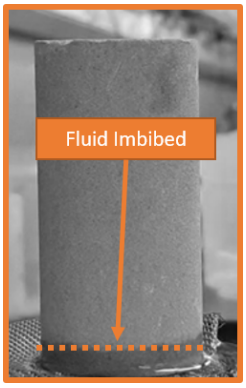


**(c)** Fluid imbibing in the core

**Figure 1.** (a) Schematic representation of the capillary rise experiments. (b) Actual setup for the capillary rise experiment, comprising the larger and smaller beakers, the siphon, the aluminum wire mesh, and the core sample. (c) A grayscale image example showing fluid imbibition in the BG core sample. Fluid height was indicated by varying intensity of colors.

been calculated to take ∼35 minutes.

An oven-dried core sample is placed on top of the wire mesh and the siphon is started (Figure 1b). The water level rises in the beaker until it interacts with the rock sample at a constant fluid-rock interface and starts imbibing into the rock. These experiments are conducted at room temperature and pressure conditions and use air as the displaced fluid.

The imbibition process' capillary height is monitored continuously for 800 seconds using a Samsung Galaxy Note 9 camera equipped with a 12.2 MP ISOCELL 2L3 (SAK2L3) sensor and a resolution of 1920 x 1080 at 30 frames per second. The timescale was selected based on the resolution limitations of the image acquisition instrument and the

observation that the rate of fluid height increment slows down. As the fluid imbibes through the rock and the water saturation changes, a distinct change in color is observed which is captured by the camera (Figure 1c). A custom MATLAB script is utilized to calculate the capillary height by analyzing the differences in color saturation in the video data (Matlab, 2022). Initially, the video is imported as a 3D RGB image stack (spatial dimensions x-y and time dimension) and the central part of the core (a row of 30 pixels forming a rectangle at the respective core height) is isolated for further image analysis. The center of the core is selected due to its minimal curvature within the observation window. A limitation of this method is that the capillary height is measured at only face and assumes the capillary front to be equal spatially, which is usually not the case in porous media (Bartels et al., 2019; Khan et al., 2020).

Subsequently, the RGB image is separated into the individual color channels and the channel (blue) with the most significant contrast between the dry and saturated zones is identified and used for subsequent image analysis. To mitigate contrast inconsistencies caused by external factors like shadows or background movements, the image is initially corrected. Following this correction, global segmentation is performed, with the transition zone's boundary indicating the imbibition front. The capillary height is calculated by taking the difference between the imbibition front and the fluid-rock interface. By comparing the physical length of the sample and the number of pixels it occupies in the image, the pixel size is calculated as 0.15 mm. By analyzing the image stack, the script tracks the temporal evolution of the imbibition front over time, generating a representation of how the capillary rise progresses over time.

The capillary rise experiments are performed in the following sequence. First three repetitions of the capillary rise with DI water is performed. Then the dilute acidic solution (pH 2 or pH 4) is used as the imbibition phase. Finally, another three repetition of the capillary rise with DI water are performed. Following each capillary rise experiment, the mass of the sample is measured, it is then oven dried at 75 °C for 12 hours, and the mass measured again.

**Fluid interaction with the rocks** Due to the reactivity of the acidic DI water, the fluid is expected to undergo physicochemical alterations during the imbibition experi-

ment. But considering the small volume of fluid imbibed during the experiment, the fluid couldn't be extracted from the rock without contamination. Therefore, a separate set of samples were tested in a batch reactor by interacting them with the acidic fluid (pH 2 and pH 4) and the base fluid (pH 7).

Six sets of 15 ml solutions of diluted HCl (pH 2 and 4) and DI water (pH 7) each were prepared and a 1.5 g chip of each sample was introduced to each solution. The solution was allowed to react for 20 minutes and then a fluid sample is collected. To remove any solids from the collected fluid sample, it was passed through a 20-micron filter. Optical emission spectrometry (ICP-OES) was then performed on each reacted and unreacted sample to determine the chemical evolution of the fluid.

## 2.2 Model fitting

**Fitting Process** Experimental capillary rise data was fit to three different spontaneous imbibition models: Lucas-Washburn (L-W) equation (Washburn, 1921) (Eq. 1), Tsunazawa et al. (2016) model (Eq. 3a), and the Quéré equation (Quéré, 1997) (Eq. 3b). Both L-W and Quéré models were selected for their distinct height-time relationships: the former illustrating a logarithmic correlation while the latter shows a linear correlation. Although Tsunazawa's model shows a trend similar to the L-W equation, it further incorporates the gravity force and considers the complexity of the pore structure through tortuosity. Further details about these models can be found in Pratama and Khan (2024).

$$t(x) = -\frac{8\mu\tau}{r^2\rho g}x - \frac{16\sigma \cdot \tau^2 cos(\theta)}{r^3\rho^2\ g^2} log\left(1 - \frac{r\rho g}{2\sigma cos\theta}x\right) \tag{3a}$$

$$h = \sqrt{\frac{2\sigma cos\theta}{\rho R}} \cdot t \tag{3b}$$

where $\rho$ is the fluid density ($kg/m^3$), $\tau$ is the tortuosity, and $g$ is the gravitational acceleration ($m/s^2$).

To perform the fitting, the petrophysical properties of the rock samples served as the fitting parameter: pore size for both the L-W equation (Eq. 1) and the Quéré equation

(Eq. 3b), and pore size along with tortuosity for the Tsunazawa model (Eq. 3a). All the other parameters were derived from laboratory measurements. The resulting fit parameters were then compared between pre-reaction, acid, and post-reaction conditions.

**Flow Regime Analysis** The purely inertial flow is represented by the Quéré (1997) equation (Eq. 3b) as it only considers inertial forces. For the viscous flow, the L-W equation (Washburn, 1921) (Eq. 1) was used. Based on these two equations, Ichikawa and Satoda (1994) determined the flow regime based on the gradient of the dimensionless height and time (Eq. 4) to incorporate the effect of the gas-liquid interface dynamics along the capillary force. The early stage of the capillary rise, which exhibits as a higher gradient, displays purely inertial flow whereas the latter shows purely viscous flow.

$$t^* = \frac{8\mu t}{\rho r^2} \tag{4a}$$

$$h^* = \sqrt{\frac{16\mu^2 h^2}{\rho r^3 \sigma cos\theta}} \tag{4b}$$

# 3 Results and Discussion

## 3.1 Capillary rise

Due to the differences in the initial petrophysical properties for each rock, the capillary rise profile and the maximum height achieved are different after 800 seconds (Figure 2 and 3). Regardless of mineralogy and pH variations, a consistent logarithmic curve shape was observed across all experiments. This aligns with both the L-W and Tsunazawa's models, indicating that capillary height demonstrates a logarithmic relationship with time and a linear relationship with the square root of time ($\sqrt{t}$). In the carbonate sample, AU exhibited the highest capillary height among the samples, reaching a maximum of 20 mm at pH 2 and 28 mm at pH 4, while IL2 displayed the lowest final capillary height for the pre-reaction experiment. Interestingly, within the IL100 sample, distinct behaviors

were observed between the samples used in pH 2 and pH 4 experiments. The pH 2 sample didn't even reach 10 mm, whereas the pH 4 sample showed a significantly higher height. This discrepancy can be attributed to a substantial difference in permeability (Table 2). In sandstones, akin to the carbonates, contrasting behaviors were observed in each sample. BB demonstrated the highest final capillary height, whereas SC and BG exhibited similar final capillary heights, lower than BB. All the samples used for both pH conditions exhibit similar profiles and reach the relatively same final capillary height.

A point to note is that the capillary front measured here is based on one face of the sample only. Generally no changes were observed on the other sides, but nevertheless the height was not exactly the same. Furthermore, this method does not show the fluid level inside the core and therefore assumes that the fluid front is constant across the cross-section.

**Acid-based Capillary Rise** In carbonates, generally, the acid-based final capillary height was found to be greater than the initial water capillary height but with a similar shape. In the pH 2 case, for IL100, it was consistently higher whereas for the other two samples, it was initially lower but increased at a faster rate than with the DI water. The point of crossing, i.e. the time at which the acid capillary rise is equal to the DI water capillary rise, is found to be longer in IL2 ($\sim$530 seconds) compared to AU ($\sim$280 seconds).

In higher pH conditions, the final capillary height post-acid reaction generally exceeded the initial water capillary height, except for AU, which displayed a lower height. However, despite this elevation in higher pH, the incremental change in final height was not as substantial as observed in lower pH environments.

Apart from the maximum capillary height, the rate of capillary rise during the acid-based experiments also differed from that observed during the water-based capillary rise. Lower pH levels exhibited a pattern where the capillary rate was initially slower, gradually increasing to eventually surpass the water capillary height. Conversely, in higher pH conditions, the capillary rate remained consistently lower. This resulted in a reduced increment of capillary height in IL100 and IL2 and an overall lower capillary height in AU.

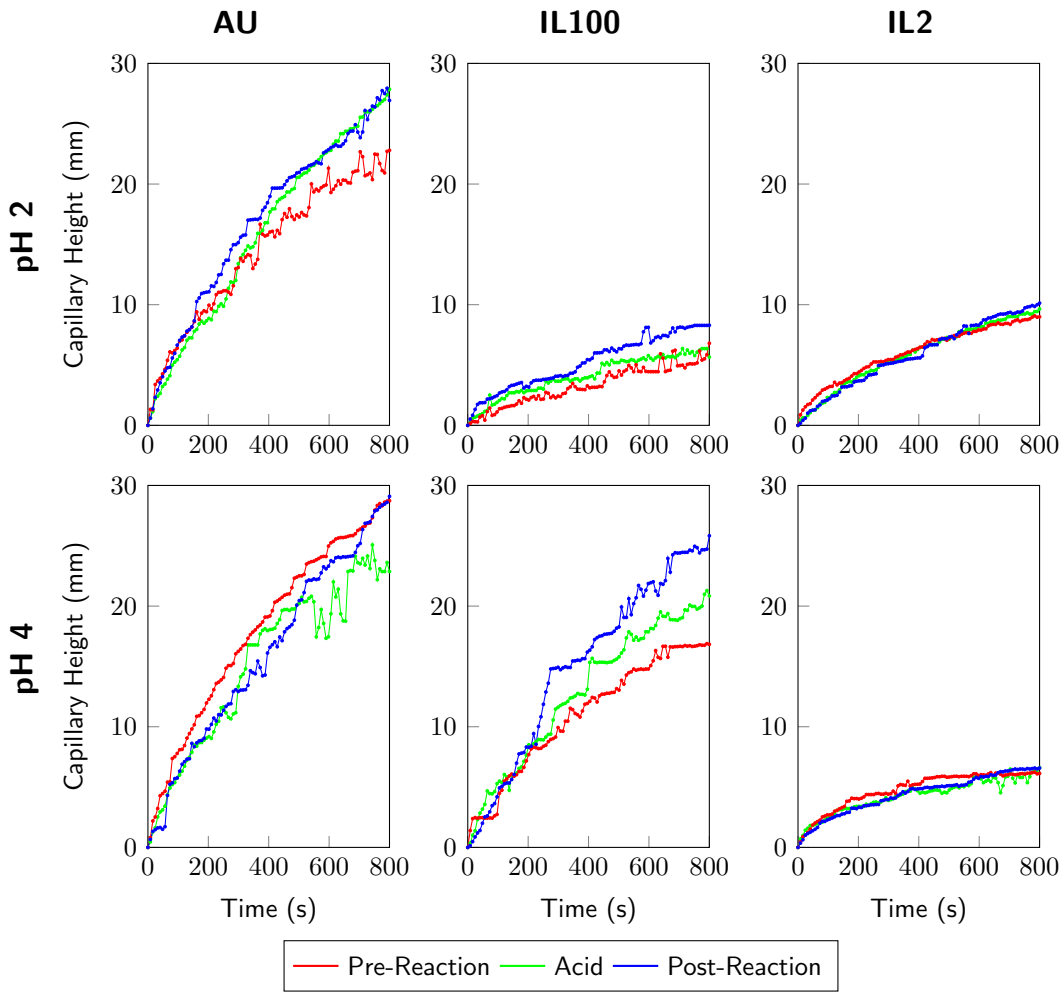


**Figure 2.** The comparison of the capillary height (time-dependent) in every carbonate core sample for each condition. The pre- and post-reaction are the capillary height observed through the DI water-based capillary rise experiment before and after the acid-based capillary rise experiment. Acid was the capillary height that was observed in acid-based capillary height.

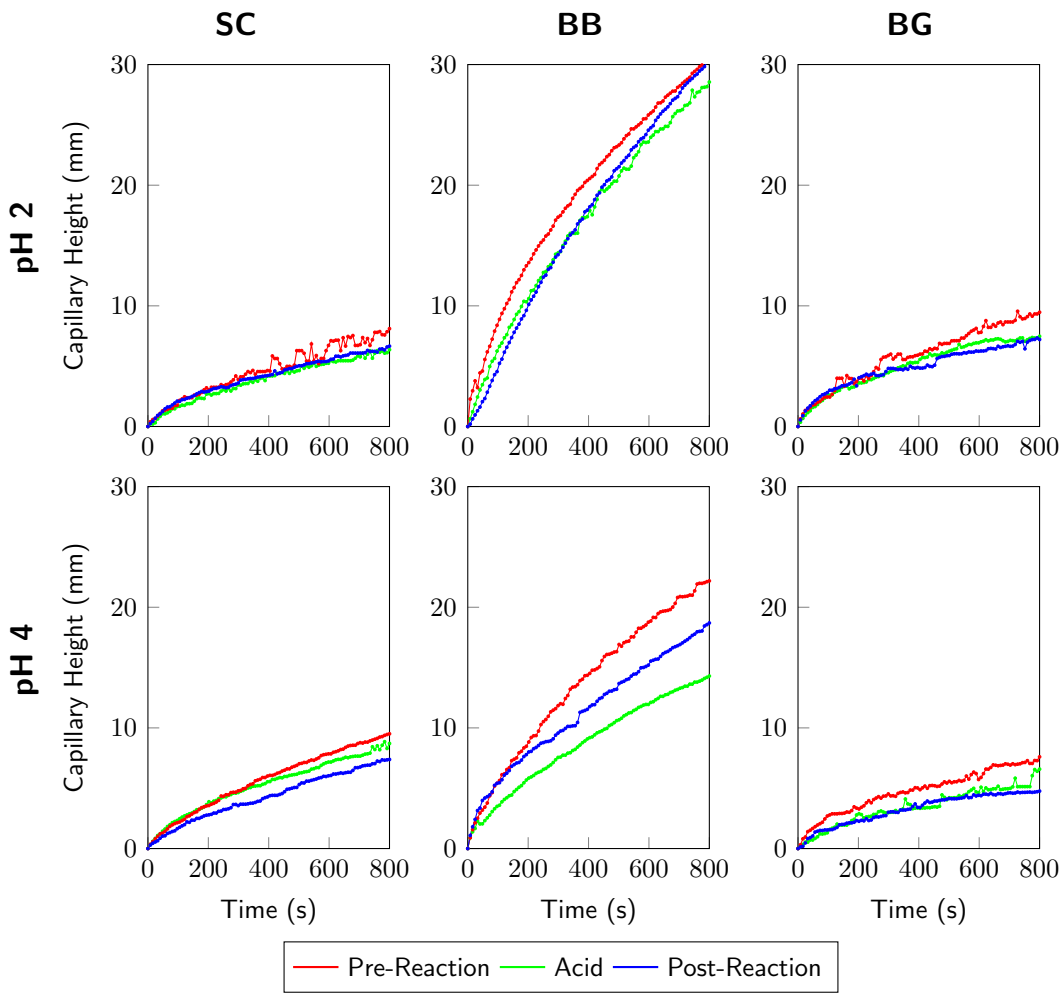


**Figure 3.** The comparison of the capillary height (time-dependent) in every sandstone sample for each condition. The pre- and post reaction was the capillary height observed through the DI water-based capillary rise experiment before and after the acid-based capillary rise experiment. Acid was the capillary height that was observed in acid-based capillary height.

In sandstones, conversely, the acid-based final capillary height is consistently lower than the pre-reaction water capillary height (Figure 3). It was observed that the acid capillary height does not surpass the initial water capillary height within the experimental time frame.

In higher pH, the decrease is more significant than the lower pH. The highest decrease relative to the water capillary height was observed in BB, as the acid final capillary height is reduced by more than 30 %, followed by BG and SC. Since the main parameters that driven the capillary rate is contact angle and pore size, the acid able to modify these two parameters and leads to lower capillary height.

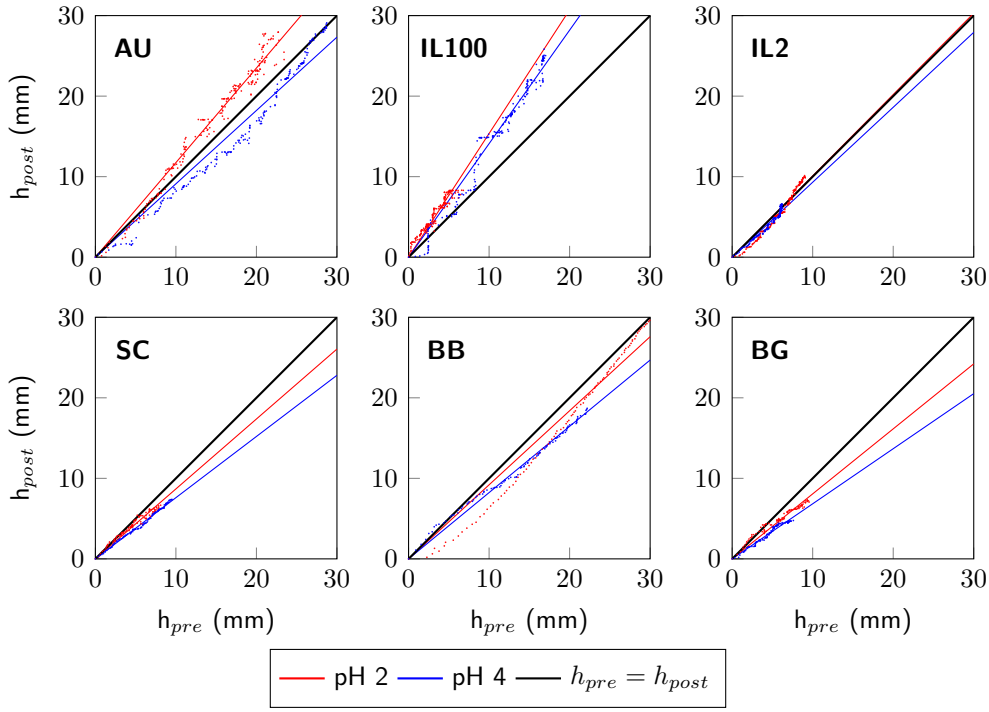


**Figure 4.** Comparison of the water capillary height before and after the acid imbibition for each core sample and for both acidic conditions. The black line indicates $h_{pre} = h_{post}$. Lines which lie above this line indicate that post-reaction capillary rise was higher than the pre-reaction capillary rise.

**Effect of Acid on the Water Capillary Height** The interaction between the acid and rock caused changes in the pore network and structure, which, in turn, could also affect the water's capillary rise. The interpolation illustrating the correlation between the water capillary heights before and after acid imbibition is depicted in Figure 4. In carbonates, for both pH levels, the most prominent change is observed in IL100, where the post-reaction maximum capillary height is ∼50 % higher than the pre-reaction and the post-reaction has a consistently higher height. AU initially shows the same height for pre- and post-reaction, but it got separated in the later stages and the post-reaction shows significantly higher end-point capillary height.

In carbonate samples, the pH notably influences the correlation between pre- and post-reaction water capillary rise. Across all three samples, a trend emerges: at lower pH levels, the post-reaction water capillary height consistently surpasses the pre-reaction level. This is visually evident as the red line consistently lies above the black line, which is the unity gradient line. Conversely at higher pH, more diverse behavior was observed. In the cases of AU and IL2, the post-reaction water capillary rise was lower than the pre-reaction rise. However, in the case of IL100, the post-reaction water capillary rise remained higher than the pre-reaction rise. Despite these variation, a consistent behavior emerged across the samples: a higher pH exhibits a lower gradient and a lower pH exhibits a higher gradient.

In sandstones, a distinct behavior was observed, as for all of the acidic conditions, the post-reaction water capillary height was lower than the pre-reaction water capillary rise. The reduction was observed to be the highest in BG sample, followed by SC and BB. Not only the final height, the water capillary rise profile was also changed. In the AU sample, the water capillary rise profile was shown to be lower than the pre-reaction water capillary rise at the beginning, but at some time, it will overlap and get higher than the pre-reaction one. The same thing happened with the IL2 sample, but the overlapping point is much later compared to the AU sample. Overall, all of the samples showed a consistent behavior, a higher end-point capillary height compared to the water pre-reaction capillary height. For the higher pH, the overlapping point happened later than in the lower pH. However, the overlap is not observed in the sandstone cases, as from the beginning, the profile was distinct from each other.

## 3.2 Petrophysical properties alteration

The petrophysical properties (porosity, permeability, contact angle, and pore size distribution) and mass for all the samples are observed to change due to the effect of the reaction with acid during the acid-based spontaneous imbibition process. Since these measurements were done on the actual samples before and after reaction, it is possible that a little mass was lost during the loading/unloading of the sample from the porosimeter and liquid permeameter.

**Mass and porosity** Although not statistically significant, comparing the core sample's mass and porosity before and after the acid reaction was nonetheless significant. The mass and porosity have a direct relationship: the mass decreases as the void areas inside the core samples grow and the comparison of it is shown in Table 2.

Small changes in the mass and porosity are expected as the fluid is only permeating to a maximum of 30 mm. Considering the case of SC at pH 2, the maximum fluid height attained is 10 mm (Figure 3). So assuming a 1% change in the porosity throughout the imbibed zone, the change in the porosity for the whole rock sample will only be 0.13%.

For low pH, consistent mass reduction was observed across all carbonate samples. AU exhibited the maximum mass decrease, while IL2 showed the lowest reduction. The average reduction across all samples was less than one percent (%), not exceeding 1.6 g. As mass directly correlates with porosity, this validates the increment in porosity. All carbonate samples experienced increased porosity, with AU demonstrating the highest change (0.73 %) and IL2 the smallest (0.15 %). None of the samples showed a significantly large change; all were under 1 %.

Interestingly, at higher pH, variations emerged within the carbonate samples. AU still experienced mass reduction, albeit smaller than in the low pH environment (0.3 g). Both IL100 and IL2 showed a marginal increase in mass (around 0.1 g). However, all samples displayed an increase in porosity, with IL2 exhibiting the highest increment (0.17 %).

In sandstones, akin to the carbonate samples, mass reduction was observed across all samples. BG exhibited the highest mass reduction, followed by BB and SC. However,

**Table 2.** Petrophysical properties comparison between pre- and post-acid reaction including the error of the measurement. Each sample experienced changes in the pore scale and opening up of pore spaces, shown by the reduction of mass and increment of the porosity, while the permeability is increased in most of the samples, and reduced in IL30.

| **Property** | **pH** | **Condition** | **Sample Name** | | | | | |
|---|---|---|---|---|---|---|---|---|
| | | | **AU** | **IL100** | **IL2** | **SC** | **BB** | **BG** |
| **Mass (g)** | **2** | Pre- | 161.78 ± 0.01 | 188.42 ± 0.01 | 185.74 ± 0.01 | 180.81 ± 0.01 | 182.14 ± 0.01 | 188.01 ± 0.01 |
| | | Post- | 160.27 ± 0.01 | 187.91 ± 0.01 | 185.45 ± 0.01 | 180.72 ± 0.01 | 181.80 ± 0.01 | 187.46 ± 0.01 |
| | **4** | Pre- | 161.92 ± 0.01 | 195.60 ± 0.01 | 185.61 ± 0.01 | 180.60 ± 0.01 | 180.81 ± 0.01 | 205.3 ± 0.01 |
| | | Post- | 161.61 ± 0.01 | 195.71 ± 0.01 | 185.71 ± 0.01 | 180.65 ± 0.01 | 180.67 ± 0.01 | 205.59 ± 0.01 |
| **Porosity (%)** | **2** | Pre- | 27.51 ± 0.10 | 16.05 ± 0.10 | 17.11 ± 0.05 | 17.82 ± 0.10 | 22.12 ± 0.10 | 21.68 ± 0.05 |
| | | Post- | 28.30 ± 0.06 | 16.23 ± 0.03 | 17.26 ± 0.06 | 17.80 ± 0.06 | 22.38 ± 0.03 | 22.39 ± 0.06 |
| | **4** | Pre- | 28.80 ± 0.10 | 15.54 ± 0.10 | 17.22 ± 0.05 | 18.68 ± 0.10 | 21.10 ± 0.10 | 14.32 ± 0.05 |
| | | Post- | 29.07 ± 0.06 | 15.66 ± 0.03 | 17.39 ± 0.06 | 19.46 ± 0.06 | 21.79 ± 0.03 | 14.61 ± 0.06 |
| **Permeability (mD)** | **2** | Pre- | 41.15 ± 0.15 | 3.80 ± 0.70 | 33.82 ± 0.25 | 4.38 ± 0.15 | 63.72 ± 0.70 | 11.94 ± 0.25 |
| | | Post- | 45.27 ± 0.10 | 5.59 ± 0.01 | 30.67 ± 0.10 | 4.97 ± 0.10 | 119.22 ± 0.01 | 13.43 ± 0.10 |
| | **4** | Pre- | 28.34 ± 0.15 | 289.60 ± 0.70 | 31.87 ± 0.25 | 4.37 ± 0.15 | 256.67 ± 0.70 | 14.88 ± 0.25 |
| | | Post- | 49.34 ± 0.10 | 85.78 ± 0.01 | 31.66 ± 0.10 | 9.05 ± 0.10 | 28.74 ± 0.01 | 24.83 ± 0.10 |

these reductions were relatively insignificant, none surpassing 0.6 g. Notably, porosity did not directly correlate with mass reduction, as SC showed reduced porosity while BB and BG displayed increments. BG showed the largest change, with a porosity increase of 0.71 %. This change was nearly as high as the highest increment in carbonate samples (AU with 0.73 %). This occurrence might be attributed to reactive minerals in the BG samples, potentially driving mineral dissolution as explained in the subsequent subsection.

At higher pH, variations in mass changes persisted. SC and BG exhibited mass increments, while BB showed mass reduction. Intriguingly, all sandstone samples displayed increased porosity. SC exhibited the largest porosity increment (0.78 %), followed by BB (0.69 %) and BG (0.31 %).

**Permeability** The alteration in permeability exhibited distinct behaviors. Most of the carbonate samples at lower pH exhibited increased permeability due to the acid reaction (Table 2). However, a noticeable and significant drop in permeability (4.6 mD or -13.3 %) occurred in IL2. AU displayed a permeability change of 3.8 mD (or +9.2 %) while IL100 showed an increase of 1.1 mD (or +24.4 %). Although the absolute change in IL100 was lower than the others, the relative changes was the highest among all. At higher pH, only the AU sample experienced an increase in permeability, whereas IL100 and IL2 showed a drop. Notably, a substantial decrease was observed in IL100 with post-reacted permeability reaching only 30% of the initial permeability, or a drop of ∼30%.

In sandstones at lower pH, all samples exhibited permeability increments. BB displayed the highest change at 55.5 mD (or +87.1 %), followed by BG with 1.49 mD (or +12.5 %) and SC with 0.59 mD (or +13.5 %). Similarly at higher pH, most samples exhibited increased permeability except for BB, which displayed a significant reduction (a decrease of 227.9 mD or -88.8 %). For SC and BG, the increments were higher compared to the lower pH samples.

The comparison between pre- and post-reaction permeability are plotted on a log-log plot to assess deviations from the line $k_{pre} = k_{post}$ (Figure 5). Points lying above the unity gradient line (black) indicate samples where the permeability has increased as a result of the acid imbibition, whereas points lying below the unity gradient line indicate

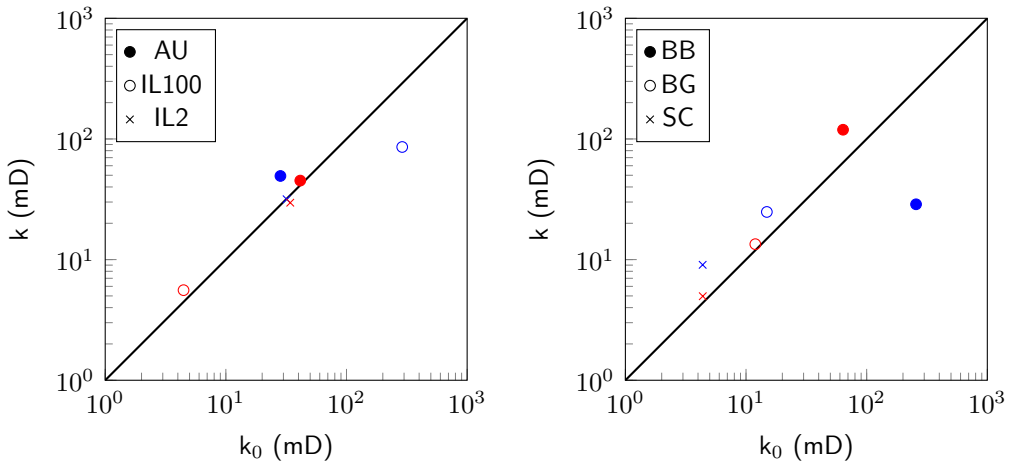


**(a)** Carbonates **(b)** Sandstones

**Figure 5.** Comparison of permeability before and after acid imbibition at pH 2 (red) and pH 4 (blue). The black line is the unity gradient line. Point lying north of the unity gradient line indicate that the permeability has increased after the acid imbibition.

samples where the permeability has decreasesd as a result of the acid imbibition. In carbonate samples, most values did not significantly deviate from the unity gradient line, indicating relatively insignificant changes (Figure 5a). Only in IL100 at pH 2 was there a high deviation. Additionally, higher pH conditions showed more significant deviations compared to lower pH.

Conversely, sandstones displayed more scattered and deviated permeability results (Figure 5b). The correlation between pH and permeability changes was notably clearer in sandstones, where higher pH (blue) induced greater permeability alterations. BB exhibited the most significant permeability alteration amongst the sandstone samples.

**Pore Size Distribution** The pore size distribution was estimated based on the distribution of $T_2$ relaxation time (Equation 2). The surface relaxivities are highly dependent on the magnetic impurities present inside the rock, but since none of these samples showed any sizeable quantity of the magnetic impurity (Table 1), the surface relaxivity found in the literature are utilized: 39.65 $\mu$m/s for Indiana Limestone (IL) (Lawal et al., 2020), 23.3 $\mu$m/s for Austin Chalk (AU) (Benavides et al., 2020), 29.6 $\mu$m/s for Sciotto Sandstone (SC) (Mitchell and Fordham, 2014), 65 $\mu$m/s for Bandera Gray (BG) (Lucas-Oliveira et al., 2020), and 21 $\mu$m/s for Berea Buff (BB) (Lucas-Oliveira et al., 2020).

Two phenomena were observed through the pore size distribution comparison: pore enlargement (increment in the mean of the distribution) and pore size reduction in the larger pore sizes (Figures 6 and 7). A slight variation was observed in the changes in the mean pore size distribution. As explained previously, the changes expected in the samples are small since the imbibed zone is considerably small. In some instances it is only ∼13% of the total length of the rock sample.

At lower pH, an increase in the mean of the distribution was observed in IL100 (from 14.98 to 15.68 $\mu$m) and AU (from 3.57 to 3.69 $\mu$m), while a reduction was observed in IL2 (from 15.35 to 14.53 $\mu$m). The largest pore spaces in each sample were notably reduced. This strongly indicates simultaneous dissolution and precipitation occurring in different parts of the pore systems. Alterations were also observed in smaller pore spaces, with new pore spaces generated, leading to an expanded distribution within the smaller pores.

In higher pH, the most notable observation was the shift of the plot to the right, indicating the enlargement of pore spaces and it is consistently observed across all carbonate samples. Unlike the lower pH observations, there was no clear reduction observed in large pore spaces, suggesting a lack of pore size reduction. However, in smaller pore sizes, reductions were observed, indicating that mineral dissolution could occur at both lower and higher pH, while mineral precipitation was observed only at lower pH.

In sandstones at lower pH, the overall distribution shifted to the left for all samples. The most notable shift occurred in SC, followed by BG and BB. Changes were also observed in smaller pore sizes. In the micropore system ($< 10^{-1}\mu$m), an increase in the number of pores was noted, while in the mesopore system (between $10^{-1}\mu$m and $10^{0}\mu$m), a reduction in the number of pores was observed. This suggests ongoing mineral dissolution, albeit less prominent compared to carbonate. Additionally, factors such as mineral precipitation or clay swelling might contribute to the reduction in pore sizes.

At higher pH, a contrasting pattern emerged. The pore size distribution shifted to the right, indicating pore enlargement across all sandstone samples. Unlike lower pH conditions, in smaller pore sizes, the number of pores decreased, signifying the enlargement of pores interacting with fluids.

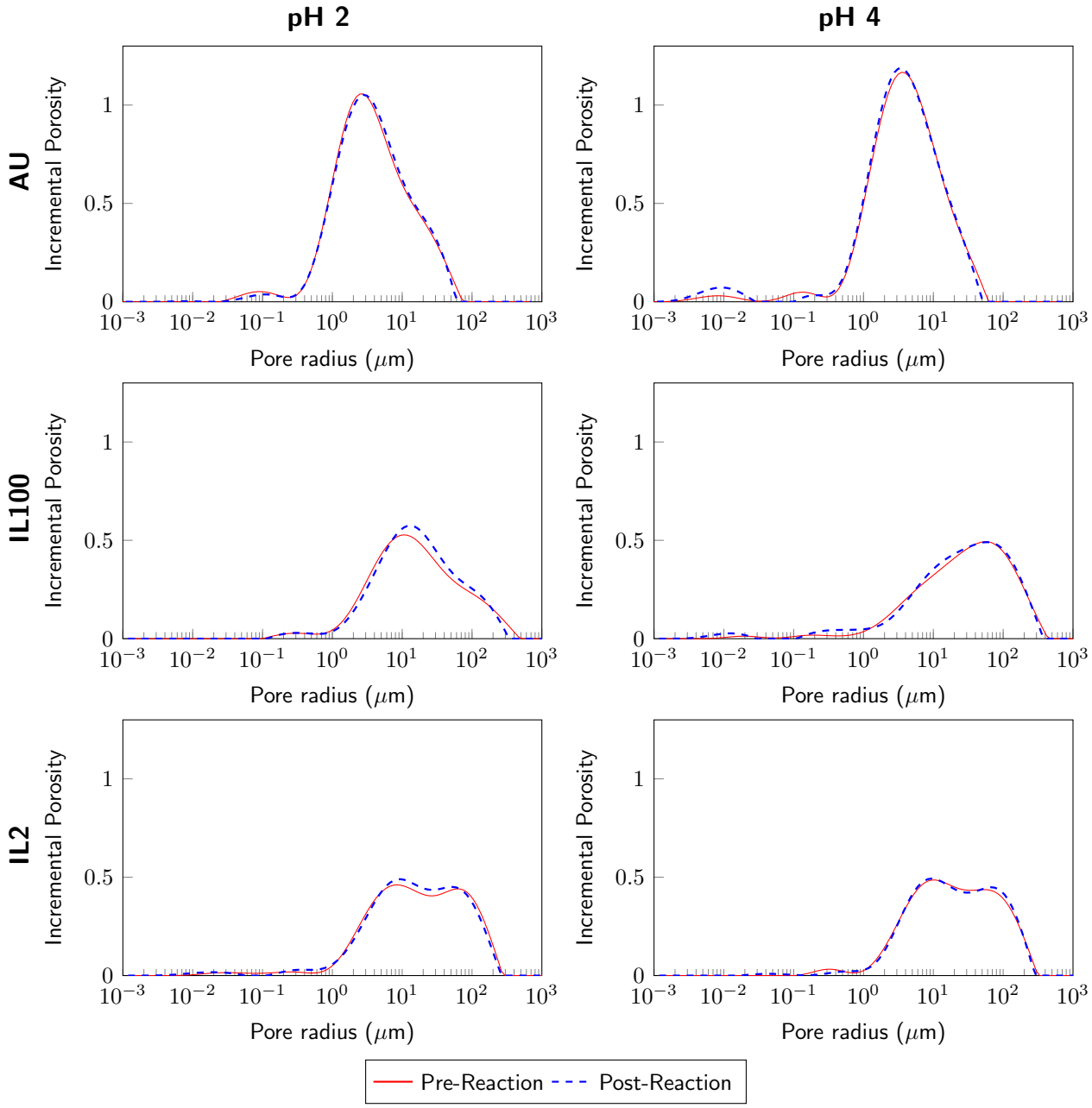


**Figure 6.** Pore size distribution for each carbonate sample based on the nuclear magnetic resonance (NMR). The correlation between the $T_2$ relaxation time and pore radius is based on Equation 2.

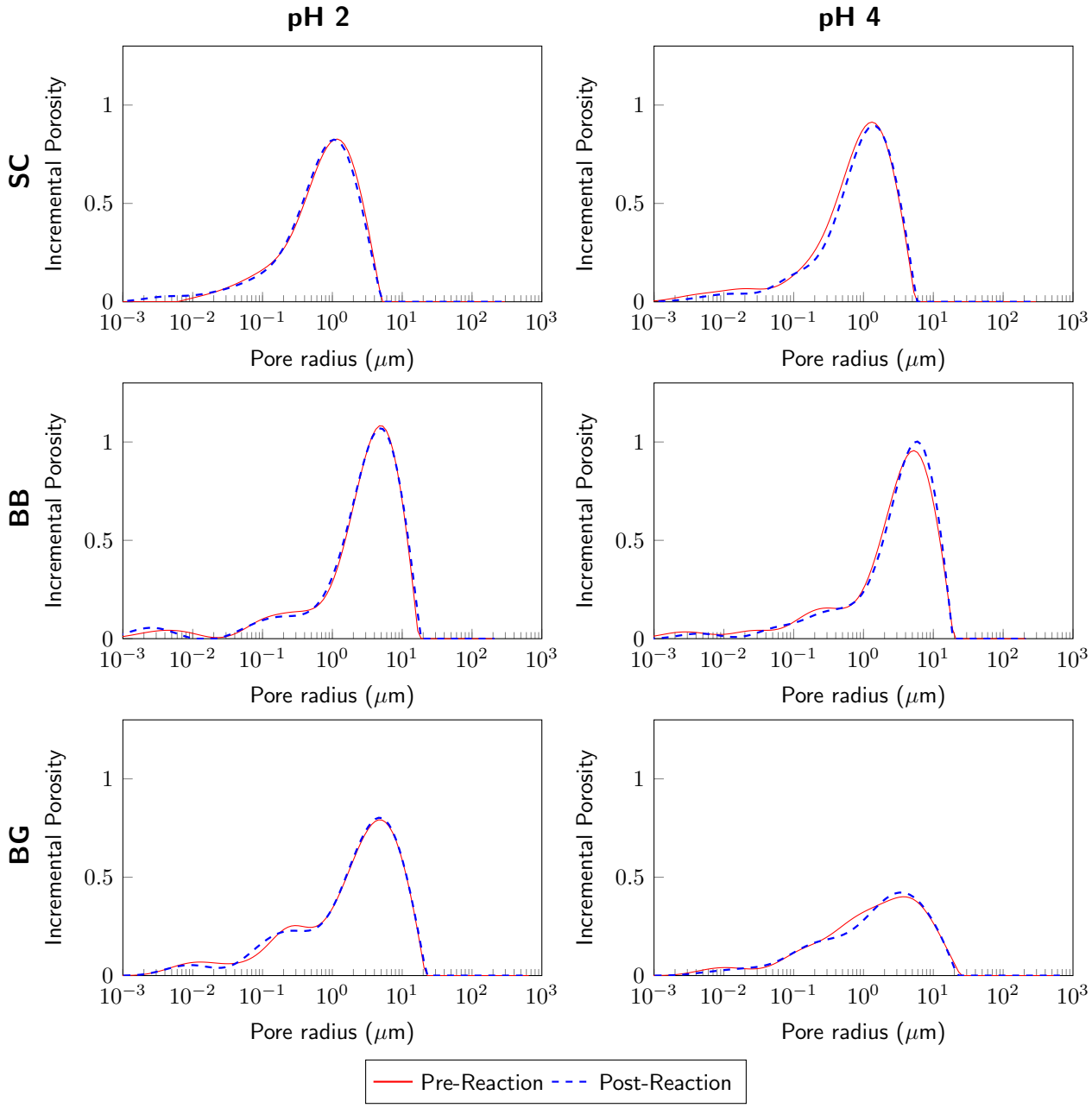


**Figure 7.** Pore size distribution for each sandstone sample based on the nuclear magnetic resonance (NMR). The correlation between the $T_2$ relaxation time and pore radius is based on Equation 2.

**Wettability** The wettability of the samples were measured using a Sessile drop method where a drop of the fluid is dropped from a tip on to the solid surface and the contact angle is measured. This contact angle is the apparent contact angle for a static fluid and can be different that the dynamic contact angle that the fluid observes while moving in the porous media. Care has been taken in handling the rock surface as well to make sure that it does not come in direct contact with the user's hand as the bodily oil on the fingers can significantly alter the contact angle.

The wettability of the rocks was observed to change due to the acid/rock interaction. In carbonates, at lower pH, a significant reduction in the contact angle was observed in each sample, rendering the wettability more water-wet (Figure 8a). The most considerable change was observed in AU, while the least change occurred in IL2. Conversely, at higher pH some variations emerged (Figure 8b). The reduction in contact angle was solely observed in AU, whereas in IL100 and IL2, the contact angle increased. This suggests that for IL100 and IL2, the samples were less water-wet after the acid interaction.

For sandstones, the observed behavior was converse to that in carbonates (Figure 8). The contact angle consistently increased due to the effect of acid interaction. This behavior was observed in both low and high pH acids, with pH 4 resulting in a less pronounced increase than pH 2. The most substantial increment was observed in SC, indicating that sandstones tend to become less water-wet after the acid interaction.

Even though the time scale of the interaction is considerably low, it has been previously shown that the acid could alter the wettability of the mineral surfaces, specifically calcite (Standnes and Austad, 2003). For instance, Rezaei Gomari and Hamouda (2006) showed that under 15 minutes of soaking time, the wettability still could be altered. The alteration in permeability could also be attributed to the change in wettability, wherein the water-wet condition influences the relative permeability of DI water (Owens and Archer, 1971). Given that DI water was employed in the permeability measurements, this change in wettability could potentially impact the liquid permeability.

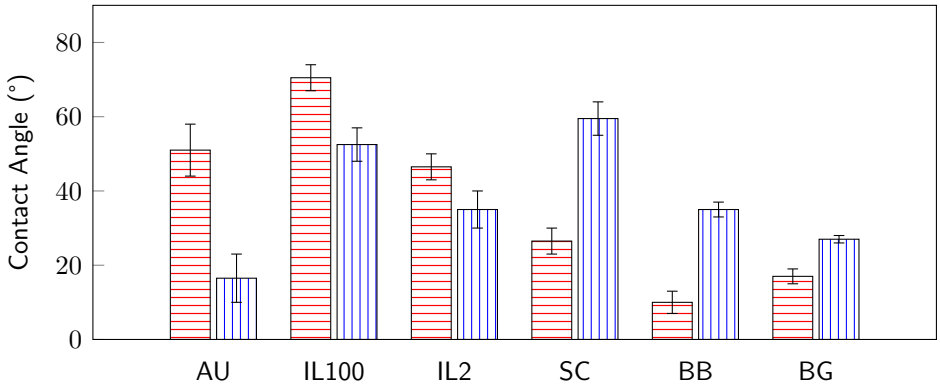


**(a)** pH 2

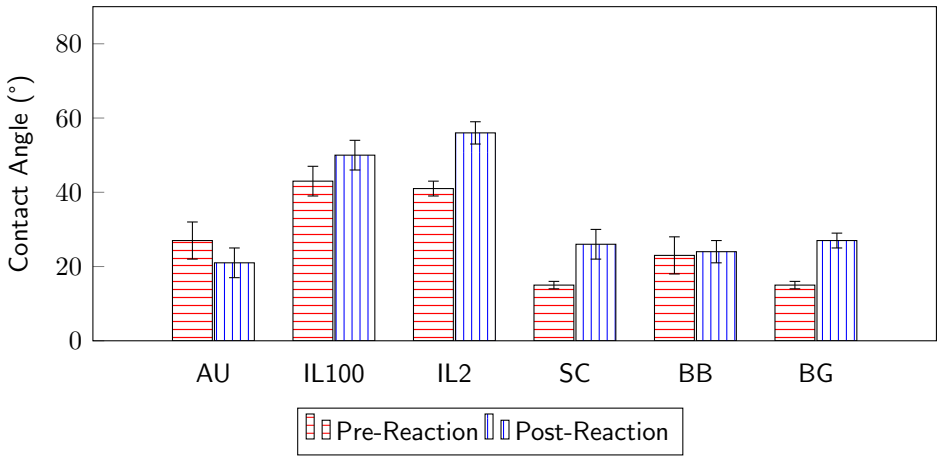


**(b)** pH 4

**Figure 8.** Comparison of the water-air contact angle for all pre- and post-acid reaction core samples for (a) pH 2 and (b) pH 4 sample.

## 3.3 Model Fitting Results

The experimental capillary rise data were fit to three different models: Tsunazawa (Tsunazawa et al., 2016), Lucas-Washburn (L-W) (Cai et al., 2021), and Quéré (Quéré, 1997) using the Levenberg-Marquardt algorithm (Moré, 1978). The fitting method and results for all the methods are shown in Appendix A. Tsunazawa's model was able to fit the water imbibition experimental data better (higher $R^2$ value) compared to the Lucas-Washburn and Quéré equation. Table 3 displays the best-fit for three parameters obtained from Tsunazawa's models: pore size, tortuosity, and contact angle.

Across the carbonate samples, a consistent reduction in pore size was observed in the water pre-reaction, acid spontaneous imbibition, and water post-reaction stages, except for the IL100 sample at pH 4. Notably, at lower pH, the simulation indicated the most significant change in the IL2 sample, while the IL100 sample displayed the least alteration in pore size. Minor changes in tortuosity were evident in all samples: IL100 and IL2 displayed a slight decrease, whereas AU exhibited an increasing trend. This trend persisted at higher pH levels, except for IL100, where the tortuosity decreased for water post-reaction but increased during acid imbibition. Notably, at lower pH levels, both AU and IL2 showcased higher pore size and tortuosity changes compared to other conditions.

In sandstones, notable variations were observed in the results of the fitting parameters. At lower pH levels, both pore size and tortuosity showed reductions in water post-reaction for SC and BB, while pore size and tortuosity increased during acid imbibition. Conversely, BG exhibited the inverse behavior: pore size decreased during acid imbibition and enlarged in water post-reaction. However, tortuosity consistently increased across all scenarios. At higher pH levels, a consistent reduction in pore size was observed in both acid and water post-reaction for all samples, with a more pronounced reduction observed in water post-reaction. Tortuosity consistently increased, showing a higher increase in water post-reaction. Notably, no clear correlation was evident between pH levels and the observed changes in each of the fitting parameters.

**Table 3.** The fitting parameters based on Tsunazawa's model (Tsunazawa et al., 2016). The fitting parameters in this calculation is the pore size and the tortuosity with an adjustment from the contact angle based on the laboratory measurements and error during the measurement.

| **Sample Name** | **pH** | **Water capillary rise (Pre-acid)** | | | **Acid capillary rise** | | | **Water capillary rise (Post-acid)** | | |
|---|---|---|---|---|---|---|---|---|---|---|
| | | $r$ (µm) | $\tau$ | $\theta$ (°) | $r$ (µm) | $\tau$ | $\theta$ (°) | $r$ (µm) | $\tau$ | $\theta$ (°) |
| **AU** | 2 | 326.63 | 2.89 | 62.76 | 328.91 | 2.90 | 50.00 | 259.42 | 3.16 | 16.74 |
| | 4 | 529.51 | 4.08 | 28.50 | 464.60 | 4.35 | 26.17 | 493.45 | 4.11 | 23.55 |
| **IL100** | 2 | 81.29 | 4.97 | 69.46 | 53.69 | 4.23 | 62.6 | 70.25 | 4.23 | 53.4 |
| | 4 | 157.95 | 3.37 | 44.73 | 288.07 | 3.47 | 51.77 | 330.23 | 3.25 | 45.90 |
| **IL2** | 2 | 184.77 | 4.59 | 70.75 | 80.39 | 3.60 | 59.63 | 79.81 | 3.85 | 51.43 |
| | 4 | 65.20 | 5.57 | 44.73 | 55.41 | 4.30 | 57.77 | 55.59 | 4.84 | 50.32 |
| **SC** | 2 | 60.82 | 5.16 | 27.93 | 61.26 | 5.88 | 40.69 | 55.55 | 4.26 | 61.53 |
| | 4 | 56.19 | 4.28 | 15.62 | 52.89 | 4.34 | 21.03 | 51.93 | 5.13 | 27.49 |
| **BB** | 2 | 363.06 | 3.36 | 9.98 | 493.58 | 4.18 | 20.26 | 320.85 | 3.02 | 32.62 |
| | 4 | 402.33 | 4.60 | 22.61 | 165.57 | 4.69 | 24.04 | 296.61 | 4.80 | 26.13 |
| **BG** | 2 | 55.96 | 4.23 | 17.84 | 45.78 | 4.56 | 23.19 | 57.59 | 5.24 | 28.64 |
| | 4 | 46.99 | 4.85 | 15.65 | 36.90 | 5.72 | 18.83 | 30.95 | 5.85 | 23.13 |

## 3.4 Mineral dissolution and precipitation

**Carbonates** Since all of the carbonate samples dominantly consist of calcite (Table 1), the reaction between the $H^+$ and $CaCO_3$ is the main reaction that drives the porosity alteration (Eq. 5). Dissolution occurs when the calcite solid surface dissolve due to the brine interaction at undersaturated conditions while precipitation deposits calcite solid in oversaturated conditions. Both of these processes result in the alteration of the petrophysical properties of the rock.

$$CaCO_{3(s)} + 2H^{+}{}_{(aq)} \longleftrightarrow Ca^{2+}{}_{(aq)} + H_2O_{(l)} + CO_{2(g)} \tag{5}$$

The dissolution process was tracked through the ICP-OES analysis of the ionic composition after the rocks' interaction with acidic fluid (Figure 9a). The presence of $Ca^{2+}$, particularly noticeable in lower pH conditions, strongly suggests an active dissolution process. This ion exhibited consistent and similar concentration levels across all carbonate samples. However, the varying final concentrations also imply differing reaction rates depending on the pH levels. Lower pH shows a higher reaction rate. These reaction rate condition also have been consistently observed in the previous studies (Alkattan et al., 1998, 2002; Rabie et al., 2011; Gray et al., 2018).

Additionally, the consistent detection of $Mg^{2+}$ across all samples raises the possibility of low amounts of Mg-enriched calcites being present, although none of which were observed in surface XRD (Table 1). Mg could also be present in the calcite minerals as impurities and could react with acid, resulting in the generation of $Ca^{2+}$ and $Mg^{2+}$ (Eq. 6). It is conceivable that any Mg content might be minimal or confined to regions that weren't analyzed via surface XRD. This aligns with the ionic composition data, where the concentration of $Mg^{2+}$ remained below 10 mg/L, suggesting a very low amount of Mg impurities.

Even with a low acid concentration, calcite dissolution could still be prominent (Alkattan et al., 1998). In the micro-scale, a smoother grain surface has a strong indication that calcite dissolution happened, which was previously observed by Järvinen et al. (2012). On the other hand, Singh et al. (2018) observed the increment of porosity distribution

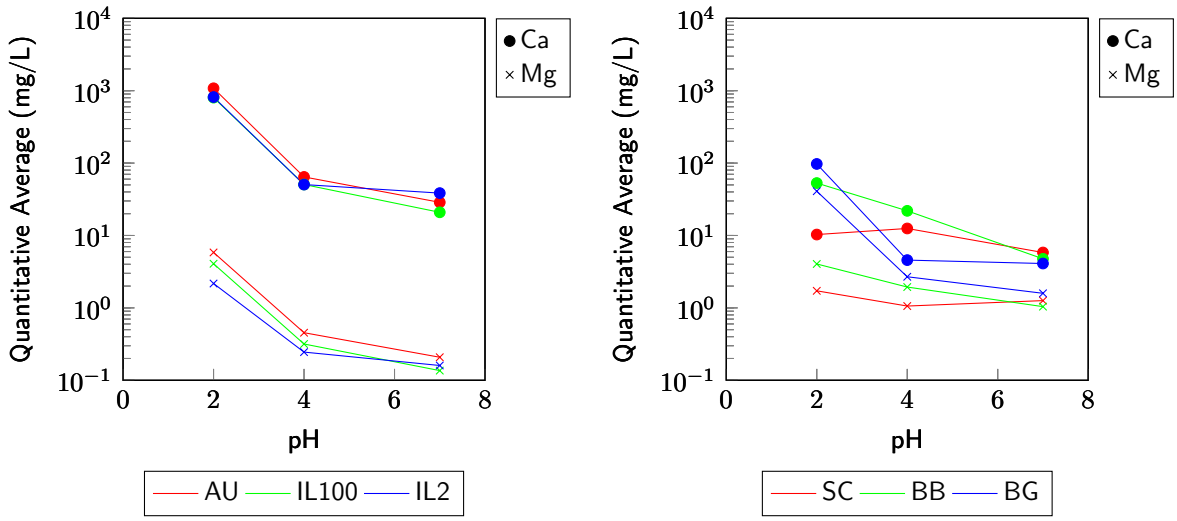


**(a)** Carbonates **(b)** Sandstones

**Figure 9.** Comparison of the $Ca^+$ and $Mg^+$ ion composition of the fluid after the fluid-rock interaction.

during the injection of reactive $CO_2$-saturated brine.

In addition to the dissolution process, the presence of calcite precipitation has been noted, particularly evident in pore size reduction within larger pores, as observed through NMR and Tsunazawa's fitting parameters. This phenomenon is primarily attributed to oversaturated calcium ions and carbon dioxide ($CO_2$) gas, byproducts generated during the dissolution process (Eq. 5). As these components were transported with the fluids to other locations, simultaneous reactions occurred, leading to calcite precipitation in different areas of the sample. This observation is consistent with the findings of Eloneva et al. (2008), who also highlighted how dissolution byproducts can trigger calcite precipitation.

**Sandstones** In sandstones, although not as predominant as in carbonate samples, a noticeable presence of $Ca^{2+}$ and $Mg^{2+}$ was detected in the fluid's ionic composition (Figure 9b). This observation is particularly understandable in BG due to its rock composition containing a significant proportion of dolomite (Eq. 6). Dolomite typically exhibits a slower reaction rate compared to calcites (Khalid et al., 2015; Lund et al., 1973), consequently resulting in lower concentrations of $Ca^{2+}$ and $Mg^{2+}$ compared to the carbonate samples.

$$CaMg(CO_3)_{2(s)} + 4H^+{}_{(aq)} \longleftrightarrow Ca^{2+}{}_{(aq)} + Mg^{2+}{}_{(aq)} + 2H_2O_{(l)} + 2CO_{2(g)} \tag{6}$$

For the case of BB and SC, where there are no significant carbonate minerals in the rock composition (Table 1), small amounts of Mg-enriched calcite have been found as cementing agent binding the grains (Washburn et al., 2017). This minor amount of Mg-enriched calcite may not have been detectable through surface XRD analysis but still underwent a reaction with acid, thereby influencing the petrophysical properties. However, further investigation is warranted including conducting a bulk XRD scan (performed on a powder) rather than a surface XRD.

## 3.5 Flow Regime Analysis

The dimensionless time and height were plotted to observe the flow regime changes during capillary rise experiment and are present in the Appendix B. The red line (steep gradient) and blue line (gentle gradient) in Figures B1 and B2 show the fit experimental data based on the Quéré and Lucas-Washburn equations respectively plotted in dimensionless height and time (Eq. 4). The intersection of these two lines indicates the transition of the flow regime from inertial to viscous flow, called the intercept time. As the effect of acid imbibition, the intercept time in post-reaction water capillary rise was significantly changed throughout the samples.

The acid imbibition process exhibited distinct behavior compared to water imbibition, reflected in the changes in intercept time (Table 4). In carbonates, variations were observed in both higher and lower pH. At lower pH, the viscous flow regime occurred earlier in IL100 and IL2, while in AU, it occurred later. Conversely, at higher pH, the viscous flow regime happened earlier for AU and IL2, while for IL100, it occurred later. There is no clear correlation between the pH and the intercept time. In IL2, the changes were minimal in higher pH, and larger in lower pH. For the other samples, distinct behavior was observed between higher and lower pH, making it inconclusive.

In sandstones, the results were more consistent, consistently showing a reduction in the intercept time for acid imbibition compared to the pre-reaction water imbibition. This

**Table 4.** The time interception of the dimensionless analysis to determine the flow regime. The interception time represents the transition time from the purely inertial to the purely viscous flow regime as explained in Pratama and Khan (2024).

| Sample Name | pH | Intercept Time ($t_{int}$ (s)) | | |
|---|---|---|---|---|
| | | Pre- | Acid | Post- |
| **AU** | 2 | 288 | 328 | 287 |
| | 4 | 360 | 357 | 304 |
| **IL100** | 2 | 33 | 26 | 29 |
| | 4 | 133 | 289 | 220 |
| **IL2** | 2 | 85 | 59 | 51 |
| | 4 | 33 | 27 | 33 |
| **SC** | 2 | 48 | 33 | 35 |
| | 4 | 60 | 20 | 51 |
| **BB** | 2 | 304 | 303 | 283 |
| | 4 | 309 | 183 | 111 |
| **BG** | 2 | 52 | 38 | 25 |
| | 4 | 23 | 18 | 14 |

indicates an earlier onset of the viscous flow regime. In SC and BB the changes in the intercept time were more substantial in higher pH. Conversely, in BG, a lower pH resulted in a larger difference in intercept time.

The acid also affects the flow regime of post-acid water capillary rise and decreases the time of the inertial flow regime. It is consistently observed that for the carbonate, at lower pH, the transition from viscous to inertial flow is decreased between the pre- and post-reaction experiment (Table 4). At higher pH levels, subtle variations in the intercept time were observed: reduction in AU, increment in IL100, and no change in IL2.

In sandstones, the observed reduction in intercept time was consistently noted. Yet, there's a subtle variation in the correlation between pH and intercept time. In SC and BG, larger changes in intercept time occurred in lower pH conditions, while in higher pH, these changes were smaller. Conversely, for BB, the trend was opposite, displaying larger changes in intercept time in higher pH and smaller changes in lower pH.

The results suggest that in sandstones, the impact of the acid is more consistent, resulting in an earlier onset of the viscous flow regime. However, for carbonates, the situation is more intricate, and the results are inconclusive. This could indicate that the methodology proposed by Fries and Dreyer (2008b) is more suitable for less complex systems like sandstones, where the reaction is minimal, as opposed to more complex systems characterized by continuous alterations in petrophysical properties, such as carbonates. Thus, it is important to introduce a new methodology to incorporate this problem.

The nature of flow regimes plays a crucial role in highlighting the limitations of the Tsunazawa et al. (2016) model. This model, akin to the L-W model, overlooks inertial and viscous forces in capillary rise dynamics. The interplay between fluid inertia, capillary force, fluid weight, and resisting viscous forces governs capillary rise dynamics (Shardt et al., 2014). These forces can induce oscillations in the capillary front during the rise process (Quéré et al., 1999). Previous research has also recognized the emergence of two distinct fronts, namely the fluid and particle fronts, as an outcome of these forces influencing dynamic capillary rise behavior (Das et al., 2012; Das and Mitra, 2013; Bhaduri et al., 2014).

## 3.6 Comprehensive discussion

The reactive capillary rise exhibits a distinct profile in comparison with the capillary rise profile observed with neutral fluid. This disparity arises from the interaction between the fluids and the rock's mineral surfaces. Referred to as the coupled hydro-chemical process, this phenomenon during reactive capillary rise is depicted in Figure 10. Initially, the petrophysical properties of porous materials, in conjunction with the fluid characteristics, determine the capillary rise profile, encompassing factors like the maximum capillary height and the capillary rate.

However, during the reactive capillary rise process, chemical reactions occur within the porous media, leading to alterations in both the petrophysical properties and the fluid characteristics. The impact of acidic capillary rise on pore sizes, wettability, and tortuosity has been discussed in the previous sections and these alterations induce changes in the capillary rise profile. Coupled with the reactivity, a cyclic process is initiated that con-

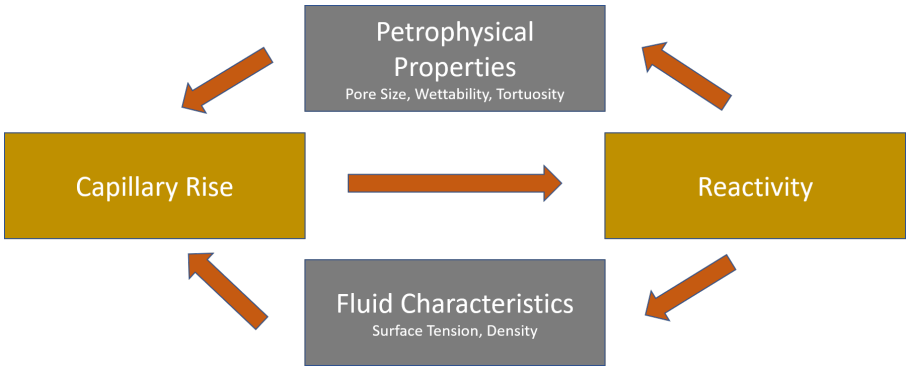


**Figure 10.** The cycle of coupled hydro-chemical processes during reactive capillary rise.

tinues indefinitely unless one of the processes (reaction or capillary-induced movement) halts: either when the capillary height reaches its maximum theoretical limit or when the fluids ceases to react. All of these alterations in petrophysical properties undoubtedly impact the capillary height and align closely with the experimental observations and measurements. This relationship between wettability, pore sizes, and capillary height is evident in Equations 1 and 3a.

A rough estimate for the Damköhler number can be determined for the calcite dissolution reaction in the sandstone and calcite samples. Since the capillary height varies between 10 and 30 mm for all the rock samples in 800 seconds of imbibition (Figures 2 and 3), the hydraulic residence time can be calculated between 2000 s and 6000 s. Considering a first order reaction with a reaction rate of $10^{-6}$ mol/m$^2$/s, the Damköhler number can be estimated to be between $2 - 6\times10^{-3}$. This indicates that all of the fluid is not reacted instantly and the reactive fluid packet imbibes deeper inside the rock where it can further react. Therefore the reaction profile is expected to show spatial dependence, with the maximum change expected near the fluid-rock interface. This was observed using micro-CT scanning in Pratama and Khan (2024).

Distinct behaviors were observed between sandstones and carbonates, particularly under varying pH conditions. In carbonates with a pH of 2, generally a slower capillary rate was observed at early times before gradually accelerating (Figure 2). In comparison, the neutral pH 7 fluid generally showed a quicker capillary rise initially which then gradually slows down. The initial deceleration in pH 2 suggests an enlargement in pore size during the early stages, followed by a reduction in pore size in the latter stages. This observation is also evident from the NMR which shows simultaneous dissolution and precipitation in

different pore sizes (Figure 6). This indicates a trend where mineral dissolution predominantly occurs in the lower part of the rock while mineral precipitation takes place in the upper part. Additionally, wettability significantly influences capillary height. The reduction in contact angle corresponds to an increased capillary height.

At higher pH levels (pH 4), the increase in capillary height is relatively slower due to less pronounced changes in the petrophysical properties compared to the more acidic pH 2 conditions. Moreover, the pore size distribution notably shifts towards the left (Figure 6), suggesting a more pronounced precipitation compared to lower pH levels. Despite this, the overall bulk porosity values after the acidic imbibition remain higher (Table 2) indicating that dissolution is still more prominent than precipitation. Additionally, the contact angle exhibits inconsistent behavior, albeit with changes that remain lower than those observed at lower pH levels.

Conversely in sandstones, the capillary height for both acidic fluids (pH 2 and pH 4) was observed to be lower compared to pH 7 (Figure 4). At the lower pH, the pore size distribution shifted towards the left (Figure 7) indicating pore reduction. However, an increase in the overall bulk porosity was noted (Table 2). It is noteworthy to emphasize that the predominant reaction observed was caclite cement dissolution. This process can potentially lead to the loosening of grains, thereby promoting fines migration. Such a phenomenon could also significantly alter the structure of the pore network, however no current observation has been made of this phenomenon. Coupled with the increase in contact angle, these changes likely contributed to the reduction in capillary height.

At the higher pH level (pH 4), a more pronounced reduction in capillary height was observed in BB and BG, while SC showed a lower reduction (Figure 3). Interestingly, the pore size distribution exhibited distinct characteristics compared to lower pH levels; it shifted towards the right (Figure 7), indicating pore enlargement. Correspondingly, there was an increase in bulk porosity, supporting the observed pore enlargement (Table 2). While evidence of grain dissolution within the sandstones was scarce, the dissolution of calcite cements, similar to the lower pH, was evident. However, this dissolution wasn't as pronounced as in lower pH conditions (Figure 9b) and potentially will not be substantial enough to loosen the grains for fines migration. When considering this observation alongside the increase in contact angle, it aligns with and supports the reduction in capillary

height.

# 4 Conclusion

The investigation into reactive fluid transport within porous media underscores the pivotal role of capillary interactions in shaping fluid behavior. The interplay between reactive fluids and the mineral composition within the pore system is paramount, provoking alterations in petrophysical properties and influencing capillary rise behavior.

In examining the distinct capillary rise profiles exhibited by acidic fluids in carbonates and sandstones, it became evident that the final capillary height and the nature of alterations in capillary behavior vary significantly based on the rock type and pH levels. In carbonates, the final capillary height is higher, while in sandstones, it is lower. Notably, in carbonates, these changes are more pronounced at lower pH levels, whereas in sandstones, higher pH levels demonstrate more significant alterations.

The reactions between acidic fluids and minerals induce shifts in petrophysical properties, especially porosity, pore size distribution, and permeability. Notably, in carbonates, dissolution, and precipitation of calcite with some magnesium impurities processes dynamically alter porosity and pore size distribution, with dissolution being more prominent at lower pH conditions. Sandstones, on the other hand, displayed dissolution primarily in Mg-enriched calcite, influencing pore size distribution and permeability, with notable variations in wettability across different pH conditions.

Furthermore, the impact of acid imbibition on the transition from inertial to viscous flow varied across rock types. Carbonates exhibited inconsistencies in correlating pH levels with intercept time, indicating complexity in the relationship between fluid reactivity and flow behavior. Conversely, sandstones displayed a more uniform response, showcasing an earlier onset of the viscous flow regime across different pH conditions.

This study highlights the often-overlooked connection between capillary interactions and fluid reactivity, emphasizing the significance of understanding the interplay between fluids and porous materials in reactive fluid transport within porous media. While conducted at

a core-scale and within short time frames, this research serves as a critical demonstration of the substantial influence of reactivity on reactive imbibition.

In conclusion, this research signifies a crucial step forward in unraveling the complexities of reactive fluid transport in porous media, advocating for further explorations at larger scales and extended durations to comprehensively understand the implications and applications of these findings across diverse fields of study and industrial practices.

# Data availability

All the data generated during this study was obtained at the Center of Integrative Petroleum Research at King Fahd University of Petroleum and Minerals (Saudi Arabia) and can be accessed at Pratama and Khan (2024). The imaging data was processed using MATLAB (Matlab, 2022) and Fiji (Schindelin et al., 2012). The figures in the manuscript are generated using PGFplots (Feuersänger, 2018).

# References


M. R. Hall and D. Allinson. 1 - Heat and mass transport processes in building materials. In Matthew R. Hall, editor, *Materials for Energy Efficiency and Thermal Comfort in Buildings*, Woodhead Publishing Series in Energy, pages 3–53. Woodhead Publishing, January 2010. ISBN 978-1-84569-526-2. doi: 10.1533/9781845699277.1.3. URL https://www.sciencedirect.com/science/article/pii/B9781845695262500013.

N. Lu and W. J. Likos. Rate of Capillary Rise in Soil. *Journal of Geotechnical and Geoenvironmental Engineering*, 130(6):646–650, June 2004. ISSN 1090-0241. doi: 10.1061/(ASCE)1090-0241(2004)130:6(646). URL https://ascelibrary.org/doi/10.1061/%28ASCE%291090-0241%282004%29130%3A6%28646%29. Publisher: American Society of Civil Engineers.

H. Dehghanpour, Q. Lan, Y. Saeed, H. Fei, and Z. Qi. Spontaneous Imbibition of Brine and Oil in Gas Shales: Effect of Water Adsorption and Resulting Microfractures. *Energy & Fuels*, 27(6):3039–3049, June 2013. ISSN 0887-0624. doi: 10.1021/ef4002814. URL https://doi.org/10.1021/ef4002814. Publisher: American Chemical Society.

Abdul Salam Abd, Elsiddig Elhafyan, Abdul Rafey Siddiqui, Wajdi Alnoush, Martin J. Blunt, and Nayef Alyafei. A review of the phenomenon of counter-current spontaneous imbibition: Analysis and data interpretation. *Journal of Petroleum Science and Engineering*, 180: 456–470, September 2019. ISSN 0920-4105. doi: 10.1016/j.petrol.2019.05.066. URL https://www.sciencedirect.com/science/article/pii/S0920410519305200.

Yan Zhou, Wei Guan, Changming Zhao, Xiaojing Zou, Zhennan He, and Hongyang Zhao. Spontaneous imbibition behavior in porous media with various hydraulic fracture propagations: A pore-scale perspective. *Advances in Geo-Energy Research*, 9(3):185–197, 2023. doi: 10.46690/ager.2023.09.06. URL https://www.sciopen.com/article/10.46690/ager.2023.09.06.

Kristopher L. Kuhlman, Melissa M. Mills, Jason E. Heath, Matthew J. Paul, Jennifer E. Wilson, and John Eric Bower. Parameter estimation from spontaneous imbibition into volcanic tuff. *Vadose Zone Journal*, 21(2):e20188, 2022. ISSN 1539-1663. doi: 10.1002/vzj2.20188. URL https://onlinelibrary.wiley.com/doi/abs/10.1002/vzj2.20188. _eprint: https://onlinelibrary.wiley.com/doi/pdf/10.1002/vzj2.20188.

Christopher Zahasky and Sally M. Benson. Preferential Solute Transport in Low Permeability Zones During Spontaneous Imbibition in Heterogeneous Porous Media. *Water Resources Research*, 58(1):e2020WR029460, 2022. ISSN 1944-7973. doi: 10.1029/2020WR029460. URL https://onlinelibrary.wiley.com/doi/abs/10.1029/2020WR029460. _eprint: https://onlinelibrary.wiley.com/doi/pdf/10.1029/2020WR029460.

Christopher Zahasky and Sally M. Benson. Spatial and Temporal Quantification of Spontaneous Imbibition. *Geophysical Research Letters*, 46 (21):11972–11982, 2019. ISSN 1944-8007. doi: 10.1029/2019GL084532. URL https://onlinelibrary.wiley.com/doi/abs/10.1029/2019GL084532. _eprint: https://onlinelibrary.wiley.com/doi/pdf/10.1029/2019GL084532.

Amir H. Haghi, Richard Chalaturnyk, Martin J. Blunt, Kevin Hodder, and Sebastian Geiger. Poromechanical controls on spontaneous imbibition in earth materials. *Scientific Reports*, 11(1):3328, February 2021. ISSN 2045-2322. doi: 10.1038/s41598-021-82236-x. URL https://www.nature.com/articles/s41598-021-82236-x. Publisher: Nature Publishing Group.

Hamed Aslannejad, Alexandros Terzis, S. Majid Hassanizadeh, and Bernhard Weigand. Occurrence of temperature spikes at a wetting front during spontaneous imbibition. *Scientific Reports*, 7(1):7268, August 2017. ISSN 2045-2322. doi: 10.1038/s41598-017-07528-7. URL https://www.nature.com/articles/s41598-017-07528-7. Publisher: Nature Publishing Group.

X. Yin, H. Aslannejad, E. T. de Vries, A. Raoof, and S. M. Hassanizadeh. Droplet Imbibition into Paper Coating Layer: Pore-Network Modeling Simulation. *Transport in Porous Media*, 125(2):239–258, November 2018. ISSN 1573-1634. doi: 10.1007/s11242-018-1116-0. URL https://doi.org/10.1007/s11242-018-1116-0.

Geoffrey Mason and Norman R Morrow. Developments in spontaneous imbibition and possibilities for future work. *Journal of Petroleum Science and Engineering*, 110:268–293, 2013.

Sebnem Boduroglu and Rashid Bashir. Review of Capillary Rise Experiments for Surface-Active Solutes in the Subsurface. 2022.

Richard Lucas. Ueber das Zeitgesetz des kapillaren Aufstiegs von Flüssigkeiten. *Kolloid-Zeitschrift*, 23(1):15–22, 1918.

Edward W Washburn. The dynamics of capillary flow. *Physical review*, 17(3):273, 1921.

David Benavente, Peter Lock, M Ángeles García Del Cura, and Salvador Ordóñez. Predicting the capillary imbibition of porous rocks from microstructure. *Transport in porous media*, 49(1):59–76, 2002.

N Fries and M Dreyer. An analytic solution of capillary rise restrained by gravity. *Journal of colloid and interface science*, 320(1):259–263, 2008a.

Yuya Tsunazawa, Tadashi Yokoyama, and Naoki Nishiyama. An experimental study on the rate and mechanism of capillary rise in sandstone. *Progress in Earth and Planetary Science*, 3(1):1–10, 2016.

Yury Villagrán Zaccardi, Natalia Mariel Alderete, and Nele De Belie. Lucas-Washburn vs Richards equation for the modelling of water absorption in cementitious materials. In *5th International Conference on Concrete Repair, Rehabilitation and Retrofitting (ICCRRR)*, volume 199. EDP Sciences, 2018.

Junjie Wang, Amgad Salama, and Jisheng Kou. Experimental and numerical analysis of imbibition processes in a corrugated capillary tube. *Capillarity*, 5(5):83–90, 2022. doi: 10.46690/capi.2022.05.01. URL https://www.sciopen.com/article/10.46690/capi.2022.05.01.

Wenjia Fan, Kim F. Hayes, and Brian R. Ellis. Estimating Radium Activity in Shale Gas Produced Brine. *Environmental Science & Technology*, 52(18):10839–10847, September 2018. ISSN 0013-936X, 1520-5851. doi: 10.1021/acs.est.8b01587. URL https://pubs.acs.org/doi/10.1021/acs.est.8b01587.

Pascale. Vachon, Rajeshwar D. Tyagi, Jean Christian. Auclair, and Kevin J. Wilkinson. Chemical and biological leaching of aluminum from red mud. *Environmental Science & Technology*, 28(1):26–30, January 1994. ISSN 0013-936X, 1520-5851. doi: 10.1021/es00050a005. URL https://pubs.acs.org/doi/abs/10.1021/es00050a005.

Balasubrahmanyam Avvaru, S. B. Roy, Yogesh Ladola, Sujit Chowdhury, K. N. Hareendran, and Aniruddha B. Pandit. Sono-chemical leaching of uranium. *Chemical Engineering and Processing: Process Intensification*, 47(12):2107–2113, November 2008. ISSN 0255-2701. doi: 10.1016/j.cep.2007.10.021. URL https://www.sciencedirect.com/science/article/pii/S0255270107003583.

Suresh K. Bhargava, Rahul Ram, Mark Pownceby, Stephen Grocott, Bob Ring, James Tardio, and Lathe Jones. A review of acid leaching of uraninite. *Hydrometallurgy*, 151:10–24, January 2015. ISSN 0304-386X. doi: 10.1016/j.hydromet.2014.10.015. URL https://www.sciencedirect.com/science/article/pii/S0304386X14002308.

E. M. Córdoba, J. A. Muñoz, M. L. Blázquez, F. González, and A. Ballester. Passivation of chalcopyrite during its chemical leaching with ferric ion at 68°C. *Minerals Engineering*, 22(3):229–235, February 2009. ISSN 0892-6875. doi: 10.1016/j.mineng.2008.07.004. URL

https://www.sciencedirect.com/science/article/pii/S0892687508001830.

Qingyun Li, Adam D Jew, Gordon E Brown Jr, John R Bargar, and Katharine Maher. Reactive transport modeling of shale–fluid interactions after imbibition of fracturing fluids. *Energy & Fuels*, 34(5):5511–5523, 2020.

Ginevra Di Donato and Martin J. Blunt. Streamline-based dual-porosity simulation of reactive transport and flow in fractured reservoirs. *Water Resources Research*, 40(4), 2004. ISSN 1944-7973. doi: 10.1029/2003WR002772. URL https://onlinelibrary.wiley.com/doi/abs/10.1029/2003WR002772. _eprint: https://onlinelibrary.wiley.com/doi/pdf/10.1029/2003WR002772.

Muhammad Andiva Pratama and Hasan Javed Khan. Effect of ph on spontaneous imbibition in calcareous rock. *Water Resource Research (Accepted)*, 2024. doi: 10.1029/2023WR035307.

F. Jaeger, S. Bowe, H. Van As, and G. E. Schaumann. Evaluation of 1H NMR relaxometry for the assessment of pore-size distribution in soil samples. *European Journal of Soil Science*, 60(6):1052–1064, 2009. ISSN 1365-2389. doi: 10.1111/j.1365-2389.2009.01192.x. URL https://onlinelibrary.wiley.com/doi/abs/10.1111/j.1365-2389.2009.01192.x. _eprint: https://onlinelibrary.wiley.com/doi/pdf/10.1111/j.1365-2389.2009.01192.x.

Starting Matlab. Matlab. *The MathWorks, Natick, MA*, 2022.

W.-B. Bartels, M. Rücker, M. Boone, T. Bultreys, H. Mahani, S. Berg, S. M. Hassanizadeh, and V. Cnudde. Imaging Spontaneous Imbibition in Full Darcy-Scale Samples at Pore-Scale Resolution by Fast X-ray Tomography. *Water Resources Research*, 55(8):7072–7085, 2019. ISSN 1944-7973. doi: 10.1029/2018WR024541. URL https://onlinelibrary.wiley.com/doi/abs/10.1029/2018WR024541. _eprint: https://onlinelibrary.wiley.com/doi/pdf/10.1029/2018WR024541.

Hasan J. Khan, Ayaz Mehmani, Maša Prodanović, David DiCarlo, and Dayeed J. Khan. Capillary rise in vuggy media. *Advances in Water Resources*, 143:103671, September 2020. ISSN 0309-1708. doi: 10.1016/j.advwatres.2020.103671. URL https://www.sciencedirect.com/science/article/pii/S0309170820303699.

D Quéré. Inertial capillarity. *Europhysics Letters (EPL)*, 39(5):533–538, September 1997. ISSN 0295-5075, 1286-4854. doi: 10.1209/epl/i1997-00389-2. URL https://iopscience.iop.org/article/10.1209/epl/i1997-00389-2.

Naoki Ichikawa and Yoko Satoda. Interface Dynamics of Capillary Flow in a Tube under Negligible Gravity Condition. *Journal of Colloid and Interface Science*, 162(2):350–355, February 1994. ISSN 00219797. doi: 10.1006/jcis.1994.1049. URL https://linkinghub.elsevier.com/retrieve/pii/S0021979784710496.

Lateef Owolabi Lawal, Abdulrauf R. Adebayo, Mohamed Mahmoud, Ben Mansour Dia, and Abdullah S. Sultan. A novel NMR surface relaxivity measurements on rock cuttings for conventional and unconventional reservoirs. *International Journal of Coal Geology*, 231:103605, November 2020. ISSN 0166-5162. doi: 10.1016/j.coal.2020.103605. URL https://www.sciencedirect.com/science/article/pii/S0166516220306017.

Francisco Benavides, Ricardo Leiderman, Andre Souza, Giovanna Carneiro, and Rodrigo Bagueira de Vasconcellos Azeredo. Pore size distribution from NMR and image based methods: A comparative study. *Journal of Petroleum Science and Engineering*, 184:106321, January 2020. ISSN 0920-4105. doi: 10.1016/j.petrol.2019.106321. URL https://www.sciencedirect.com/science/article/pii/S0920410519307429.

Jonathan Mitchell and Edmund J. Fordham. Contributed Review: Nuclear magnetic resonance core analysis at 0.3 T. *Review of Scientific Instruments*, 85(11):111502, November 2014. ISSN 0034-6748. doi: 10.1063/1.4902093. URL https://doi.org/10.1063/1.4902093.

Everton Lucas-Oliveira, Arthur G. Araujo-Ferreira, Willian A. Trevizan, Bernardo Coutinho C. dos Santos, and Tito J. Bonagamba. Sandstone surface relaxivity determined by NMR T2 distribution and digital rock simulation for permeability evaluation. *Journal of Petroleum Science and Engineering*, 193:107400, October 2020. ISSN 0920-4105. doi: 10.1016/j.petrol.2020.107400. URL https://www.sciencedirect.com/science/article/pii/S0920410520304721.

Dag C Standnes and Tor Austad. Wettability alteration in carbonates. *Colloids and Surfaces A: Physicochemical and Engineering Aspects*, 216(1-3):243–259, April 2003. ISSN 09277757. doi: 10.1016/S0927-7757(02)00580-0. URL https://linkinghub.elsevier.com/retrieve/pii/S0927775702005800.

K. A. Rezaei Gomari and A. A. Hamouda. Effect of fatty acids, water composition and pH on the wettability alteration of calcite surface. *Journal of Petroleum Science and Engineering*, 50(2):140–150, February 2006. ISSN 0920-4105. doi: 10.1016/j.petrol.2005.10.007. URL https://www.sciencedirect.com/science/article/pii/S0920410505001671.

W W Owens and D L Archer. The Effect of Rock Wettability on Oil- Water Relative Permeability Relationships. *JOURNAL OF PETROLEUM TECHNOLOGY*, 1971.

Jianchao Cai, Tingxu Jin, Jisheng Kou, Shuangmei Zou, Junfeng Xiao, and Qingbang Meng. Lucas–Washburn equation-based modeling of capillary-driven flow in porous systems. *Langmuir*, 37(5):1623–1636, 2021.

Jorge J. Moré. The Levenberg-Marquardt algorithm: Implementation and theory. In G. A. Watson, editor, *Numerical Analysis*, pages 105–116, Berlin, Heidelberg, 1978. Springer Berlin Heidelberg. ISBN 978-3-540-35972-2.

Marwan Alkattan, Eric H Oelkers, Jean-Louis Dandurand, and Jacques Schott. An experimental study of calcite and limestone dissolution rates as a function of pH from −1 to 3 and temperature from 25 to 80°C. *Chemical Geology*, 151(1-4):199–214, October 1998. ISSN 00092541. doi: 10.1016/S0009-2541(98)00080-1. URL https://linkinghub.elsevier.com/retrieve/pii/S0009254198000801.

Marwan Alkattan, Eric H Oelkers, Jean-Louis Dandurand, and Jacques Schott. An experimental study of calcite dissolution rates at acidic conditions and 25 °C in the presence of NaPO3 and MgCl2. *Chemical Geology*, 190(1):291–302, October 2002. ISSN 0009-2541. doi: 10.1016/S0009-2541(02)00121-3. URL https://www.sciencedirect.com/science/article/pii/S0009254102001213.

Ahmed I. Rabie, Ahmed M. Gomaa, and Hisham A. Nasr-El-Din. Reaction of In-Situ-Gelled Acids With Calcite: Reaction-Rate Study. *SPE Journal*, 16(04):981–992, July 2011. ISSN 1086-055X. doi: 10.2118/133501-PA. URL https://doi.org/10.2118/133501-PA.

F. Gray, B. Anabaraonye, S. Shah, E. Boek, and J. Crawshaw. Chemical mechanisms of dissolution of calcite by HCl in porous media: Simulations and experiment. *Advances in Water Resources*, 121:369–387, November 2018. ISSN 0309-1708. doi: 10.1016/j.advwatres.2018.09.007. URL https://www.sciencedirect.com/science/article/pii/S0309170818303713.

Lauri Järvinen, Jarkko Albert Leiro, Frej Bjondahl, Claudio Carletti, and Olav Eklund. XPS and SEM study of calcite bearing rock powders in the case of reactivity measurement with HCl solution: XPS and SEM study of calcite bearing rock powders in the case of HCl. *Surface and Interface Analysis*, 44(5):519–528, May 2012. ISSN 01422421. doi: 10.1002/sia.3838. URL https://onlinelibrary.wiley.com/doi/10.1002/sia.3838.

Kamaljit Singh, Benaiah U. Anabaraonye, Martin J. Blunt, and John Crawshaw. Partial dissolution of carbonate rock grains during reactive CO2-saturated brine injection under reservoir conditions. *Advances in Water Resources*, 122:27–36, December 2018. ISSN 03091708. doi:

10.1016/j.advwatres.2018.09.005. URL https://linkinghub.elsevier.com/retrieve/pii/S0309170818305311.

Sanni Eloneva, Sebastian Teir, Justin Salminen, Carl-Johan Fogelholm, and Ron Zevenhoven. Steel Converter Slag as a Raw Material for Precipitation of Pure Calcium Carbonate. *Industrial & Engineering Chemistry Research*, 47(18):7104–7111, September 2008. ISSN 0888-5885, 1520-5045. doi: 10.1021/ie8004034. URL https://pubs.acs.org/doi/10.1021/ie8004034.

Muhammad Ali Khalid, Abdullah Sultan, and Xiangdong Qiu. Revisiting Reaction Kinetics and Diffusion Rate of Dolomitic Rock with HCl. OnePetro, September 2015. doi: 10.2118/175832-MS. URL https://dx.doi.org/10.2118/175832-MS.

Kasper Lund, H. Scott Fogler, and C. C. McCune. Acidization—I. The dissolution of dolomite in hydrochloric acid. *Chemical Engineering Science*, 28(3):691–IN1, March 1973. ISSN 0009-2509. doi: 10.1016/0009-2509(77)80003-1. URL https://www.sciencedirect.com/science/article/pii/0009250977800031.

Kathryn E. Washburn, Magdalena Sandor, and Yuesheng Cheng. Evaluation of sandstone surface relaxivity using laser-induced breakdown spectroscopy. *Journal of Magnetic Resonance*, 275:80–89, February 2017. ISSN 1090-7807. doi: 10.1016/j.jmr.2016.12.004. URL https://www.sciencedirect.com/science/article/pii/S1090780716302580.

N. Fries and M. Dreyer. The transition from inertial to viscous flow in capillary rise. *Journal of Colloid and Interface Science*, 327(1):125–128, November 2008b. ISSN 00219797. doi: 10.1016/j.jcis.2008.08.018. URL https://linkinghub.elsevier.com/retrieve/pii/S0021979708009661.

Orest Shardt, Prashant R Waghmare, JJ Derksen, and Sushanta K Mitra. Inertial rise in short capillary tubes. *Rsc Advances*, 4(28): 14781–14785, 2014.

David Quéré, Elie Raphael, and Jean-Yves Ollitrault. Rebounds in a capillary tube. *Langmuir*, 15(10):3679–3682, 1999.

Siddhartha Das, Prashant R Waghmare, and Sushanta K Mitra. Early regimes of capillary filling. *Physical Review E*, 86(6):067301, 2012.

Siddhartha Das and Sushanta K Mitra. Different regimes in vertical capillary filling. *Physical Review E*, 87(6):063005, 2013.

Swayamdipta Bhaduri, Pankaj Sahu, Siddhartha Das, Aloke Kumar, and Sushanta K Mitra. Capillary Imbibition Dynamics in Porous Media. In *International Conference on Nanochannels, Microchannels, and Minichannels*, volume 46278, page V001T08A002. American Society of Mechanical Engineers, 2014.

Johannes Schindelin, Ignacio Arganda-Carreras, Erwin Frise, Verena Kaynig, Mark Longair, Tobias Pietzsch, Stephan Preibisch, Curtis Rueden, Stephan Saalfeld, Benjamin Schmid, et al. Fiji: an open-source platform for biological-image analysis. *Nature methods*, 9(7): 676–682, 2012.

Christian Feuersänger. Pgfplots-a la-tex package to create normal/logarithmic plots in two and three dimensions. *Zugriff unter http://pgfplots. sourceforge. net*, 2018.

# Appendix A - Fitting Accuracy

The experimental data for sandstones and carbonates under pH 2 and 4 conditions were individually fit using three distinct, established equations: the Tsunazawa et al. (2016) model, the Lucas-Washburn equation (Washburn, 1921), and the Quéré equation (Quéré, 1997). One of the fitting process is depicted in Figure A1. The fitting accuracy, as assessed by the $R^2$ Score, is presented in Table A1. The results indicate that Tsunazawa's models generally exhibit superior accuracy across most cases. However, there are instances where the correlation does not follow a logarithmic trend, and the linear correlation (Quéré model) demonstrates better accuracy.

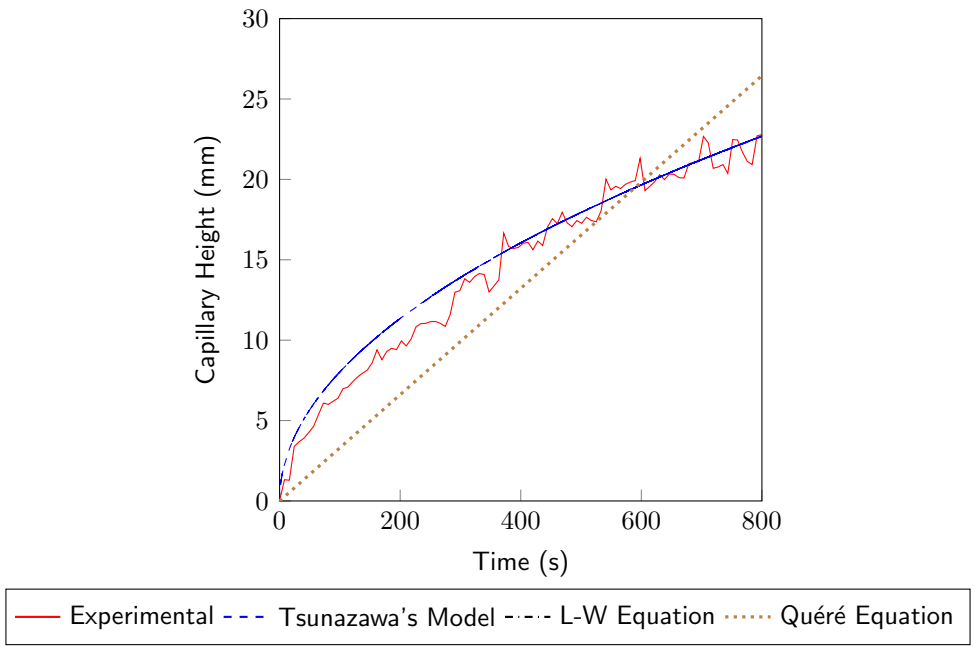


**Figure A1.** An example of the result of fitting the experimental data to the Tsunazawa, Lucas-Washburn, and Quéré model. The data used in this graph was based on water pre-reaction capillary rise of AU sample used in pH 2 acidic capillary rise.

**Table A1.** The $R^2$ Score of fitting Tsunazawa, Lucas-Washburn, and Quéré model. The underlined number shows the best model with the highest $R^2$ values.

| Sample Name | pH | Exp | $R^2$ Score | | |
|---|---|---|---|---|---|
| | | | **Tsunazawa** | **L-W** | **Quéré** |
| **AU** | **2** | Pre- | 1.000 | 0.971 | 0.803 |
| | | Acid | 0.930 | 0.924 | 0.952 |
| | | Post- | 0.978 | 0.969 | 0.852 |
| | **4** | Pre- | 0.986 | 0.985 | 0.904 |
| | | Acid | 0.860 | 0.859 | 0.899 |
| | | Post- | 0.889 | 0.888 | 0.972 |
| **IL100** | **2** | Pre- | 1.000 | 0.883 | 0.926 |
| | | Acid | 0.999 | 0.965 | 0.669 |
| | | Post- | 0.941 | 0.959 | 0.821 |
| | **4** | Pre- | 0.963 | 0.962 | 0.865 |
| | | Acid | 0.951 | 0.951 | 0.919 |
| | | Post- | 0.951 | 0.951 | 0.937 |
| **IL2** | **2** | Pre- | 1.000 | 0.997 | 0.681 |
| | | Acid | 0.967 | 0.962 | 0.891 |
| | | Post- | 0.949 | 0.933 | 0.945 |
| | **4** | Pre- | 0.862 | 0.837 | 0.665 |
| | | Acid | 0.871 | 0.831 | 0.838 |
| | | Post- | 0.988 | 0.900 | 0.840 |
| **SC** | **2** | Pre- | 0.887 | 0.490 | 0.932 |
| | | Acid | 0.962 | 0.899 | 0.916 |
| | | Post- | 0.983 | 0.950 | 0.895 |
| | **4** | Pre- | 0.954 | 0.364 | 0.946 |
| | | Acid | 0.944 | 0.621 | 0.928 |
| | | Post- | 0.927 | 0.191 | 0.955 |
| **BB** | **2** | Pre- | 0.989 | 0.988 | 0.900 |
| | | Acid | 0.914 | 0.913 | 0.975 |
| | | Post- | 0.943 | 0.858 | 0.954 |
| | **4** | Pre- | 0.987 | 0.984 | 0.906 |
| | | Acid | 0.963 | 0.924 | 0.936 |
| | | Post- | 0.951 | 0.942 | 0.926 |
| **BG** | **2** | Pre- | 0.967 | 0.590 | 0.896 |
| | | Acid | 0.971 | 0.926 | 0.839 |
| | | Post- | 0.989 | 0.833 | 0.815 |
| | **4** | Pre- | 0.967 | 0.830 | 0.884 |
| | | Acid | 0.869 | 0.600 | 0.907 |
| | | Post- | 0.976 | 0.811 | 0.840 |

# Appendix B - Flow Regime

The dimensionless time and height were graphed to observe changes in flow regimes during the capillary rise experiment. Figure B1 and B2 display the dimensionless time and height plots for pH 2 and 4, respectively. These plots depict the experimental data fitted with the Quéré (red line with a steep gradient) and Lucas-Washburn (blue line with a gentle gradient) equations, showcasing the transition from inertial to viscous flow—a crucial point identified as the intercept time where these lines intersect. Notably, the impact of acid imbibition significantly altered the intercept time during post-reaction water capillary rise across the samples.

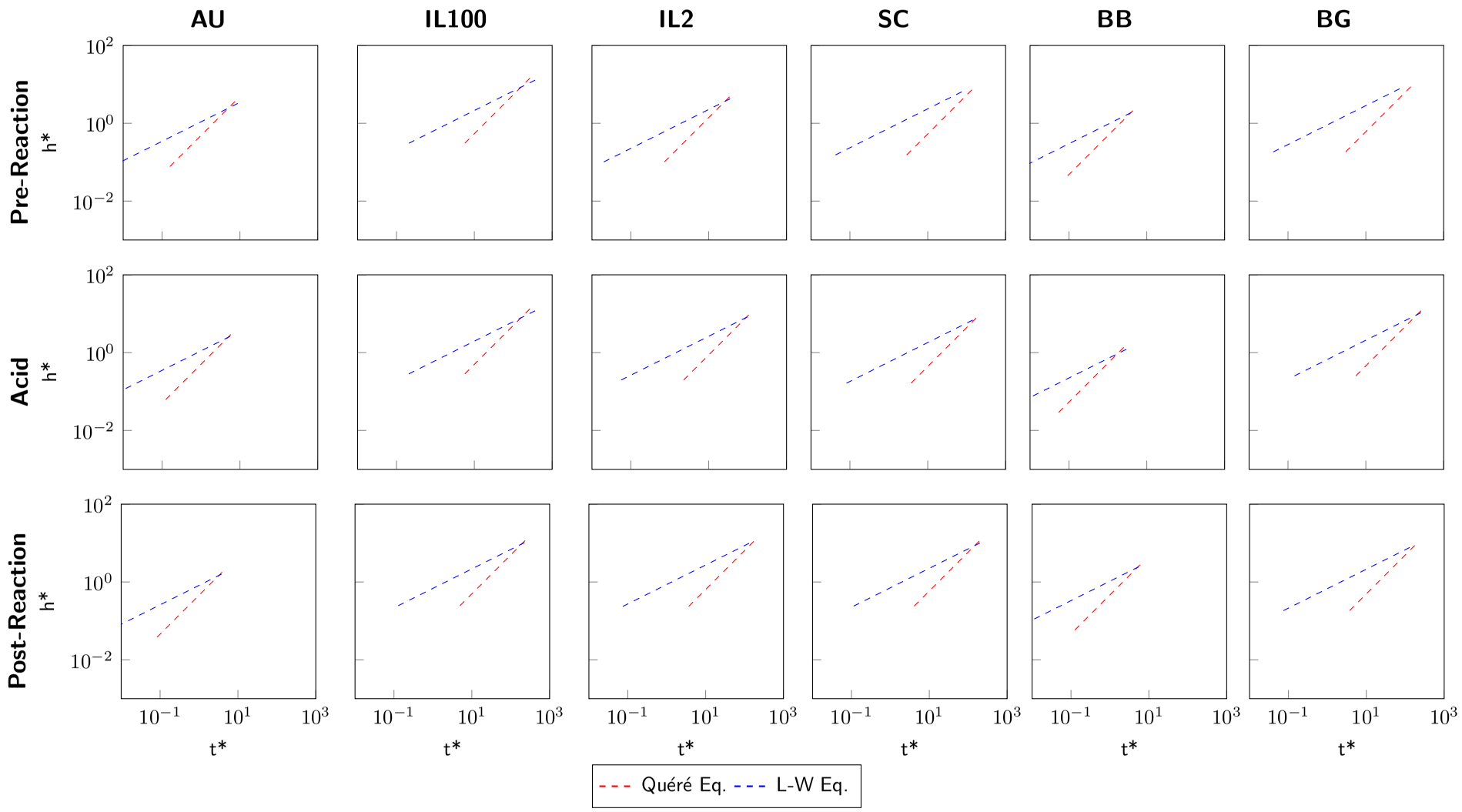


**Figure B1.** The dimensionless height and time for each sample based on the Quéré (1997) and Washburn (1921) equation and using the dimensionless formula from Ichikawa and Satoda (1994) for pH 2. The intersection between two lines indicates the transition from the purely inertial to viscous flow regime and is presented in time units.

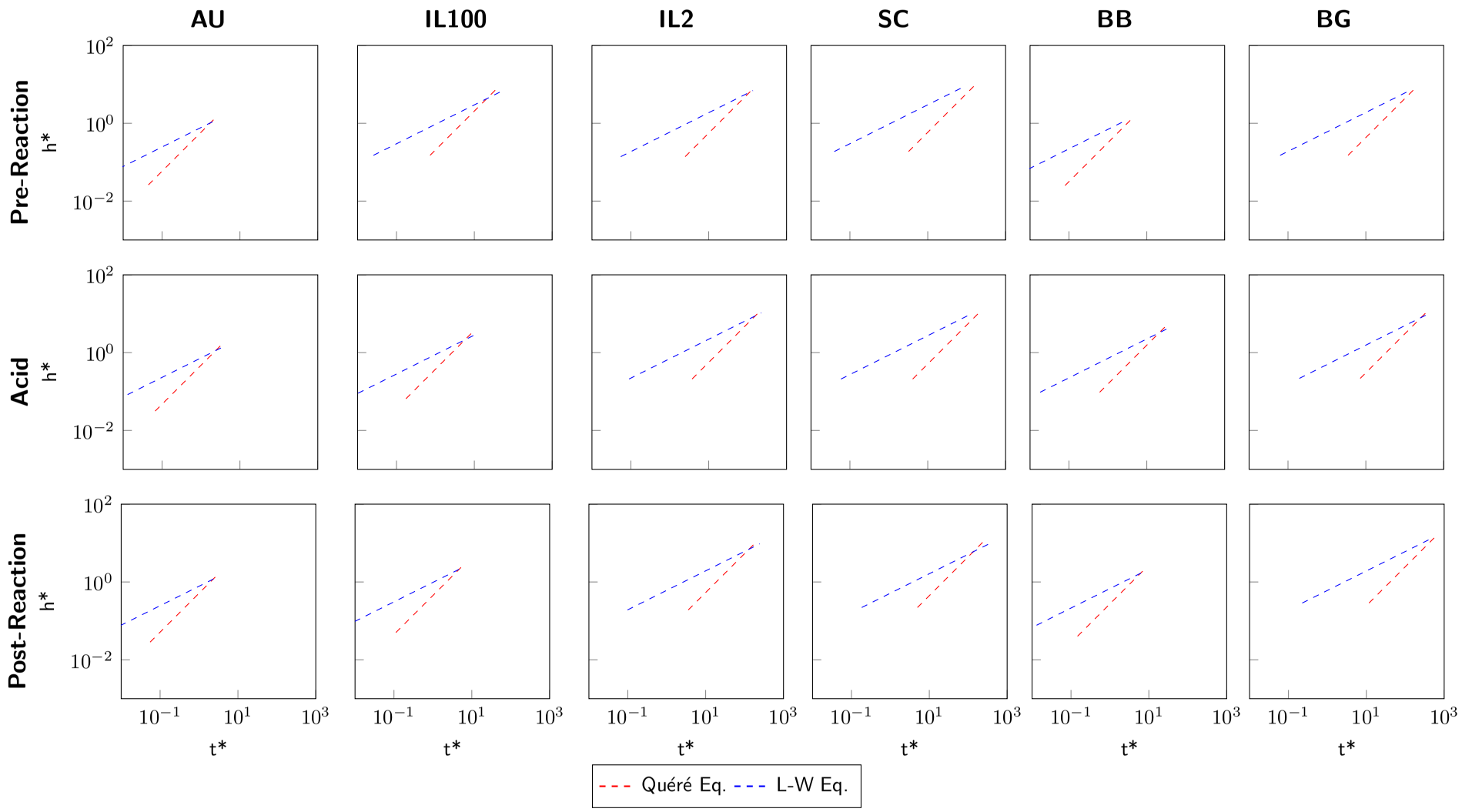


**Figure B2.** The dimensionless height and time for each sample based on the Quéré (1997) and Washburn (1921) equation and using the dimensionless formula from Ichikawa and Satoda (1994) for pH 4. The intersection between two lines indicates the transition from the purely inertial to viscous flow regime and is presented in time units.

# Effect of Acid Strength on Spontaneous Imbibition in Calcareous and Siliceous Rocks

Muhammad Andiva Pratama and Hasan Javed Khan*

*Department of Petroleum Engineering, King Fahd University of Petroleum & Minerals, Eastern Province, Saudi Arabia 34464*

**Abstract**

Capillary rise experiments are conducted in a set of calcareous and siliceous rocks with varying mineralogy and petrophysical properties to understand the coupled impact of reactivity and spontaneous imbibition. A capillary rise experiment is performed in each sample: first with deionized water, then with a dilute acidic solution, and finally again with deionized water and the capillary rise profile for each is recorded. Pre- and post-acid petrophysical properties such as porosity, permeability, pore size distribution, and contact angle are measured for each sample. The mineral makeup of the rocks significantly influences how the acidic fluids penetrate the samples. The primary reactions are the dissolution of Ca and Mg rich minerals which alter the pore network. The higher acid strength results in higher capillary rise in calcareous rocks and results in an increase in the average pore size. The same pH acid results in lower capillary rise in the siliceous rocks and a general decrease in the average pore size is observed. Changes in contact angle indicate increased water affinity in carbonate and reduced affinity in sandstone. The link between capillary interactions and fluid reactivity is often overlooked in fluid flow studies and this research sheds light on the importance of reactivity during spontaneous imbibition, offering insights into dissolution and precipitation processes during capillary flow.

***Keywords*** — spontaneous imbibition; coupled reaction-imbibition; reactive imbibition; mineral dissolution;

*hasan.khan@kfupm.edu.sa

# 1 Introduction

Spontaneous imbibition is a natural occurrence within porous materials driven by fluid surface tension at the fluid-fluid interfaces (Hall and Allinson, 2010). It involves intricate molecular interactions between two fluids situated at a solid surface interface and is presented as the movement of fluids in empty spaces. It is a significant aspect of fluid dynamics (Lu and Likos, 2004) and is observed extensively during in flow in porous media, including but not limited to, hydrocarbon production in unconventional rocks Dehghanpour et al. (2013); Abd et al. (2019); Zhou et al. (2023), solute transport in the vadose zone (Kuhlman et al., 2022; Zahasky and Benson, 2022), CO2 storage (Zahasky and Benson, 2019; Haghi et al., 2021), and ink wicking on paper during inkjet printing (Aslannejad et al., 2017; Yin et al., 2018). Multiple factors influence spontaneous imbibition including fluid properties such as surface tension and density, the contact angle formed at the solid-liquid interface, and the cross-sectional area open to flow (Mason and Morrow, 2013). In a porous medium, the last is analogous to the size of the pore openings (Boduroglu and Bashir, 2022).

The main driver of the fluid during spontaneous imbibition is the capillary forces, which is related to the surface tension/energy, and the resistive force is the viscous force (Mason and Morrow, 2013). The earliest and simplest analytical solution that successfully characterized the capillary rise behavior were separately found by Lucas (1918) and Washburn (1921). These solutions were for a vertical capillary tube with a constant cross-sectional area and without the impact of gravity. A power law relationship was observed between the capillary height and the time, which is represented by the Lucas-Washburn equation (L-W equation):

$$x = \sqrt{\frac{r\sigma\cos\theta}{2\mu} \cdot t} \tag{1}$$

where $x$ is the capillary height $(m)$, $r$ is the pore radius $(m)$, $\sigma$ is the surface tension between the fluid-air interface *(N/m)*, $\theta$ is the contact angle $(^\circ)$, $\mu$ is the viscosity of the fluid $(Pa.s)$, and $t$ is the time $(s)$.

Over time, the L-W equation have been found to be insufficient to model spontaneous

imbibition in porous and permeable medium and different models have been proposed to overcome the specific issues including, but not limited to, addition of gravity force, non-constant cross-sectional area, inclined capillary tubes, and tortousity (Benavente et al., 2002; Fries and Dreyer, 2008a; Tsunazawa et al., 2016; Villagrán Zaccardi et al., 2018; Wang et al., 2022).

While spontaneous imbibition has been extensively studied, there is limited research focused on the reactivity occurring during spontaneous imbibition processes. In contrast, forced imbibition processes involving reactive fluids have been thoroughly observed and modeled. From an experimental perspective, studies have been conducted using reactive fluids in imbibition experiments. For example, Fan et al. (2018) observed that the increase in total dissolved solids resulting from the chemical leaching of brine-dissolved salts could mobilize hazardous radionuclides like radium. Similar to the imbibition process, chemical and biological leaching has also been extensively studied in the context of heavy metal extraction, metal-contaminated environments, and radionuclide-contaminated soils and rocks (Vachon et al., 1994; Avvaru et al., 2008; Bhargava et al., 2015; Córdoba et al., 2009). In the realm of modeling, extensive research has explored various techniques to simulate reactive imbibition processes. For instance, Li et al. (2020) developed a model to capture mineral dissolution and precipitation in shale matrices resulting from acidic hydraulic fracturing fluid imbibition. Meanwhile, Di Donato and Blunt (2004) utilized both analytical and numerical simulations to observe countercurrent imbibition during reactive flow and transport in fractured rocks.

In a previous study (Pratama and Khan, 2024), we studied the impact of fluid reactivity on spontaneous imbibition in calcareous rock samples by conducting a series of capillary rise experiments using deionized (DI) water and diluted HCl at pH 2 and tracking the capillary movement and the evolution of the rock's petrophysical properties. Here we extend the work by employing a combined experimental and modeling approach to investigate how fluid reactivity influences spontaneous imbibition in both carbonate and sandstone formations at different acid strength. We conduct capillary rise experiments using DI water and diluted HCl acid at two pH levels (2 and 4) and observe changes in the petrophysical properties before and after the acid-induced capillary rise as well as the physicochemical changes in the fluid resulting from the reactive interaction be-

tween the rocks and the fluid. Finally, we fit the capillary rise profiles using an extended Lucas-Washburn equation based on the Tsunazawa et al. (2016) model. Connecting capillary interactions with fluid reactivity is frequently overlooked in fluid transport analysis. This research presents new insights on the significance of reactivity concerning spontaneous imbibition timescales as this is crucial for understanding the movement of reactive contaminants through the vadose zone.

# 2 Methodology

## 2.1 Experimental methods

**Sample preparation and petrophysical characterization** Six cylindrical core samples, each measuring 3.8 cm in diameter and 7.6 cm in length, are extracted from different carbonate and sandstone blocks exhibiting diverse petrophysical properties. They are individually labeled according to their formation and the expected permeability value provided by the supplier. *AU* for Austin Chalk, *IL* for Indiana Limestone, *SC* for Sciotto Sandstones, *BB* for Berea Buff, and *BG* for Bandera Gray.

Surface x-ray diffraction (SXRD) is conducted for each sample to determine the mineralogy of the rock surface (Table 1). SXRD is used rather than bulk XRD, which is performed on a powder, to get a more representative mineralogy. All of the carbonate samples exhibit notably high calcite content. In contrast, the composition of the three sandstone samples varies with quartz content between 58 – 98% and the rest mostly feldspar and mica. SC and BB are categorized as pure-quartz sandstones, while BG displays a dolomite composition.

The standard petrophysical properties (porosity, permeability, contact angle, and pore size distribution) are measured twice for each sample: before and after an acid-based capillary rise experiment. Porosity is assessed via a helium porosimeter, liquid permeability using DI water injection, contact angle in a water-rock-air system via the sessile drop method, and pore size distribution via NMR $T_2$ relaxation time measured on a Geospec benchtop rock core analyzer. Each measurement is repeated for consistency, with the

**Table 1.** Mineral compositions for each core samples used in this study based on surface x-ray diffraction (SXRD) analysis.

| Sample Name | Mineral Composition (%) | | | | | | | |
|---|---|---|---|---|---|---|---|---|
| | Calcite | Dolomite | Quartz | Halite | Microcline | Orthoclase | Albite | Muscovite |
| AU | 99.9 | - | 0.1 | - | - | - | - | - |
| IL100 | 100.0 | - | - | - | - | - | - | - |
| IL2 | 100.0 | - | - | - | - | - | - | - |
| SC | - | - | 87.1 | - | - | 4.0 | 6.0 | 2.9 |
| BB | - | - | 97.8 | 0.1 | 1.4 | - | - | - |
| BG | - | 20.5 | 58.6 | - | - | - | 8.4 | 12.4 |

contact angle tested three times on different spots of the same rock surface. The $T_2$ relaxation time, reflecting $H^+$ relaxation in magnetic resonance and proportional to pore size, is estimated using an equation assuming spherical pores (Jaeger et al., 2009):

$$\frac{1}{T_2} = \rho_s \frac{S}{V} = \rho_s \frac{3}{r} \tag{2}$$

where $T_2$ is the spin-spin relaxation time ($\mu s$), $\rho_s$ is the surface relaxivity ($\mu s/s$), $S$ is the individual pore surface area ($m^2$), $V$ is the individual pore volume ($m^3$), $\phi$ is the porosity, and $r$ is the pore radius ($\mu m$).

Separately, two acidic solution was prepared by titrating 12M HCl with deionized (DI) water to get a dilute pH 2 and 4 solution. DI water was used as the baseline fluid.

**Capillary Rise** The capillary rise experiment involves two beakers of different sizes (2 L and 100 ml) connected by a siphon (Figure 1a). The larger beaker is open at the top while the smaller beaker has an aluminum wire mesh placed on the top. Initially, the smaller beaker is empty and the larger beaker is full. Water is siphoned from the larger beaker and flows into the smaller beaker where the fluid level rises. Once the fluid level reaches the top, it passes through the wire mesh and spills over whilst maintaining a constant level at the top of the small beaker. This system will continue until the water level in the larger beaker becomes equal to the height of the smaller beaker, which has

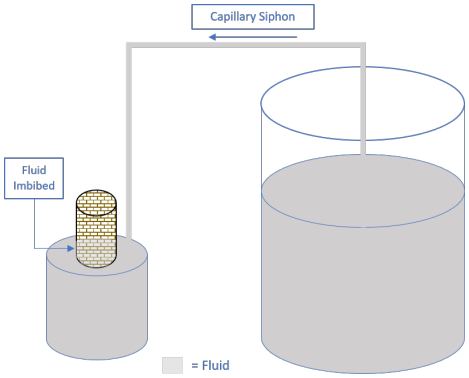


**(a)** Capillary rise experiment schematic

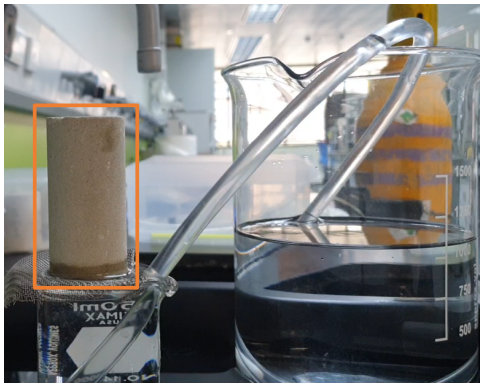

**(b)** Capillary rise experiment setup

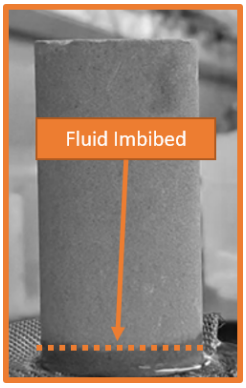


**(c)** Fluid imbibing in the core

**Figure 1.** (a) Schematic representation of the capillary rise experiments. (b) Actual setup for the capillary rise experiment, comprising the larger and smaller beakers, the siphon, the aluminum wire mesh, and the core sample. (c) A grayscale image example showing fluid imbibition in the BG core sample. Fluid height was indicated by varying intensity of colors.

been calculated to take ∼35 minutes.

An oven-dried core sample is placed on top of the wire mesh and the siphon is started (Figure 1b). The water level rises in the beaker until it interacts with the rock sample at a constant fluid-rock interface and starts imbibing into the rock. These experiments are conducted at room temperature and pressure conditions and use air as the displaced fluid.

The imbibition process' capillary height is monitored continuously for 800 seconds using a Samsung Galaxy Note 9 camera equipped with a 12.2 MP ISOCELL 2L3 (SAK2L3) sensor and a resolution of 1920 x 1080 at 30 frames per second. The timescale was selected based on the resolution limitations of the image acquisition instrument and the

observation that the rate of fluid height increment slows down. As the fluid imbibes through the rock and the water saturation changes, a distinct change in color is observed which is captured by the camera (Figure 1c). A custom MATLAB script is utilized to calculate the capillary height by analyzing the differences in color saturation in the video data (Matlab, 2022). Initially, the video is imported as a 3D RGB image stack (spatial dimensions x-y and time dimension) and the central part of the core (a row of 30 pixels forming a rectangle at the respective core height) is isolated for further image analysis. The center of the core is selected due to its minimal curvature within the observation window. A limitation of this method is that the capillary height is measured at only face and assumes the capillary front to be equal spatially, which is usually not the case in porous media (Bartels et al., 2019; Khan et al., 2020).

Subsequently, the RGB image is separated into the individual color channels and the channel (blue) with the most significant contrast between the dry and saturated zones is identified and used for subsequent image analysis. To mitigate contrast inconsistencies caused by external factors like shadows or background movements, the image is initially corrected. Following this correction, global segmentation is performed, with the transition zone's boundary indicating the imbibition front. The capillary height is calculated by taking the difference between the imbibition front and the fluid-rock interface. By comparing the physical length of the sample and the number of pixels it occupies in the image, the pixel size is calculated as 0.15 mm. By analyzing the image stack, the script tracks the temporal evolution of the imbibition front over time, generating a representation of how the capillary rise progresses over time.

The capillary rise experiments are performed in the following sequence. First three repetitions of the capillary rise with DI water is performed. Then the dilute acidic solution (pH 2 or pH 4) is used as the imbibition phase. Finally, another three repetition of the capillary rise with DI water are performed. Following each capillary rise experiment, the mass of the sample is measured, it is then oven dried at 75 °C for 12 hours, and the mass measured again.

**Fluid interaction with the rocks** Due to the reactivity of the acidic DI water, the fluid is expected to undergo physicochemical alterations during the imbibition experi-

ment. But considering the small volume of fluid imbibed during the experiment, the fluid couldn't be extracted from the rock without contamination. Therefore, a separate set of samples were tested in a batch reactor by interacting them with the acidic fluid (pH 2 and pH 4) and the base fluid (pH 7).

Six sets of 15 ml solutions of diluted HCl (pH 2 and 4) and DI water (pH 7) each were prepared and a 1.5 g chip of each sample was introduced to each solution. The solution was allowed to react for 20 minutes and then a fluid sample is collected. To remove any solids from the collected fluid sample, it was passed through a 20-micron filter. Optical emission spectrometry (ICP-OES) was then performed on each reacted and unreacted sample to determine the chemical evolution of the fluid.

## 2.2 Model fitting

**Fitting Process** Experimental capillary rise data was fit to three different spontaneous imbibition models: Lucas-Washburn (L-W) equation (Washburn, 1921) (Eq. 1), Tsunazawa et al. (2016) model (Eq. 3a), and the Quéré equation (Quéré, 1997) (Eq. 3b). Both L-W and Quéré models were selected for their distinct height-time relationships: the former illustrating a logarithmic correlation while the latter shows a linear correlation. Although Tsunazawa's model shows a trend similar to the L-W equation, it further incorporates the gravity force and considers the complexity of the pore structure through tortuosity. Further details about these models can be found in Pratama and Khan (2024).

$$t(x) = -\frac{8\mu\tau}{r^2\rho g}x - \frac{16\sigma \cdot \tau^2 cos(\theta)}{r^3\rho^2\ g^2} log\left(1 - \frac{r\rho g}{2\sigma cos\theta}x\right) \tag{3a}$$

$$h = \sqrt{\frac{2\sigma cos\theta}{\rho R}} \cdot t \tag{3b}$$

where $\rho$ is the fluid density ($kg/m^3$), $\tau$ is the tortuosity, and $g$ is the gravitational acceleration ($m/s^2$).

To perform the fitting, the petrophysical properties of the rock samples served as the fitting parameter: pore size for both the L-W equation (Eq. 1) and the Quéré equation

(Eq. 3b), and pore size along with tortuosity for the Tsunazawa model (Eq. 3a). All the other parameters were derived from laboratory measurements. The resulting fit parameters were then compared between pre-reaction, acid, and post-reaction conditions.

**Flow Regime Analysis** The purely inertial flow is represented by the Quéré (1997) equation (Eq. 3b) as it only considers inertial forces. For the viscous flow, the L-W equation (Washburn, 1921) (Eq. 1) was used. Based on these two equations, Ichikawa and Satoda (1994) determined the flow regime based on the gradient of the dimensionless height and time (Eq. 4) to incorporate the effect of the gas-liquid interface dynamics along the capillary force. The early stage of the capillary rise, which exhibits as a higher gradient, displays purely inertial flow whereas the latter shows purely viscous flow.

$$t^* = \frac{8\mu t}{\rho r^2} \tag{4a}$$

$$h^* = \sqrt{\frac{16\mu^2 h^2}{\rho r^3 \sigma cos\theta}} \tag{4b}$$

# 3 Results and Discussion

## 3.1 Capillary rise

Due to the differences in the initial petrophysical properties for each rock, the capillary rise profile and the maximum height achieved are different after 800 seconds (Figure 2 and 3). Regardless of mineralogy and pH variations, a consistent logarithmic curve shape was observed across all experiments. This aligns with both the L-W and Tsunazawa's models, indicating that capillary height demonstrates a logarithmic relationship with time and a linear relationship with the square root of time ($\sqrt{t}$). In the carbonate sample, AU exhibited the highest capillary height among the samples, reaching a maximum of 20 mm at pH 2 and 28 mm at pH 4, while IL2 displayed the lowest final capillary height for the pre-reaction experiment. Interestingly, within the IL100 sample, distinct behaviors

were observed between the samples used in pH 2 and pH 4 experiments. The pH 2 sample didn't even reach 10 mm, whereas the pH 4 sample showed a significantly higher height. This discrepancy can be attributed to a substantial difference in permeability (Table 2). In sandstones, akin to the carbonates, contrasting behaviors were observed in each sample. BB demonstrated the highest final capillary height, whereas SC and BG exhibited similar final capillary heights, lower than BB. All the samples used for both pH conditions exhibit similar profiles and reach the relatively same final capillary height.

A point to note is that the capillary front measured here is based on one face of the sample only. Generally no changes were observed on the other sides, but nevertheless the height was not exactly the same. Furthermore, this method does not show the fluid level inside the core and therefore assumes that the fluid front is constant across the cross-section.

**Acid-based Capillary Rise** In carbonates, generally, the acid-based final capillary height was found to be greater than the initial water capillary height but with a similar shape. In the pH 2 case, for IL100, it was consistently higher whereas for the other two samples, it was initially lower but increased at a faster rate than with the DI water. The point of crossing, i.e. the time at which the acid capillary rise is equal to the DI water capillary rise, is found to be longer in IL2 ($\sim$530 seconds) compared to AU ($\sim$280 seconds).

In higher pH conditions, the final capillary height post-acid reaction generally exceeded the initial water capillary height, except for AU, which displayed a lower height. However, despite this elevation in higher pH, the incremental change in final height was not as substantial as observed in lower pH environments.

Apart from the maximum capillary height, the rate of capillary rise during the acid-based experiments also differed from that observed during the water-based capillary rise. Lower pH levels exhibited a pattern where the capillary rate was initially slower, gradually increasing to eventually surpass the water capillary height. Conversely, in higher pH conditions, the capillary rate remained consistently lower. This resulted in a reduced increment of capillary height in IL100 and IL2 and an overall lower capillary height in AU.

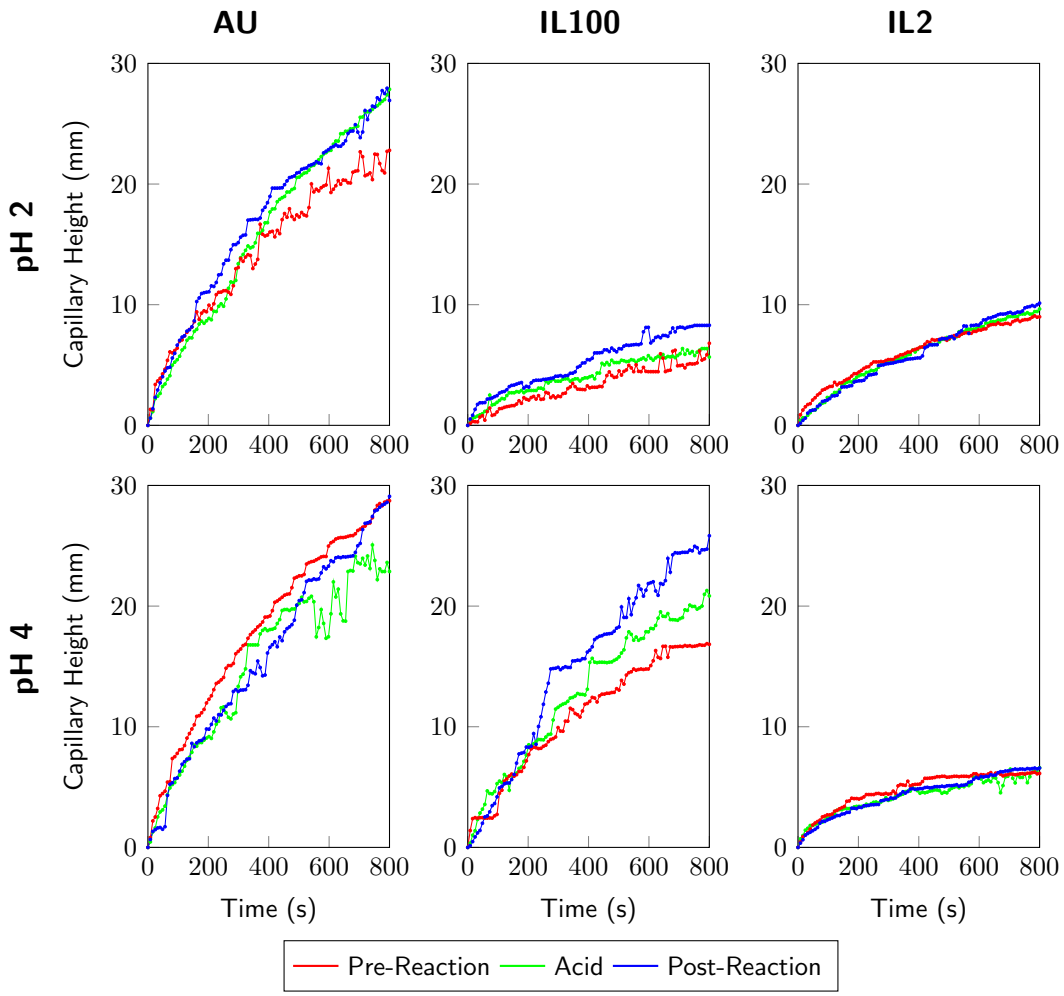


**Figure 2.** The comparison of the capillary height (time-dependent) in every carbonate core sample for each condition. The pre- and post-reaction are the capillary height observed through the DI water-based capillary rise experiment before and after the acid-based capillary rise experiment. Acid was the capillary height that was observed in acid-based capillary height.

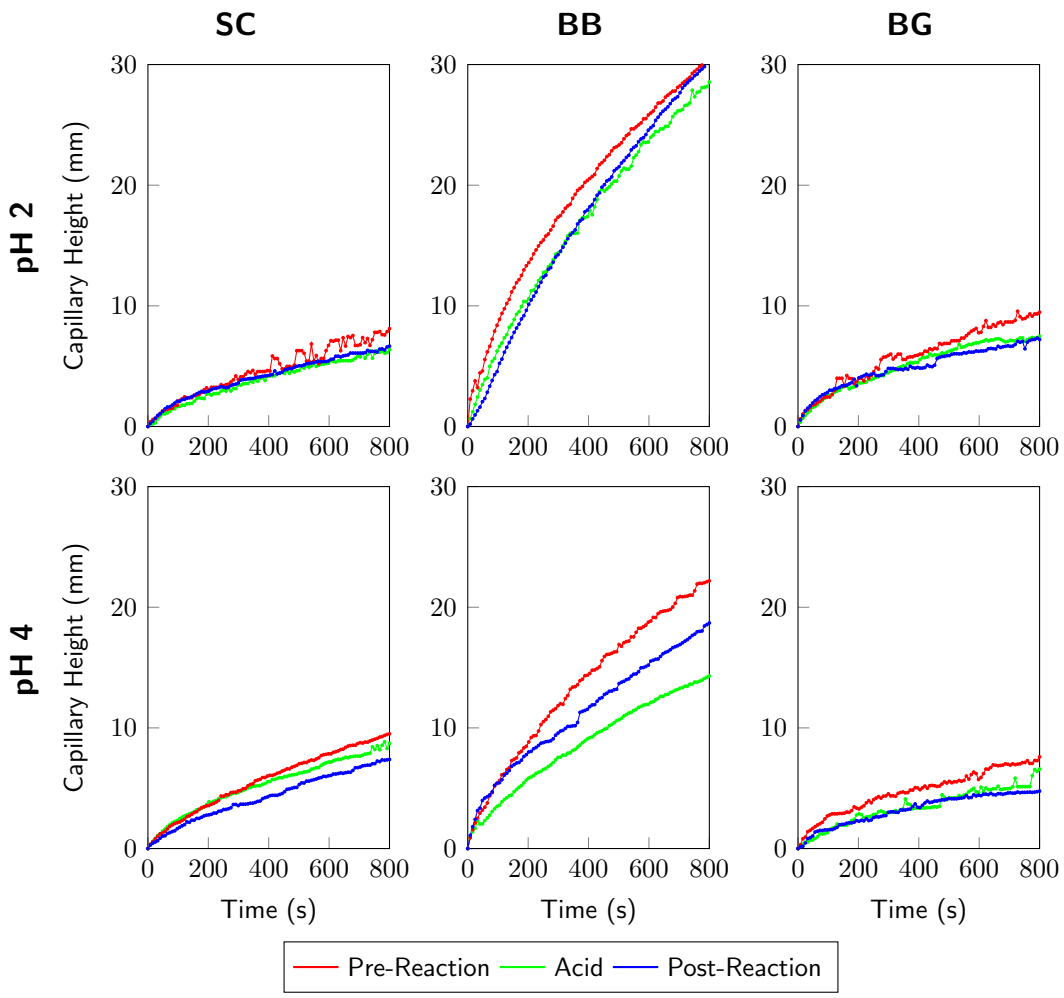


**Figure 3.** The comparison of the capillary height (time-dependent) in every sandstone sample for each condition. The pre- and post reaction was the capillary height observed through the DI water-based capillary rise experiment before and after the acid-based capillary rise experiment. Acid was the capillary height that was observed in acid-based capillary height.

In sandstones, conversely, the acid-based final capillary height is consistently lower than the pre-reaction water capillary height (Figure 3). It was observed that the acid capillary height does not surpass the initial water capillary height within the experimental time frame.

In higher pH, the decrease is more significant than the lower pH. The highest decrease relative to the water capillary height was observed in BB, as the acid final capillary height is reduced by more than 30 %, followed by BG and SC. Since the main parameters that driven the capillary rate is contact angle and pore size, the acid able to modify these two parameters and leads to lower capillary height.

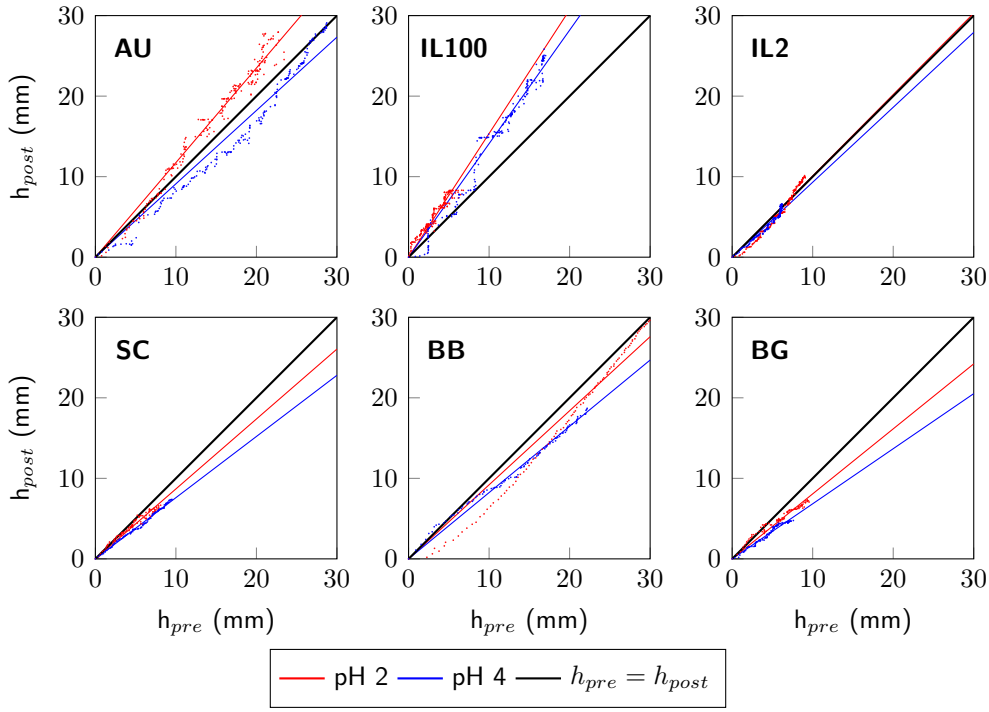


**Figure 4.** Comparison of the water capillary height before and after the acid imbibition for each core sample and for both acidic conditions. The black line indicates $h_{pre} = h_{post}$. Lines which lie above this line indicate that post-reaction capillary rise was higher than the pre-reaction capillary rise.

**Effect of Acid on the Water Capillary Height** The interaction between the acid and rock caused changes in the pore network and structure, which, in turn, could also affect the water's capillary rise. The interpolation illustrating the correlation between the water capillary heights before and after acid imbibition is depicted in Figure 4. In carbonates, for both pH levels, the most prominent change is observed in IL100, where the post-reaction maximum capillary height is ∼50 % higher than the pre-reaction and the post-reaction has a consistently higher height. AU initially shows the same height for pre- and post-reaction, but it got separated in the later stages and the post-reaction shows significantly higher end-point capillary height.

In carbonate samples, the pH notably influences the correlation between pre- and post-reaction water capillary rise. Across all three samples, a trend emerges: at lower pH levels, the post-reaction water capillary height consistently surpasses the pre-reaction level. This is visually evident as the red line consistently lies above the black line, which is the unity gradient line. Conversely at higher pH, more diverse behavior was observed. In the cases of AU and IL2, the post-reaction water capillary rise was lower than the pre-reaction rise. However, in the case of IL100, the post-reaction water capillary rise remained higher than the pre-reaction rise. Despite these variation, a consistent behavior emerged across the samples: a higher pH exhibits a lower gradient and a lower pH exhibits a higher gradient.

In sandstones, a distinct behavior was observed, as for all of the acidic conditions, the post-reaction water capillary height was lower than the pre-reaction water capillary rise. The reduction was observed to be the highest in BG sample, followed by SC and BB. Not only the final height, the water capillary rise profile was also changed. In the AU sample, the water capillary rise profile was shown to be lower than the pre-reaction water capillary rise at the beginning, but at some time, it will overlap and get higher than the pre-reaction one. The same thing happened with the IL2 sample, but the overlapping point is much later compared to the AU sample. Overall, all of the samples showed a consistent behavior, a higher end-point capillary height compared to the water pre-reaction capillary height. For the higher pH, the overlapping point happened later than in the lower pH. However, the overlap is not observed in the sandstone cases, as from the beginning, the profile was distinct from each other.

## 3.2 Petrophysical properties alteration

The petrophysical properties (porosity, permeability, contact angle, and pore size distribution) and mass for all the samples are observed to change due to the effect of the reaction with acid during the acid-based spontaneous imbibition process. Since these measurements were done on the actual samples before and after reaction, it is possible that a little mass was lost during the loading/unloading of the sample from the porosimeter and liquid permeameter.

**Mass and porosity** Although not statistically significant, comparing the core sample's mass and porosity before and after the acid reaction was nonetheless significant. The mass and porosity have a direct relationship: the mass decreases as the void areas inside the core samples grow and the comparison of it is shown in Table 2.

Small changes in the mass and porosity are expected as the fluid is only permeating to a maximum of 30 mm. Considering the case of SC at pH 2, the maximum fluid height attained is 10 mm (Figure 3). So assuming a 1% change in the porosity throughout the imbibed zone, the change in the porosity for the whole rock sample will only be 0.13%.

For low pH, consistent mass reduction was observed across all carbonate samples. AU exhibited the maximum mass decrease, while IL2 showed the lowest reduction. The average reduction across all samples was less than one percent (%), not exceeding 1.6 g. As mass directly correlates with porosity, this validates the increment in porosity. All carbonate samples experienced increased porosity, with AU demonstrating the highest change (0.73 %) and IL2 the smallest (0.15 %). None of the samples showed a significantly large change; all were under 1 %.

Interestingly, at higher pH, variations emerged within the carbonate samples. AU still experienced mass reduction, albeit smaller than in the low pH environment (0.3 g). Both IL100 and IL2 showed a marginal increase in mass (around 0.1 g). However, all samples displayed an increase in porosity, with IL2 exhibiting the highest increment (0.17 %).

In sandstones, akin to the carbonate samples, mass reduction was observed across all samples. BG exhibited the highest mass reduction, followed by BB and SC. However,

**Table 2.** Petrophysical properties comparison between pre- and post-acid reaction including the error of the measurement. Each sample experienced changes in the pore scale and opening up of pore spaces, shown by the reduction of mass and increment of the porosity, while the permeability is increased in most of the samples, and reduced in IL30.

| **Property** | **pH** | **Condition** | **Sample Name** | | | | | |
|---|---|---|---|---|---|---|---|---|
| | | | **AU** | **IL100** | **IL2** | **SC** | **BB** | **BG** |
| **Mass (g)** | **2** | Pre- | 161.78 ± 0.01 | 188.42 ± 0.01 | 185.74 ± 0.01 | 180.81 ± 0.01 | 182.14 ± 0.01 | 188.01 ± 0.01 |
| | | Post- | 160.27 ± 0.01 | 187.91 ± 0.01 | 185.45 ± 0.01 | 180.72 ± 0.01 | 181.80 ± 0.01 | 187.46 ± 0.01 |
| | **4** | Pre- | 161.92 ± 0.01 | 195.60 ± 0.01 | 185.61 ± 0.01 | 180.60 ± 0.01 | 180.81 ± 0.01 | 205.3 ± 0.01 |
| | | Post- | 161.61 ± 0.01 | 195.71 ± 0.01 | 185.71 ± 0.01 | 180.65 ± 0.01 | 180.67 ± 0.01 | 205.59 ± 0.01 |
| **Porosity (%)** | **2** | Pre- | 27.51 ± 0.10 | 16.05 ± 0.10 | 17.11 ± 0.05 | 17.82 ± 0.10 | 22.12 ± 0.10 | 21.68 ± 0.05 |
| | | Post- | 28.30 ± 0.06 | 16.23 ± 0.03 | 17.26 ± 0.06 | 17.80 ± 0.06 | 22.38 ± 0.03 | 22.39 ± 0.06 |
| | **4** | Pre- | 28.80 ± 0.10 | 15.54 ± 0.10 | 17.22 ± 0.05 | 18.68 ± 0.10 | 21.10 ± 0.10 | 14.32 ± 0.05 |
| | | Post- | 29.07 ± 0.06 | 15.66 ± 0.03 | 17.39 ± 0.06 | 19.46 ± 0.06 | 21.79 ± 0.03 | 14.61 ± 0.06 |
| **Permeability (mD)** | **2** | Pre- | 41.15 ± 0.15 | 3.80 ± 0.70 | 33.82 ± 0.25 | 4.38 ± 0.15 | 63.72 ± 0.70 | 11.94 ± 0.25 |
| | | Post- | 45.27 ± 0.10 | 5.59 ± 0.01 | 30.67 ± 0.10 | 4.97 ± 0.10 | 119.22 ± 0.01 | 13.43 ± 0.10 |
| | **4** | Pre- | 28.34 ± 0.15 | 289.60 ± 0.70 | 31.87 ± 0.25 | 4.37 ± 0.15 | 256.67 ± 0.70 | 14.88 ± 0.25 |
| | | Post- | 49.34 ± 0.10 | 85.78 ± 0.01 | 31.66 ± 0.10 | 9.05 ± 0.10 | 28.74 ± 0.01 | 24.83 ± 0.10 |

these reductions were relatively insignificant, none surpassing 0.6 g. Notably, porosity did not directly correlate with mass reduction, as SC showed reduced porosity while BB and BG displayed increments. BG showed the largest change, with a porosity increase of 0.71 %. This change was nearly as high as the highest increment in carbonate samples (AU with 0.73 %). This occurrence might be attributed to reactive minerals in the BG samples, potentially driving mineral dissolution as explained in the subsequent subsection.

At higher pH, variations in mass changes persisted. SC and BG exhibited mass increments, while BB showed mass reduction. Intriguingly, all sandstone samples displayed increased porosity. SC exhibited the largest porosity increment (0.78 %), followed by BB (0.69 %) and BG (0.31 %).

**Permeability** The alteration in permeability exhibited distinct behaviors. Most of the carbonate samples at lower pH exhibited increased permeability due to the acid reaction (Table 2). However, a noticeable and significant drop in permeability (4.6 mD or -13.3 %) occurred in IL2. AU displayed a permeability change of 3.8 mD (or +9.2 %) while IL100 showed an increase of 1.1 mD (or +24.4 %). Although the absolute change in IL100 was lower than the others, the relative changes was the highest among all. At higher pH, only the AU sample experienced an increase in permeability, whereas IL100 and IL2 showed a drop. Notably, a substantial decrease was observed in IL100 with post-reacted permeability reaching only 30% of the initial permeability, or a drop of ∼30%.

In sandstones at lower pH, all samples exhibited permeability increments. BB displayed the highest change at 55.5 mD (or +87.1 %), followed by BG with 1.49 mD (or +12.5 %) and SC with 0.59 mD (or +13.5 %). Similarly at higher pH, most samples exhibited increased permeability except for BB, which displayed a significant reduction (a decrease of 227.9 mD or -88.8 %). For SC and BG, the increments were higher compared to the lower pH samples.

The comparison between pre- and post-reaction permeability are plotted on a log-log plot to assess deviations from the line $k_{pre} = k_{post}$ (Figure 5). Points lying above the unity gradient line (black) indicate samples where the permeability has increased as a result of the acid imbibition, whereas points lying below the unity gradient line indicate

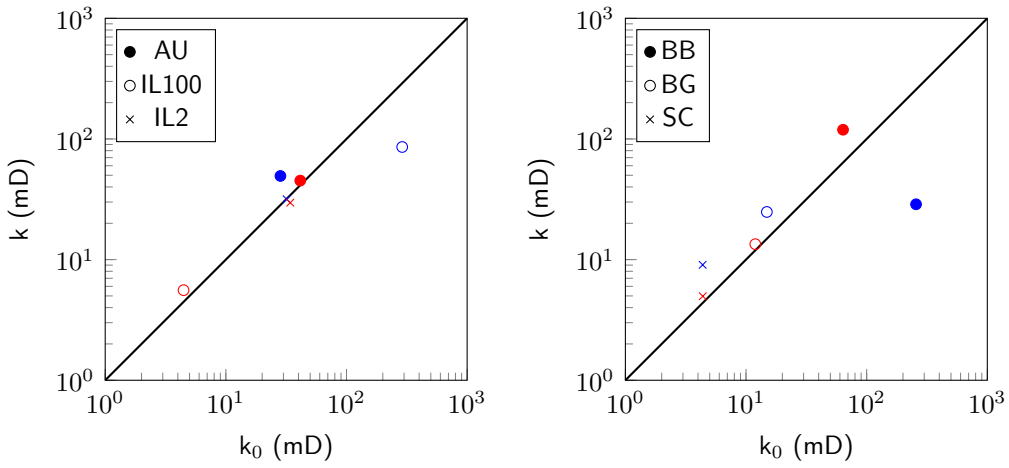


**(a)** Carbonates **(b)** Sandstones

**Figure 5.** Comparison of permeability before and after acid imbibition at pH 2 (red) and pH 4 (blue). The black line is the unity gradient line. Point lying north of the unity gradient line indicate that the permeability has increased after the acid imbibition.

samples where the permeability has decreasesd as a result of the acid imbibition. In carbonate samples, most values did not significantly deviate from the unity gradient line, indicating relatively insignificant changes (Figure 5a). Only in IL100 at pH 2 was there a high deviation. Additionally, higher pH conditions showed more significant deviations compared to lower pH.

Conversely, sandstones displayed more scattered and deviated permeability results (Figure 5b). The correlation between pH and permeability changes was notably clearer in sandstones, where higher pH (blue) induced greater permeability alterations. BB exhibited the most significant permeability alteration amongst the sandstone samples.

**Pore Size Distribution** The pore size distribution was estimated based on the distribution of $T_2$ relaxation time (Equation 2). The surface relaxivities are highly dependent on the magnetic impurities present inside the rock, but since none of these samples showed any sizeable quantity of the magnetic impurity (Table 1), the surface relaxivity found in the literature are utilized: 39.65 $\mu$m/s for Indiana Limestone (IL) (Lawal et al., 2020), 23.3 $\mu$m/s for Austin Chalk (AU) (Benavides et al., 2020), 29.6 $\mu$m/s for Sciotto Sandstone (SC) (Mitchell and Fordham, 2014), 65 $\mu$m/s for Bandera Gray (BG) (Lucas-Oliveira et al., 2020), and 21 $\mu$m/s for Berea Buff (BB) (Lucas-Oliveira et al., 2020).

Two phenomena were observed through the pore size distribution comparison: pore enlargement (increment in the mean of the distribution) and pore size reduction in the larger pore sizes (Figures 6 and 7). A slight variation was observed in the changes in the mean pore size distribution. As explained previously, the changes expected in the samples are small since the imbibed zone is considerably small. In some instances it is only ∼13% of the total length of the rock sample.

At lower pH, an increase in the mean of the distribution was observed in IL100 (from 14.98 to 15.68 $\mu$m) and AU (from 3.57 to 3.69 $\mu$m), while a reduction was observed in IL2 (from 15.35 to 14.53 $\mu$m). The largest pore spaces in each sample were notably reduced. This strongly indicates simultaneous dissolution and precipitation occurring in different parts of the pore systems. Alterations were also observed in smaller pore spaces, with new pore spaces generated, leading to an expanded distribution within the smaller pores.

In higher pH, the most notable observation was the shift of the plot to the right, indicating the enlargement of pore spaces and it is consistently observed across all carbonate samples. Unlike the lower pH observations, there was no clear reduction observed in large pore spaces, suggesting a lack of pore size reduction. However, in smaller pore sizes, reductions were observed, indicating that mineral dissolution could occur at both lower and higher pH, while mineral precipitation was observed only at lower pH.

In sandstones at lower pH, the overall distribution shifted to the left for all samples. The most notable shift occurred in SC, followed by BG and BB. Changes were also observed in smaller pore sizes. In the micropore system ($< 10^{-1}\mu$m), an increase in the number of pores was noted, while in the mesopore system (between $10^{-1}\mu$m and $10^{0}\mu$m), a reduction in the number of pores was observed. This suggests ongoing mineral dissolution, albeit less prominent compared to carbonate. Additionally, factors such as mineral precipitation or clay swelling might contribute to the reduction in pore sizes.

At higher pH, a contrasting pattern emerged. The pore size distribution shifted to the right, indicating pore enlargement across all sandstone samples. Unlike lower pH conditions, in smaller pore sizes, the number of pores decreased, signifying the enlargement of pores interacting with fluids.

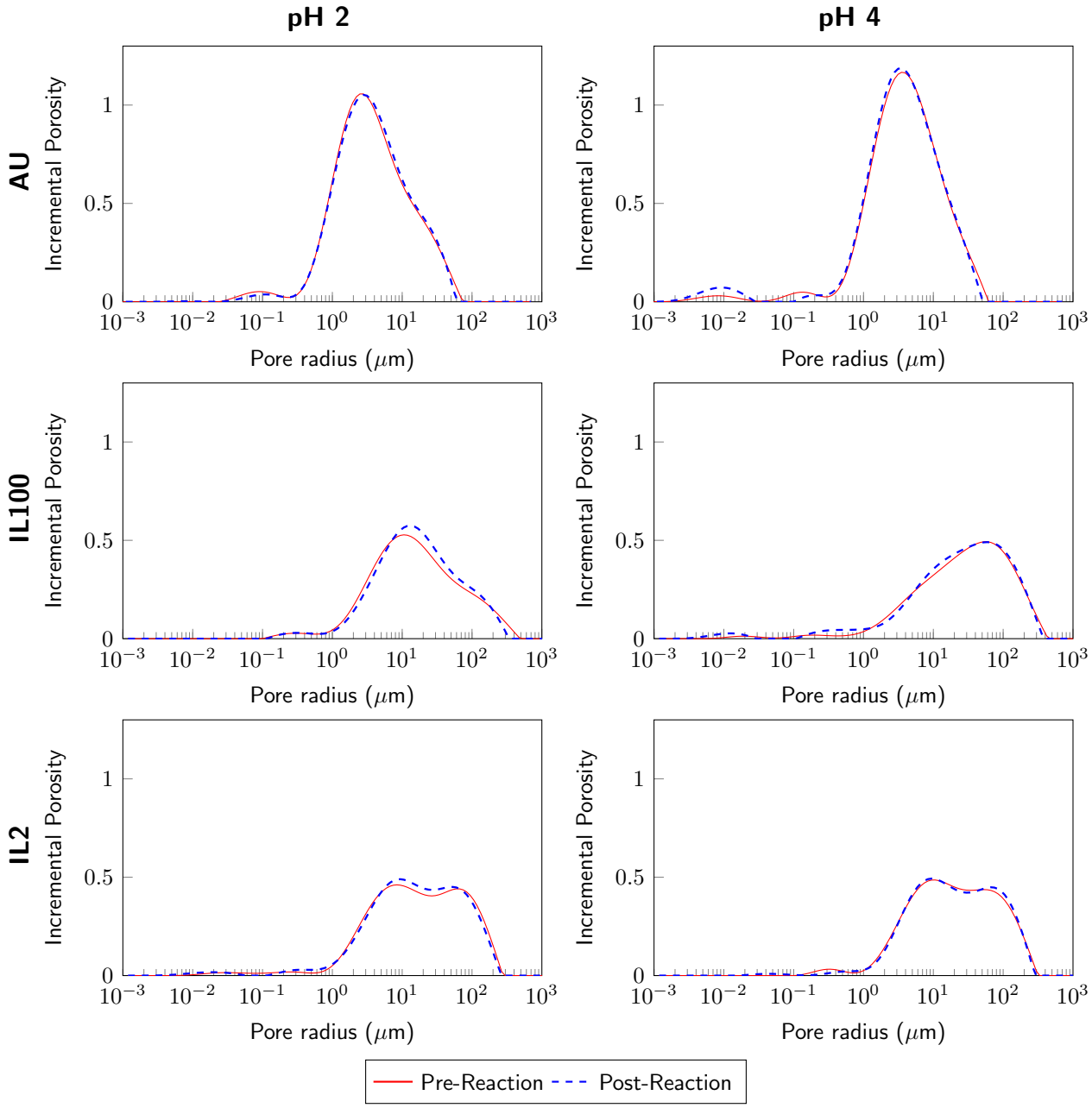


**Figure 6.** Pore size distribution for each carbonate sample based on the nuclear magnetic resonance (NMR). The correlation between the $T_2$ relaxation time and pore radius is based on Equation 2.

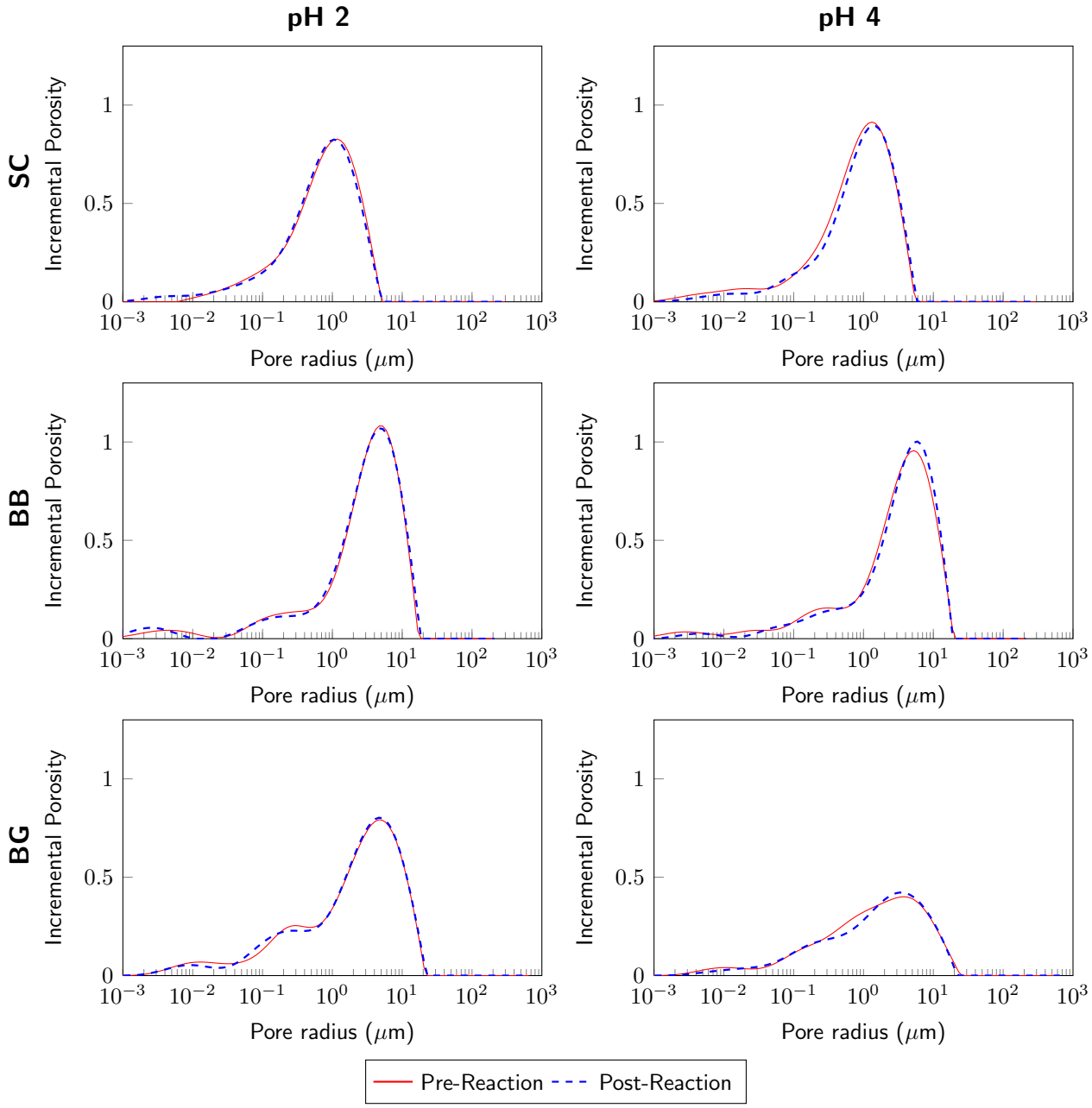


**Figure 7.** Pore size distribution for each sandstone sample based on the nuclear magnetic resonance (NMR). The correlation between the $T_2$ relaxation time and pore radius is based on Equation 2.

**Wettability** The wettability of the samples were measured using a Sessile drop method where a drop of the fluid is dropped from a tip on to the solid surface and the contact angle is measured. This contact angle is the apparent contact angle for a static fluid and can be different that the dynamic contact angle that the fluid observes while moving in the porous media. Care has been taken in handling the rock surface as well to make sure that it does not come in direct contact with the user's hand as the bodily oil on the fingers can significantly alter the contact angle.

The wettability of the rocks was observed to change due to the acid/rock interaction. In carbonates, at lower pH, a significant reduction in the contact angle was observed in each sample, rendering the wettability more water-wet (Figure 8a). The most considerable change was observed in AU, while the least change occurred in IL2. Conversely, at higher pH some variations emerged (Figure 8b). The reduction in contact angle was solely observed in AU, whereas in IL100 and IL2, the contact angle increased. This suggests that for IL100 and IL2, the samples were less water-wet after the acid interaction.

For sandstones, the observed behavior was converse to that in carbonates (Figure 8). The contact angle consistently increased due to the effect of acid interaction. This behavior was observed in both low and high pH acids, with pH 4 resulting in a less pronounced increase than pH 2. The most substantial increment was observed in SC, indicating that sandstones tend to become less water-wet after the acid interaction.

Even though the time scale of the interaction is considerably low, it has been previously shown that the acid could alter the wettability of the mineral surfaces, specifically calcite (Standnes and Austad, 2003). For instance, Rezaei Gomari and Hamouda (2006) showed that under 15 minutes of soaking time, the wettability still could be altered. The alteration in permeability could also be attributed to the change in wettability, wherein the water-wet condition influences the relative permeability of DI water (Owens and Archer, 1971). Given that DI water was employed in the permeability measurements, this change in wettability could potentially impact the liquid permeability.

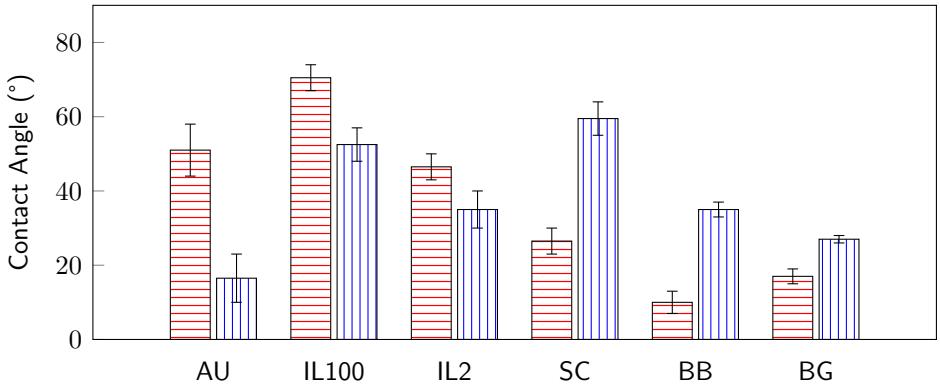


**(a)** pH 2

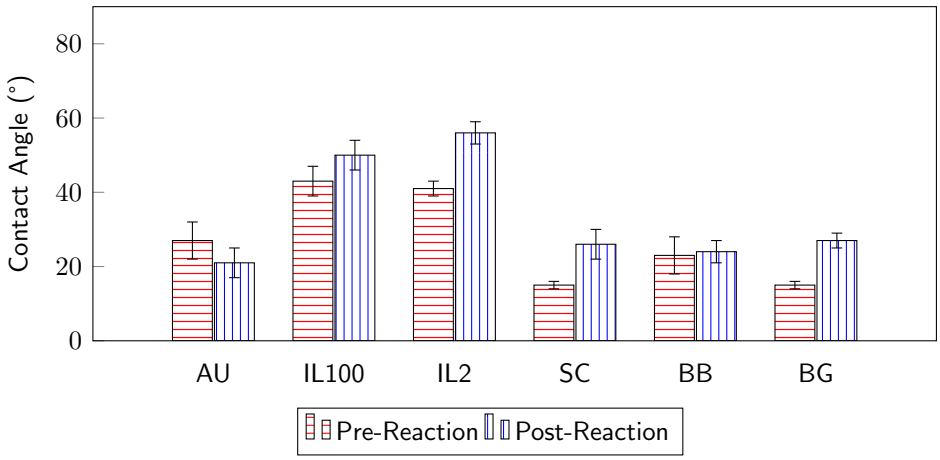


**(b)** pH 4

**Figure 8.** Comparison of the water-air contact angle for all pre- and post-acid reaction core samples for (a) pH 2 and (b) pH 4 sample.

## 3.3 Model Fitting Results

The experimental capillary rise data were fit to three different models: Tsunazawa (Tsunazawa et al., 2016), Lucas-Washburn (L-W) (Cai et al., 2021), and Quéré (Quéré, 1997) using the Levenberg-Marquardt algorithm (Moré, 1978). The fitting method and results for all the methods are shown in Appendix A. Tsunazawa's model was able to fit the water imbibition experimental data better (higher $R^2$ value) compared to the Lucas-Washburn and Quéré equation. Table 3 displays the best-fit for three parameters obtained from Tsunazawa's models: pore size, tortuosity, and contact angle.

Across the carbonate samples, a consistent reduction in pore size was observed in the water pre-reaction, acid spontaneous imbibition, and water post-reaction stages, except for the IL100 sample at pH 4. Notably, at lower pH, the simulation indicated the most significant change in the IL2 sample, while the IL100 sample displayed the least alteration in pore size. Minor changes in tortuosity were evident in all samples: IL100 and IL2 displayed a slight decrease, whereas AU exhibited an increasing trend. This trend persisted at higher pH levels, except for IL100, where the tortuosity decreased for water post-reaction but increased during acid imbibition. Notably, at lower pH levels, both AU and IL2 showcased higher pore size and tortuosity changes compared to other conditions.

In sandstones, notable variations were observed in the results of the fitting parameters. At lower pH levels, both pore size and tortuosity showed reductions in water post-reaction for SC and BB, while pore size and tortuosity increased during acid imbibition. Conversely, BG exhibited the inverse behavior: pore size decreased during acid imbibition and enlarged in water post-reaction. However, tortuosity consistently increased across all scenarios. At higher pH levels, a consistent reduction in pore size was observed in both acid and water post-reaction for all samples, with a more pronounced reduction observed in water post-reaction. Tortuosity consistently increased, showing a higher increase in water post-reaction. Notably, no clear correlation was evident between pH levels and the observed changes in each of the fitting parameters.

**Table 3.** The fitting parameters based on Tsunazawa's model (Tsunazawa et al., 2016). The fitting parameters in this calculation is the pore size and the tortuosity with an adjustment from the contact angle based on the laboratory measurements and error during the measurement.

| **Sample Name** | **pH** | **Water capillary rise (Pre-acid)** | | | **Acid capillary rise** | | | **Water capillary rise (Post-acid)** | | |
|---|---|---|---|---|---|---|---|---|---|---|
| | | $r$ (µm) | $\tau$ | $\theta$ (°) | $r$ (µm) | $\tau$ | $\theta$ (°) | $r$ (µm) | $\tau$ | $\theta$ (°) |
| **AU** | 2 | 326.63 | 2.89 | 62.76 | 328.91 | 2.90 | 50.00 | 259.42 | 3.16 | 16.74 |
| | 4 | 529.51 | 4.08 | 28.50 | 464.60 | 4.35 | 26.17 | 493.45 | 4.11 | 23.55 |
| **IL100** | 2 | 81.29 | 4.97 | 69.46 | 53.69 | 4.23 | 62.6 | 70.25 | 4.23 | 53.4 |
| | 4 | 157.95 | 3.37 | 44.73 | 288.07 | 3.47 | 51.77 | 330.23 | 3.25 | 45.90 |
| **IL2** | 2 | 184.77 | 4.59 | 70.75 | 80.39 | 3.60 | 59.63 | 79.81 | 3.85 | 51.43 |
| | 4 | 65.20 | 5.57 | 44.73 | 55.41 | 4.30 | 57.77 | 55.59 | 4.84 | 50.32 |
| **SC** | 2 | 60.82 | 5.16 | 27.93 | 61.26 | 5.88 | 40.69 | 55.55 | 4.26 | 61.53 |
| | 4 | 56.19 | 4.28 | 15.62 | 52.89 | 4.34 | 21.03 | 51.93 | 5.13 | 27.49 |
| **BB** | 2 | 363.06 | 3.36 | 9.98 | 493.58 | 4.18 | 20.26 | 320.85 | 3.02 | 32.62 |
| | 4 | 402.33 | 4.60 | 22.61 | 165.57 | 4.69 | 24.04 | 296.61 | 4.80 | 26.13 |
| **BG** | 2 | 55.96 | 4.23 | 17.84 | 45.78 | 4.56 | 23.19 | 57.59 | 5.24 | 28.64 |
| | 4 | 46.99 | 4.85 | 15.65 | 36.90 | 5.72 | 18.83 | 30.95 | 5.85 | 23.13 |

## 3.4 Mineral dissolution and precipitation

**Carbonates** Since all of the carbonate samples dominantly consist of calcite (Table 1), the reaction between the $H^+$ and $CaCO_3$ is the main reaction that drives the porosity alteration (Eq. 5). Dissolution occurs when the calcite solid surface dissolve due to the brine interaction at undersaturated conditions while precipitation deposits calcite solid in oversaturated conditions. Both of these processes result in the alteration of the petrophysical properties of the rock.

$$CaCO_{3(s)} + 2H^{+}{}_{(aq)} \longleftrightarrow Ca^{2+}{}_{(aq)} + H_2O_{(l)} + CO_{2(g)} \tag{5}$$

The dissolution process was tracked through the ICP-OES analysis of the ionic composition after the rocks' interaction with acidic fluid (Figure 9a). The presence of $Ca^{2+}$, particularly noticeable in lower pH conditions, strongly suggests an active dissolution process. This ion exhibited consistent and similar concentration levels across all carbonate samples. However, the varying final concentrations also imply differing reaction rates depending on the pH levels. Lower pH shows a higher reaction rate. These reaction rate condition also have been consistently observed in the previous studies (Alkattan et al., 1998, 2002; Rabie et al., 2011; Gray et al., 2018).

Additionally, the consistent detection of $Mg^{2+}$ across all samples raises the possibility of low amounts of Mg-enriched calcites being present, although none of which were observed in surface XRD (Table 1). Mg could also be present in the calcite minerals as impurities and could react with acid, resulting in the generation of $Ca^{2+}$ and $Mg^{2+}$ (Eq. 6). It is conceivable that any Mg content might be minimal or confined to regions that weren't analyzed via surface XRD. This aligns with the ionic composition data, where the concentration of $Mg^{2+}$ remained below 10 mg/L, suggesting a very low amount of Mg impurities.

Even with a low acid concentration, calcite dissolution could still be prominent (Alkattan et al., 1998). In the micro-scale, a smoother grain surface has a strong indication that calcite dissolution happened, which was previously observed by Järvinen et al. (2012). On the other hand, Singh et al. (2018) observed the increment of porosity distribution

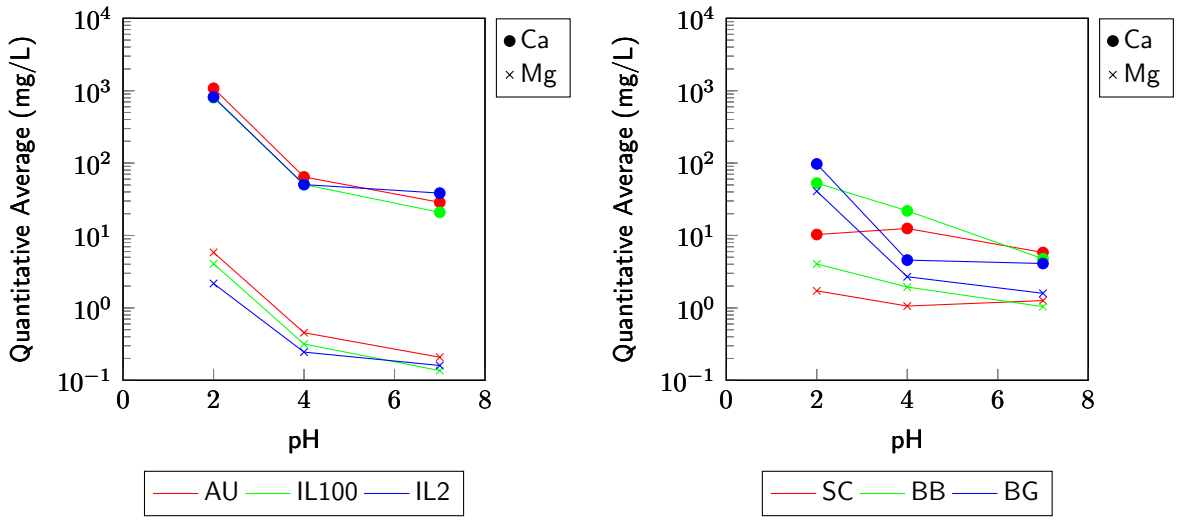


**(a)** Carbonates **(b)** Sandstones

**Figure 9.** Comparison of the $Ca^+$ and $Mg^+$ ion composition of the fluid after the fluid-rock interaction.

during the injection of reactive $CO_2$-saturated brine.

In addition to the dissolution process, the presence of calcite precipitation has been noted, particularly evident in pore size reduction within larger pores, as observed through NMR and Tsunazawa's fitting parameters. This phenomenon is primarily attributed to oversaturated calcium ions and carbon dioxide ($CO_2$) gas, byproducts generated during the dissolution process (Eq. 5). As these components were transported with the fluids to other locations, simultaneous reactions occurred, leading to calcite precipitation in different areas of the sample. This observation is consistent with the findings of Eloneva et al. (2008), who also highlighted how dissolution byproducts can trigger calcite precipitation.

**Sandstones** In sandstones, although not as predominant as in carbonate samples, a noticeable presence of $Ca^{2+}$ and $Mg^{2+}$ was detected in the fluid's ionic composition (Figure 9b). This observation is particularly understandable in BG due to its rock composition containing a significant proportion of dolomite (Eq. 6). Dolomite typically exhibits a slower reaction rate compared to calcites (Khalid et al., 2015; Lund et al., 1973), consequently resulting in lower concentrations of $Ca^{2+}$ and $Mg^{2+}$ compared to the carbonate samples.

$$CaMg(CO_3)_{2(s)} + 4H^+{}_{(aq)} \longleftrightarrow Ca^{2+}{}_{(aq)} + Mg^{2+}{}_{(aq)} + 2H_2O_{(l)} + 2CO_{2(g)} \tag{6}$$

For the case of BB and SC, where there are no significant carbonate minerals in the rock composition (Table 1), small amounts of Mg-enriched calcite have been found as cementing agent binding the grains (Washburn et al., 2017). This minor amount of Mg-enriched calcite may not have been detectable through surface XRD analysis but still underwent a reaction with acid, thereby influencing the petrophysical properties. However, further investigation is warranted including conducting a bulk XRD scan (performed on a powder) rather than a surface XRD.

## 3.5 Flow Regime Analysis

The dimensionless time and height were plotted to observe the flow regime changes during capillary rise experiment and are present in the Appendix B. The red line (steep gradient) and blue line (gentle gradient) in Figures B1 and B2 show the fit experimental data based on the Quéré and Lucas-Washburn equations respectively plotted in dimensionless height and time (Eq. 4). The intersection of these two lines indicates the transition of the flow regime from inertial to viscous flow, called the intercept time. As the effect of acid imbibition, the intercept time in post-reaction water capillary rise was significantly changed throughout the samples.

The acid imbibition process exhibited distinct behavior compared to water imbibition, reflected in the changes in intercept time (Table 4). In carbonates, variations were observed in both higher and lower pH. At lower pH, the viscous flow regime occurred earlier in IL100 and IL2, while in AU, it occurred later. Conversely, at higher pH, the viscous flow regime happened earlier for AU and IL2, while for IL100, it occurred later. There is no clear correlation between the pH and the intercept time. In IL2, the changes were minimal in higher pH, and larger in lower pH. For the other samples, distinct behavior was observed between higher and lower pH, making it inconclusive.

In sandstones, the results were more consistent, consistently showing a reduction in the intercept time for acid imbibition compared to the pre-reaction water imbibition. This

**Table 4.** The time interception of the dimensionless analysis to determine the flow regime. The interception time represents the transition time from the purely inertial to the purely viscous flow regime as explained in Pratama and Khan (2024).

| Sample Name | pH | Intercept Time ($t_{int}$ (s)) | | |
|---|---|---|---|---|
| | | Pre- | Acid | Post- |
| **AU** | 2 | 288 | 328 | 287 |
| | 4 | 360 | 357 | 304 |
| **IL100** | 2 | 33 | 26 | 29 |
| | 4 | 133 | 289 | 220 |
| **IL2** | 2 | 85 | 59 | 51 |
| | 4 | 33 | 27 | 33 |
| **SC** | 2 | 48 | 33 | 35 |
| | 4 | 60 | 20 | 51 |
| **BB** | 2 | 304 | 303 | 283 |
| | 4 | 309 | 183 | 111 |
| **BG** | 2 | 52 | 38 | 25 |
| | 4 | 23 | 18 | 14 |

indicates an earlier onset of the viscous flow regime. In SC and BB the changes in the intercept time were more substantial in higher pH. Conversely, in BG, a lower pH resulted in a larger difference in intercept time.

The acid also affects the flow regime of post-acid water capillary rise and decreases the time of the inertial flow regime. It is consistently observed that for the carbonate, at lower pH, the transition from viscous to inertial flow is decreased between the pre- and post-reaction experiment (Table 4). At higher pH levels, subtle variations in the intercept time were observed: reduction in AU, increment in IL100, and no change in IL2.

In sandstones, the observed reduction in intercept time was consistently noted. Yet, there's a subtle variation in the correlation between pH and intercept time. In SC and BG, larger changes in intercept time occurred in lower pH conditions, while in higher pH, these changes were smaller. Conversely, for BB, the trend was opposite, displaying larger changes in intercept time in higher pH and smaller changes in lower pH.

The results suggest that in sandstones, the impact of the acid is more consistent, resulting in an earlier onset of the viscous flow regime. However, for carbonates, the situation is more intricate, and the results are inconclusive. This could indicate that the methodology proposed by Fries and Dreyer (2008b) is more suitable for less complex systems like sandstones, where the reaction is minimal, as opposed to more complex systems characterized by continuous alterations in petrophysical properties, such as carbonates. Thus, it is important to introduce a new methodology to incorporate this problem.

The nature of flow regimes plays a crucial role in highlighting the limitations of the Tsunazawa et al. (2016) model. This model, akin to the L-W model, overlooks inertial and viscous forces in capillary rise dynamics. The interplay between fluid inertia, capillary force, fluid weight, and resisting viscous forces governs capillary rise dynamics (Shardt et al., 2014). These forces can induce oscillations in the capillary front during the rise process (Quéré et al., 1999). Previous research has also recognized the emergence of two distinct fronts, namely the fluid and particle fronts, as an outcome of these forces influencing dynamic capillary rise behavior (Das et al., 2012; Das and Mitra, 2013; Bhaduri et al., 2014).

## 3.6 Comprehensive discussion

The reactive capillary rise exhibits a distinct profile in comparison with the capillary rise profile observed with neutral fluid. This disparity arises from the interaction between the fluids and the rock's mineral surfaces. Referred to as the coupled hydro-chemical process, this phenomenon during reactive capillary rise is depicted in Figure 10. Initially, the petrophysical properties of porous materials, in conjunction with the fluid characteristics, determine the capillary rise profile, encompassing factors like the maximum capillary height and the capillary rate.

However, during the reactive capillary rise process, chemical reactions occur within the porous media, leading to alterations in both the petrophysical properties and the fluid characteristics. The impact of acidic capillary rise on pore sizes, wettability, and tortuosity has been discussed in the previous sections and these alterations induce changes in the capillary rise profile. Coupled with the reactivity, a cyclic process is initiated that con-

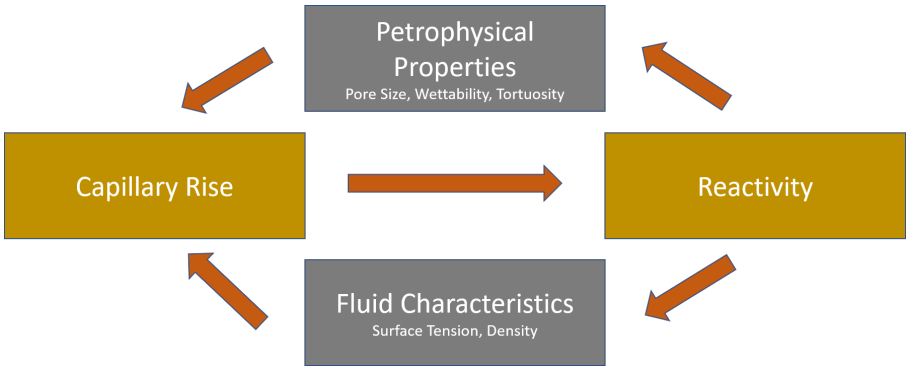


**Figure 10.** The cycle of coupled hydro-chemical processes during reactive capillary rise.

tinues indefinitely unless one of the processes (reaction or capillary-induced movement) halts: either when the capillary height reaches its maximum theoretical limit or when the fluids ceases to react. All of these alterations in petrophysical properties undoubtedly impact the capillary height and align closely with the experimental observations and measurements. This relationship between wettability, pore sizes, and capillary height is evident in Equations 1 and 3a.

A rough estimate for the Damköhler number can be determined for the calcite dissolution reaction in the sandstone and calcite samples. Since the capillary height varies between 10 and 30 mm for all the rock samples in 800 seconds of imbibition (Figures 2 and 3), the hydraulic residence time can be calculated between 2000 s and 6000 s. Considering a first order reaction with a reaction rate of $10^{-6}$ mol/m$^2$/s, the Damköhler number can be estimated to be between $2 - 6\times10^{-3}$. This indicates that all of the fluid is not reacted instantly and the reactive fluid packet imbibes deeper inside the rock where it can further react. Therefore the reaction profile is expected to show spatial dependence, with the maximum change expected near the fluid-rock interface. This was observed using micro-CT scanning in Pratama and Khan (2024).

Distinct behaviors were observed between sandstones and carbonates, particularly under varying pH conditions. In carbonates with a pH of 2, generally a slower capillary rate was observed at early times before gradually accelerating (Figure 2). In comparison, the neutral pH 7 fluid generally showed a quicker capillary rise initially which then gradually slows down. The initial deceleration in pH 2 suggests an enlargement in pore size during the early stages, followed by a reduction in pore size in the latter stages. This observation is also evident from the NMR which shows simultaneous dissolution and precipitation in

different pore sizes (Figure 6). This indicates a trend where mineral dissolution predominantly occurs in the lower part of the rock while mineral precipitation takes place in the upper part. Additionally, wettability significantly influences capillary height. The reduction in contact angle corresponds to an increased capillary height.

At higher pH levels (pH 4), the increase in capillary height is relatively slower due to less pronounced changes in the petrophysical properties compared to the more acidic pH 2 conditions. Moreover, the pore size distribution notably shifts towards the left (Figure 6), suggesting a more pronounced precipitation compared to lower pH levels. Despite this, the overall bulk porosity values after the acidic imbibition remain higher (Table 2) indicating that dissolution is still more prominent than precipitation. Additionally, the contact angle exhibits inconsistent behavior, albeit with changes that remain lower than those observed at lower pH levels.

Conversely in sandstones, the capillary height for both acidic fluids (pH 2 and pH 4) was observed to be lower compared to pH 7 (Figure 4). At the lower pH, the pore size distribution shifted towards the left (Figure 7) indicating pore reduction. However, an increase in the overall bulk porosity was noted (Table 2). It is noteworthy to emphasize that the predominant reaction observed was caclite cement dissolution. This process can potentially lead to the loosening of grains, thereby promoting fines migration. Such a phenomenon could also significantly alter the structure of the pore network, however no current observation has been made of this phenomenon. Coupled with the increase in contact angle, these changes likely contributed to the reduction in capillary height.

At the higher pH level (pH 4), a more pronounced reduction in capillary height was observed in BB and BG, while SC showed a lower reduction (Figure 3). Interestingly, the pore size distribution exhibited distinct characteristics compared to lower pH levels; it shifted towards the right (Figure 7), indicating pore enlargement. Correspondingly, there was an increase in bulk porosity, supporting the observed pore enlargement (Table 2). While evidence of grain dissolution within the sandstones was scarce, the dissolution of calcite cements, similar to the lower pH, was evident. However, this dissolution wasn't as pronounced as in lower pH conditions (Figure 9b) and potentially will not be substantial enough to loosen the grains for fines migration. When considering this observation alongside the increase in contact angle, it aligns with and supports the reduction in capillary

height.

# 4 Conclusion

The investigation into reactive fluid transport within porous media underscores the pivotal role of capillary interactions in shaping fluid behavior. The interplay between reactive fluids and the mineral composition within the pore system is paramount, provoking alterations in petrophysical properties and influencing capillary rise behavior.

In examining the distinct capillary rise profiles exhibited by acidic fluids in carbonates and sandstones, it became evident that the final capillary height and the nature of alterations in capillary behavior vary significantly based on the rock type and pH levels. In carbonates, the final capillary height is higher, while in sandstones, it is lower. Notably, in carbonates, these changes are more pronounced at lower pH levels, whereas in sandstones, higher pH levels demonstrate more significant alterations.

The reactions between acidic fluids and minerals induce shifts in petrophysical properties, especially porosity, pore size distribution, and permeability. Notably, in carbonates, dissolution, and precipitation of calcite with some magnesium impurities processes dynamically alter porosity and pore size distribution, with dissolution being more prominent at lower pH conditions. Sandstones, on the other hand, displayed dissolution primarily in Mg-enriched calcite, influencing pore size distribution and permeability, with notable variations in wettability across different pH conditions.

Furthermore, the impact of acid imbibition on the transition from inertial to viscous flow varied across rock types. Carbonates exhibited inconsistencies in correlating pH levels with intercept time, indicating complexity in the relationship between fluid reactivity and flow behavior. Conversely, sandstones displayed a more uniform response, showcasing an earlier onset of the viscous flow regime across different pH conditions.

This study highlights the often-overlooked connection between capillary interactions and fluid reactivity, emphasizing the significance of understanding the interplay between fluids and porous materials in reactive fluid transport within porous media. While conducted at

a core-scale and within short time frames, this research serves as a critical demonstration of the substantial influence of reactivity on reactive imbibition.

In conclusion, this research signifies a crucial step forward in unraveling the complexities of reactive fluid transport in porous media, advocating for further explorations at larger scales and extended durations to comprehensively understand the implications and applications of these findings across diverse fields of study and industrial practices.

# Data availability

All the data generated during this study was obtained at the Center of Integrative Petroleum Research at King Fahd University of Petroleum and Minerals (Saudi Arabia) and can be accessed at Pratama and Khan (2024). The imaging data was processed using MATLAB (Matlab, 2022) and Fiji (Schindelin et al., 2012). The figures in the manuscript are generated using PGFplots (Feuersänger, 2018).

# References


M. R. Hall and D. Allinson. 1 - Heat and mass transport processes in building materials. In Matthew R. Hall, editor, *Materials for Energy Efficiency and Thermal Comfort in Buildings*, Woodhead Publishing Series in Energy, pages 3–53. Woodhead Publishing, January 2010. ISBN 978-1-84569-526-2. doi: 10.1533/9781845699277.1.3. URL https://www.sciencedirect.com/science/article/pii/B9781845695262500013.

N. Lu and W. J. Likos. Rate of Capillary Rise in Soil. *Journal of Geotechnical and Geoenvironmental Engineering*, 130(6):646–650, June 2004. ISSN 1090-0241. doi: 10.1061/(ASCE)1090-0241(2004)130:6(646). URL https://ascelibrary.org/doi/10.1061/%28ASCE%291090-0241%282004%29130%3A6%28646%29. Publisher: American Society of Civil Engineers.

H. Dehghanpour, Q. Lan, Y. Saeed, H. Fei, and Z. Qi. Spontaneous Imbibition of Brine and Oil in Gas Shales: Effect of Water Adsorption and Resulting Microfractures. *Energy & Fuels*, 27(6):3039–3049, June 2013. ISSN 0887-0624. doi: 10.1021/ef4002814. URL https://doi.org/10.1021/ef4002814. Publisher: American Chemical Society.

Abdul Salam Abd, Elsiddig Elhafyan, Abdul Rafey Siddiqui, Wajdi Alnoush, Martin J. Blunt, and Nayef Alyafei. A review of the phenomenon of counter-current spontaneous imbibition: Analysis and data interpretation. *Journal of Petroleum Science and Engineering*, 180: 456–470, September 2019. ISSN 0920-4105. doi: 10.1016/j.petrol.2019.05.066. URL https://www.sciencedirect.com/science/article/pii/S0920410519305200.

Yan Zhou, Wei Guan, Changming Zhao, Xiaojing Zou, Zhennan He, and Hongyang Zhao. Spontaneous imbibition behavior in porous media with various hydraulic fracture propagations: A pore-scale perspective. *Advances in Geo-Energy Research*, 9(3):185–197, 2023. doi: 10.46690/ager.2023.09.06. URL https://www.sciopen.com/article/10.46690/ager.2023.09.06.

Kristopher L. Kuhlman, Melissa M. Mills, Jason E. Heath, Matthew J. Paul, Jennifer E. Wilson, and John Eric Bower. Parameter estimation from spontaneous imbibition into volcanic tuff. *Vadose Zone Journal*, 21(2):e20188, 2022. ISSN 1539-1663. doi: 10.1002/vzj2.20188. URL https://onlinelibrary.wiley.com/doi/abs/10.1002/vzj2.20188. _eprint: https://onlinelibrary.wiley.com/doi/pdf/10.1002/vzj2.20188.

Christopher Zahasky and Sally M. Benson. Preferential Solute Transport in Low Permeability Zones During Spontaneous Imbibition in Heterogeneous Porous Media. *Water Resources Research*, 58(1):e2020WR029460, 2022. ISSN 1944-7973. doi: 10.1029/2020WR029460. URL https://onlinelibrary.wiley.com/doi/abs/10.1029/2020WR029460. _eprint: https://onlinelibrary.wiley.com/doi/pdf/10.1029/2020WR029460.

Christopher Zahasky and Sally M. Benson. Spatial and Temporal Quantification of Spontaneous Imbibition. *Geophysical Research Letters*, 46 (21):11972–11982, 2019. ISSN 1944-8007. doi: 10.1029/2019GL084532. URL https://onlinelibrary.wiley.com/doi/abs/10.1029/2019GL084532. _eprint: https://onlinelibrary.wiley.com/doi/pdf/10.1029/2019GL084532.

Amir H. Haghi, Richard Chalaturnyk, Martin J. Blunt, Kevin Hodder, and Sebastian Geiger. Poromechanical controls on spontaneous imbibition in earth materials. *Scientific Reports*, 11(1):3328, February 2021. ISSN 2045-2322. doi: 10.1038/s41598-021-82236-x. URL https://www.nature.com/articles/s41598-021-82236-x. Publisher: Nature Publishing Group.

Hamed Aslannejad, Alexandros Terzis, S. Majid Hassanizadeh, and Bernhard Weigand. Occurrence of temperature spikes at a wetting front during spontaneous imbibition. *Scientific Reports*, 7(1):7268, August 2017. ISSN 2045-2322. doi: 10.1038/s41598-017-07528-7. URL https://www.nature.com/articles/s41598-017-07528-7. Publisher: Nature Publishing Group.

X. Yin, H. Aslannejad, E. T. de Vries, A. Raoof, and S. M. Hassanizadeh. Droplet Imbibition into Paper Coating Layer: Pore-Network Modeling Simulation. *Transport in Porous Media*, 125(2):239–258, November 2018. ISSN 1573-1634. doi: 10.1007/s11242-018-1116-0. URL https://doi.org/10.1007/s11242-018-1116-0.

Geoffrey Mason and Norman R Morrow. Developments in spontaneous imbibition and possibilities for future work. *Journal of Petroleum Science and Engineering*, 110:268–293, 2013.

Sebnem Boduroglu and Rashid Bashir. Review of Capillary Rise Experiments for Surface-Active Solutes in the Subsurface. 2022.

Richard Lucas. Ueber das Zeitgesetz des kapillaren Aufstiegs von Flüssigkeiten. *Kolloid-Zeitschrift*, 23(1):15–22, 1918.

Edward W Washburn. The dynamics of capillary flow. *Physical review*, 17(3):273, 1921.

David Benavente, Peter Lock, M Ángeles García Del Cura, and Salvador Ordóñez. Predicting the capillary imbibition of porous rocks from microstructure. *Transport in porous media*, 49(1):59–76, 2002.

N Fries and M Dreyer. An analytic solution of capillary rise restrained by gravity. *Journal of colloid and interface science*, 320(1):259–263, 2008a.

Yuya Tsunazawa, Tadashi Yokoyama, and Naoki Nishiyama. An experimental study on the rate and mechanism of capillary rise in sandstone. *Progress in Earth and Planetary Science*, 3(1):1–10, 2016.

Yury Villagrán Zaccardi, Natalia Mariel Alderete, and Nele De Belie. Lucas-Washburn vs Richards equation for the modelling of water absorption in cementitious materials. In *5th International Conference on Concrete Repair, Rehabilitation and Retrofitting (ICCRRR)*, volume 199. EDP Sciences, 2018.

Junjie Wang, Amgad Salama, and Jisheng Kou. Experimental and numerical analysis of imbibition processes in a corrugated capillary tube. *Capillarity*, 5(5):83–90, 2022. doi: 10.46690/capi.2022.05.01. URL https://www.sciopen.com/article/10.46690/capi.2022.05.01.

Wenjia Fan, Kim F. Hayes, and Brian R. Ellis. Estimating Radium Activity in Shale Gas Produced Brine. *Environmental Science & Technology*, 52(18):10839–10847, September 2018. ISSN 0013-936X, 1520-5851. doi: 10.1021/acs.est.8b01587. URL https://pubs.acs.org/doi/10.1021/acs.est.8b01587.

Pascale. Vachon, Rajeshwar D. Tyagi, Jean Christian. Auclair, and Kevin J. Wilkinson. Chemical and biological leaching of aluminum from red mud. *Environmental Science & Technology*, 28(1):26–30, January 1994. ISSN 0013-936X, 1520-5851. doi: 10.1021/es00050a005. URL https://pubs.acs.org/doi/abs/10.1021/es00050a005.

Balasubrahmanyam Avvaru, S. B. Roy, Yogesh Ladola, Sujit Chowdhury, K. N. Hareendran, and Aniruddha B. Pandit. Sono-chemical leaching of uranium. *Chemical Engineering and Processing: Process Intensification*, 47(12):2107–2113, November 2008. ISSN 0255-2701. doi: 10.1016/j.cep.2007.10.021. URL https://www.sciencedirect.com/science/article/pii/S0255270107003583.

Suresh K. Bhargava, Rahul Ram, Mark Pownceby, Stephen Grocott, Bob Ring, James Tardio, and Lathe Jones. A review of acid leaching of uraninite. *Hydrometallurgy*, 151:10–24, January 2015. ISSN 0304-386X. doi: 10.1016/j.hydromet.2014.10.015. URL https://www.sciencedirect.com/science/article/pii/S0304386X14002308.

E. M. Córdoba, J. A. Muñoz, M. L. Blázquez, F. González, and A. Ballester. Passivation of chalcopyrite during its chemical leaching with ferric ion at 68°C. *Minerals Engineering*, 22(3):229–235, February 2009. ISSN 0892-6875. doi: 10.1016/j.mineng.2008.07.004. URL

https://www.sciencedirect.com/science/article/pii/S0892687508001830.

Qingyun Li, Adam D Jew, Gordon E Brown Jr, John R Bargar, and Katharine Maher. Reactive transport modeling of shale–fluid interactions after imbibition of fracturing fluids. *Energy & Fuels*, 34(5):5511–5523, 2020.

Ginevra Di Donato and Martin J. Blunt. Streamline-based dual-porosity simulation of reactive transport and flow in fractured reservoirs. *Water Resources Research*, 40(4), 2004. ISSN 1944-7973. doi: 10.1029/2003WR002772. URL https://onlinelibrary.wiley.com/doi/abs/10.1029/2003WR002772. _eprint: https://onlinelibrary.wiley.com/doi/pdf/10.1029/2003WR002772.

Muhammad Andiva Pratama and Hasan Javed Khan. Effect of ph on spontaneous imbibition in calcareous rock. *Water Resource Research (Accepted)*, 2024. doi: 10.1029/2023WR035307.

F. Jaeger, S. Bowe, H. Van As, and G. E. Schaumann. Evaluation of 1H NMR relaxometry for the assessment of pore-size distribution in soil samples. *European Journal of Soil Science*, 60(6):1052–1064, 2009. ISSN 1365-2389. doi: 10.1111/j.1365-2389.2009.01192.x. URL https://onlinelibrary.wiley.com/doi/abs/10.1111/j.1365-2389.2009.01192.x. _eprint: https://onlinelibrary.wiley.com/doi/pdf/10.1111/j.1365-2389.2009.01192.x.

Starting Matlab. Matlab. *The MathWorks, Natick, MA*, 2022.

W.-B. Bartels, M. Rücker, M. Boone, T. Bultreys, H. Mahani, S. Berg, S. M. Hassanizadeh, and V. Cnudde. Imaging Spontaneous Imbibition in Full Darcy-Scale Samples at Pore-Scale Resolution by Fast X-ray Tomography. *Water Resources Research*, 55(8):7072–7085, 2019. ISSN 1944-7973. doi: 10.1029/2018WR024541. URL https://onlinelibrary.wiley.com/doi/abs/10.1029/2018WR024541. _eprint: https://onlinelibrary.wiley.com/doi/pdf/10.1029/2018WR024541.

Hasan J. Khan, Ayaz Mehmani, Maša Prodanović, David DiCarlo, and Dayeed J. Khan. Capillary rise in vuggy media. *Advances in Water Resources*, 143:103671, September 2020. ISSN 0309-1708. doi: 10.1016/j.advwatres.2020.103671. URL https://www.sciencedirect.com/science/article/pii/S0309170820303699.

D Quéré. Inertial capillarity. *Europhysics Letters (EPL)*, 39(5):533–538, September 1997. ISSN 0295-5075, 1286-4854. doi: 10.1209/epl/i1997-00389-2. URL https://iopscience.iop.org/article/10.1209/epl/i1997-00389-2.

Naoki Ichikawa and Yoko Satoda. Interface Dynamics of Capillary Flow in a Tube under Negligible Gravity Condition. *Journal of Colloid and Interface Science*, 162(2):350–355, February 1994. ISSN 00219797. doi: 10.1006/jcis.1994.1049. URL https://linkinghub.elsevier.com/retrieve/pii/S0021979784710496.

Lateef Owolabi Lawal, Abdulrauf R. Adebayo, Mohamed Mahmoud, Ben Mansour Dia, and Abdullah S. Sultan. A novel NMR surface relaxivity measurements on rock cuttings for conventional and unconventional reservoirs. *International Journal of Coal Geology*, 231:103605, November 2020. ISSN 0166-5162. doi: 10.1016/j.coal.2020.103605. URL https://www.sciencedirect.com/science/article/pii/S0166516220306017.

Francisco Benavides, Ricardo Leiderman, Andre Souza, Giovanna Carneiro, and Rodrigo Bagueira de Vasconcellos Azeredo. Pore size distribution from NMR and image based methods: A comparative study. *Journal of Petroleum Science and Engineering*, 184:106321, January 2020. ISSN 0920-4105. doi: 10.1016/j.petrol.2019.106321. URL https://www.sciencedirect.com/science/article/pii/S0920410519307429.

Jonathan Mitchell and Edmund J. Fordham. Contributed Review: Nuclear magnetic resonance core analysis at 0.3 T. *Review of Scientific Instruments*, 85(11):111502, November 2014. ISSN 0034-6748. doi: 10.1063/1.4902093. URL https://doi.org/10.1063/1.4902093.

Everton Lucas-Oliveira, Arthur G. Araujo-Ferreira, Willian A. Trevizan, Bernardo Coutinho C. dos Santos, and Tito J. Bonagamba. Sandstone surface relaxivity determined by NMR T2 distribution and digital rock simulation for permeability evaluation. *Journal of Petroleum Science and Engineering*, 193:107400, October 2020. ISSN 0920-4105. doi: 10.1016/j.petrol.2020.107400. URL https://www.sciencedirect.com/science/article/pii/S0920410520304721.

Dag C Standnes and Tor Austad. Wettability alteration in carbonates. *Colloids and Surfaces A: Physicochemical and Engineering Aspects*, 216(1-3):243–259, April 2003. ISSN 09277757. doi: 10.1016/S0927-7757(02)00580-0. URL https://linkinghub.elsevier.com/retrieve/pii/S0927775702005800.

K. A. Rezaei Gomari and A. A. Hamouda. Effect of fatty acids, water composition and pH on the wettability alteration of calcite surface. *Journal of Petroleum Science and Engineering*, 50(2):140–150, February 2006. ISSN 0920-4105. doi: 10.1016/j.petrol.2005.10.007. URL https://www.sciencedirect.com/science/article/pii/S0920410505001671.

W W Owens and D L Archer. The Effect of Rock Wettability on Oil- Water Relative Permeability Relationships. *JOURNAL OF PETROLEUM TECHNOLOGY*, 1971.

Jianchao Cai, Tingxu Jin, Jisheng Kou, Shuangmei Zou, Junfeng Xiao, and Qingbang Meng. Lucas–Washburn equation-based modeling of capillary-driven flow in porous systems. *Langmuir*, 37(5):1623–1636, 2021.

Jorge J. Moré. The Levenberg-Marquardt algorithm: Implementation and theory. In G. A. Watson, editor, *Numerical Analysis*, pages 105–116, Berlin, Heidelberg, 1978. Springer Berlin Heidelberg. ISBN 978-3-540-35972-2.

Marwan Alkattan, Eric H Oelkers, Jean-Louis Dandurand, and Jacques Schott. An experimental study of calcite and limestone dissolution rates as a function of pH from −1 to 3 and temperature from 25 to 80°C. *Chemical Geology*, 151(1-4):199–214, October 1998. ISSN 00092541. doi: 10.1016/S0009-2541(98)00080-1. URL https://linkinghub.elsevier.com/retrieve/pii/S0009254198000801.

Marwan Alkattan, Eric H Oelkers, Jean-Louis Dandurand, and Jacques Schott. An experimental study of calcite dissolution rates at acidic conditions and 25 °C in the presence of NaPO3 and MgCl2. *Chemical Geology*, 190(1):291–302, October 2002. ISSN 0009-2541. doi: 10.1016/S0009-2541(02)00121-3. URL https://www.sciencedirect.com/science/article/pii/S0009254102001213.

Ahmed I. Rabie, Ahmed M. Gomaa, and Hisham A. Nasr-El-Din. Reaction of In-Situ-Gelled Acids With Calcite: Reaction-Rate Study. *SPE Journal*, 16(04):981–992, July 2011. ISSN 1086-055X. doi: 10.2118/133501-PA. URL https://doi.org/10.2118/133501-PA.

F. Gray, B. Anabaraonye, S. Shah, E. Boek, and J. Crawshaw. Chemical mechanisms of dissolution of calcite by HCl in porous media: Simulations and experiment. *Advances in Water Resources*, 121:369–387, November 2018. ISSN 0309-1708. doi: 10.1016/j.advwatres.2018.09.007. URL https://www.sciencedirect.com/science/article/pii/S0309170818303713.

Lauri Järvinen, Jarkko Albert Leiro, Frej Bjondahl, Claudio Carletti, and Olav Eklund. XPS and SEM study of calcite bearing rock powders in the case of reactivity measurement with HCl solution: XPS and SEM study of calcite bearing rock powders in the case of HCl. *Surface and Interface Analysis*, 44(5):519–528, May 2012. ISSN 01422421. doi: 10.1002/sia.3838. URL https://onlinelibrary.wiley.com/doi/10.1002/sia.3838.

Kamaljit Singh, Benaiah U. Anabaraonye, Martin J. Blunt, and John Crawshaw. Partial dissolution of carbonate rock grains during reactive CO2-saturated brine injection under reservoir conditions. *Advances in Water Resources*, 122:27–36, December 2018. ISSN 03091708. doi:

10.1016/j.advwatres.2018.09.005. URL https://linkinghub.elsevier.com/retrieve/pii/S0309170818305311.

Sanni Eloneva, Sebastian Teir, Justin Salminen, Carl-Johan Fogelholm, and Ron Zevenhoven. Steel Converter Slag as a Raw Material for Precipitation of Pure Calcium Carbonate. *Industrial & Engineering Chemistry Research*, 47(18):7104–7111, September 2008. ISSN 0888-5885, 1520-5045. doi: 10.1021/ie8004034. URL https://pubs.acs.org/doi/10.1021/ie8004034.

Muhammad Ali Khalid, Abdullah Sultan, and Xiangdong Qiu. Revisiting Reaction Kinetics and Diffusion Rate of Dolomitic Rock with HCl. OnePetro, September 2015. doi: 10.2118/175832-MS. URL https://dx.doi.org/10.2118/175832-MS.

Kasper Lund, H. Scott Fogler, and C. C. McCune. Acidization—I. The dissolution of dolomite in hydrochloric acid. *Chemical Engineering Science*, 28(3):691–IN1, March 1973. ISSN 0009-2509. doi: 10.1016/0009-2509(77)80003-1. URL https://www.sciencedirect.com/science/article/pii/0009250977800031.

Kathryn E. Washburn, Magdalena Sandor, and Yuesheng Cheng. Evaluation of sandstone surface relaxivity using laser-induced breakdown spectroscopy. *Journal of Magnetic Resonance*, 275:80–89, February 2017. ISSN 1090-7807. doi: 10.1016/j.jmr.2016.12.004. URL https://www.sciencedirect.com/science/article/pii/S1090780716302580.

N. Fries and M. Dreyer. The transition from inertial to viscous flow in capillary rise. *Journal of Colloid and Interface Science*, 327(1):125–128, November 2008b. ISSN 00219797. doi: 10.1016/j.jcis.2008.08.018. URL https://linkinghub.elsevier.com/retrieve/pii/S0021979708009661.

Orest Shardt, Prashant R Waghmare, JJ Derksen, and Sushanta K Mitra. Inertial rise in short capillary tubes. *Rsc Advances*, 4(28): 14781–14785, 2014.

David Quéré, Elie Raphael, and Jean-Yves Ollitrault. Rebounds in a capillary tube. *Langmuir*, 15(10):3679–3682, 1999.

Siddhartha Das, Prashant R Waghmare, and Sushanta K Mitra. Early regimes of capillary filling. *Physical Review E*, 86(6):067301, 2012.

Siddhartha Das and Sushanta K Mitra. Different regimes in vertical capillary filling. *Physical Review E*, 87(6):063005, 2013.

Swayamdipta Bhaduri, Pankaj Sahu, Siddhartha Das, Aloke Kumar, and Sushanta K Mitra. Capillary Imbibition Dynamics in Porous Media. In *International Conference on Nanochannels, Microchannels, and Minichannels*, volume 46278, page V001T08A002. American Society of Mechanical Engineers, 2014.

Johannes Schindelin, Ignacio Arganda-Carreras, Erwin Frise, Verena Kaynig, Mark Longair, Tobias Pietzsch, Stephan Preibisch, Curtis Rueden, Stephan Saalfeld, Benjamin Schmid, et al. Fiji: an open-source platform for biological-image analysis. *Nature methods*, 9(7): 676–682, 2012.

Christian Feuersänger. Pgfplots-a la-tex package to create normal/logarithmic plots in two and three dimensions. *Zugriff unter http://pgfplots. sourceforge. net*, 2018.

# Appendix A - Fitting Accuracy

The experimental data for sandstones and carbonates under pH 2 and 4 conditions were individually fit using three distinct, established equations: the Tsunazawa et al. (2016) model, the Lucas-Washburn equation (Washburn, 1921), and the Quéré equation (Quéré, 1997). One of the fitting process is depicted in Figure A1. The fitting accuracy, as assessed by the $R^2$ Score, is presented in Table A1. The results indicate that Tsunazawa's models generally exhibit superior accuracy across most cases. However, there are instances where the correlation does not follow a logarithmic trend, and the linear correlation (Quéré model) demonstrates better accuracy.

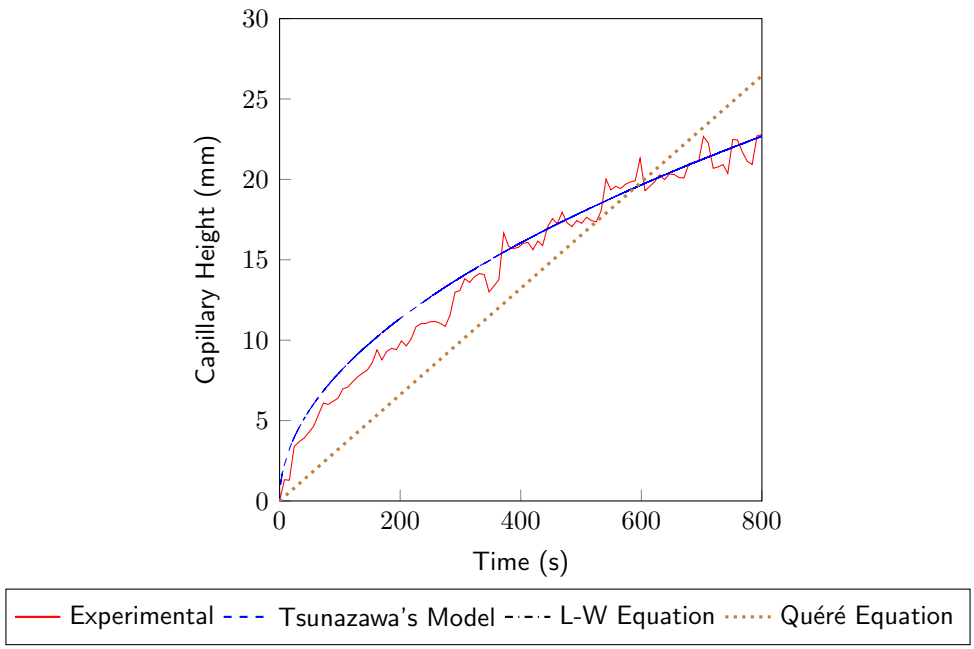


**Figure A1.** An example of the result of fitting the experimental data to the Tsunazawa, Lucas-Washburn, and Quéré model. The data used in this graph was based on water pre-reaction capillary rise of AU sample used in pH 2 acidic capillary rise.

**Table A1.** The $R^2$ Score of fitting Tsunazawa, Lucas-Washburn, and Quéré model. The underlined number shows the best model with the highest $R^2$ values.

| Sample Name | pH | Exp | $R^2$ Score | | |
|---|---|---|---|---|---|
| | | | **Tsunazawa** | **L-W** | **Quéré** |
| **AU** | **2** | Pre- | 1.000 | 0.971 | 0.803 |
| | | Acid | 0.930 | 0.924 | 0.952 |
| | | Post- | 0.978 | 0.969 | 0.852 |
| | **4** | Pre- | 0.986 | 0.985 | 0.904 |
| | | Acid | 0.860 | 0.859 | 0.899 |
| | | Post- | 0.889 | 0.888 | 0.972 |
| **IL100** | **2** | Pre- | 1.000 | 0.883 | 0.926 |
| | | Acid | 0.999 | 0.965 | 0.669 |
| | | Post- | 0.941 | 0.959 | 0.821 |
| | **4** | Pre- | 0.963 | 0.962 | 0.865 |
| | | Acid | 0.951 | 0.951 | 0.919 |
| | | Post- | 0.951 | 0.951 | 0.937 |
| **IL2** | **2** | Pre- | 1.000 | 0.997 | 0.681 |
| | | Acid | 0.967 | 0.962 | 0.891 |
| | | Post- | 0.949 | 0.933 | 0.945 |
| | **4** | Pre- | 0.862 | 0.837 | 0.665 |
| | | Acid | 0.871 | 0.831 | 0.838 |
| | | Post- | 0.988 | 0.900 | 0.840 |
| **SC** | **2** | Pre- | 0.887 | 0.490 | 0.932 |
| | | Acid | 0.962 | 0.899 | 0.916 |
| | | Post- | 0.983 | 0.950 | 0.895 |
| | **4** | Pre- | 0.954 | 0.364 | 0.946 |
| | | Acid | 0.944 | 0.621 | 0.928 |
| | | Post- | 0.927 | 0.191 | 0.955 |
| **BB** | **2** | Pre- | 0.989 | 0.988 | 0.900 |
| | | Acid | 0.914 | 0.913 | 0.975 |
| | | Post- | 0.943 | 0.858 | 0.954 |
| | **4** | Pre- | 0.987 | 0.984 | 0.906 |
| | | Acid | 0.963 | 0.924 | 0.936 |
| | | Post- | 0.951 | 0.942 | 0.926 |
| **BG** | **2** | Pre- | 0.967 | 0.590 | 0.896 |
| | | Acid | 0.971 | 0.926 | 0.839 |
| | | Post- | 0.989 | 0.833 | 0.815 |
| | **4** | Pre- | 0.967 | 0.830 | 0.884 |
| | | Acid | 0.869 | 0.600 | 0.907 |
| | | Post- | 0.976 | 0.811 | 0.840 |

# Appendix B - Flow Regime

The dimensionless time and height were graphed to observe changes in flow regimes during the capillary rise experiment. Figure B1 and B2 display the dimensionless time and height plots for pH 2 and 4, respectively. These plots depict the experimental data fitted with the Quéré (red line with a steep gradient) and Lucas-Washburn (blue line with a gentle gradient) equations, showcasing the transition from inertial to viscous flow—a crucial point identified as the intercept time where these lines intersect. Notably, the impact of acid imbibition significantly altered the intercept time during post-reaction water capillary rise across the samples.

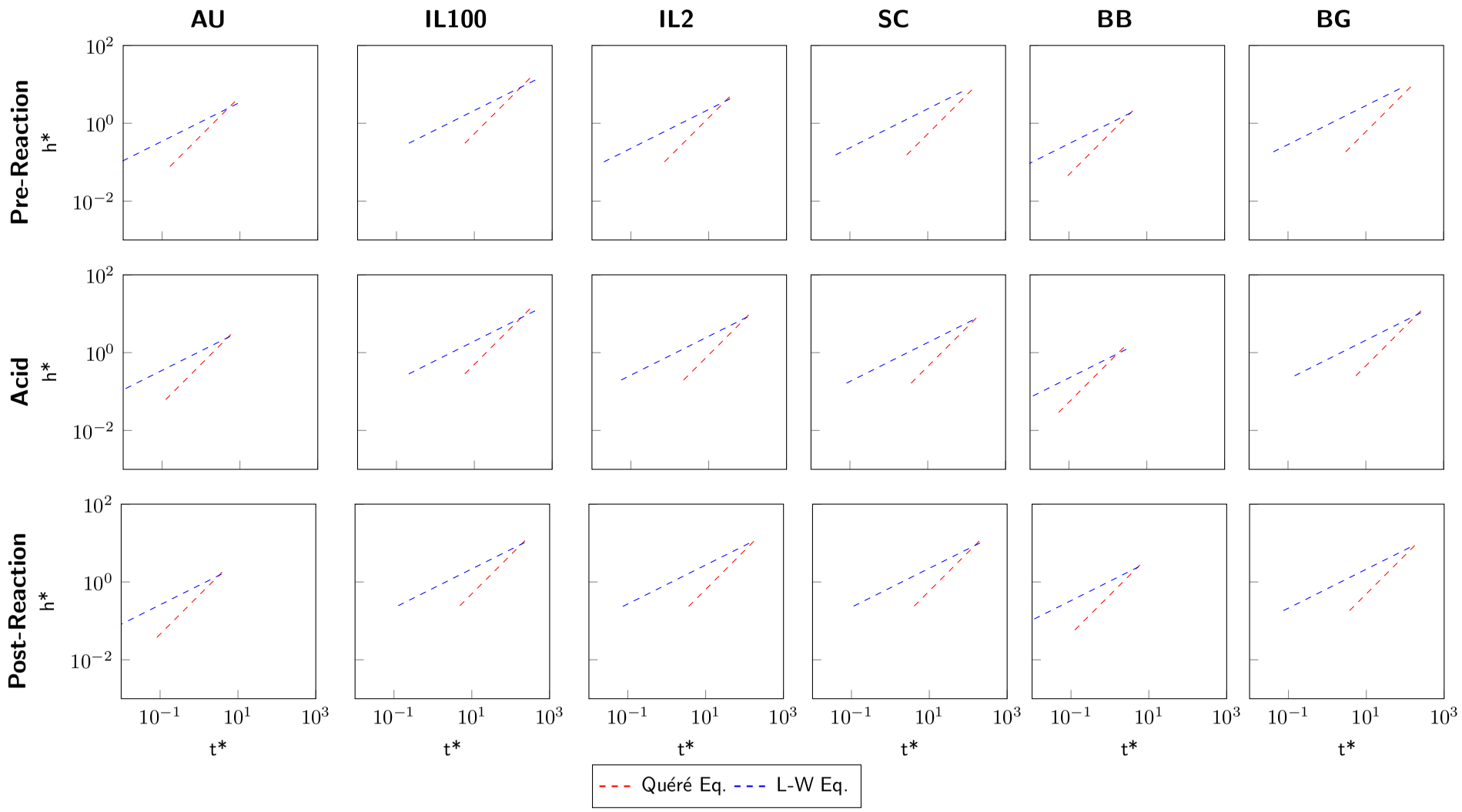


**Figure B1.** The dimensionless height and time for each sample based on the Quéré (1997) and Washburn (1921) equation and using the dimensionless formula from Ichikawa and Satoda (1994) for pH 2. The intersection between two lines indicates the transition from the purely inertial to viscous flow regime and is presented in time units.

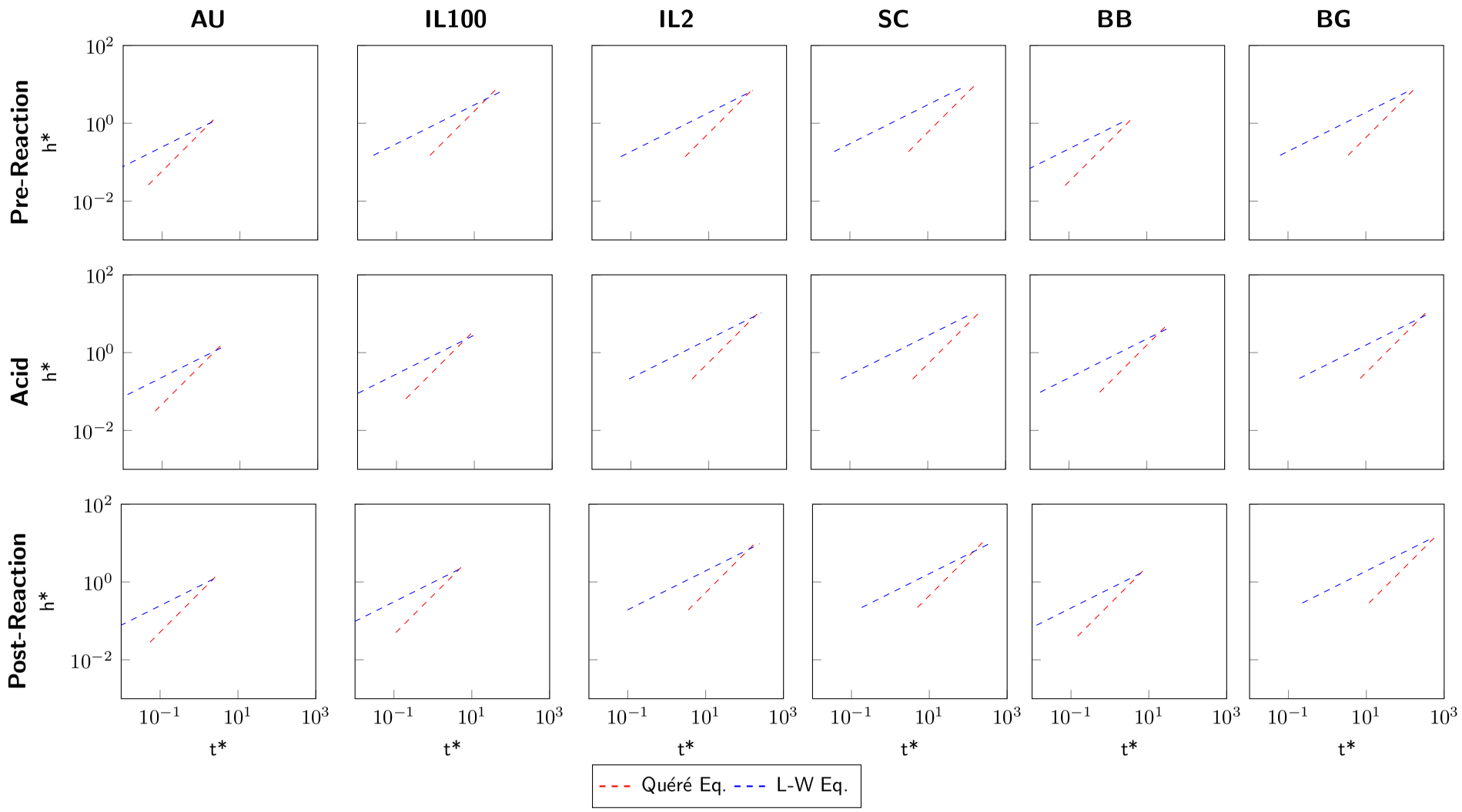


**Figure B2.** The dimensionless height and time for each sample based on the Quéré (1997) and Washburn (1921) equation and using the dimensionless formula from Ichikawa and Satoda (1994) for pH 4. The intersection between two lines indicates the transition from the purely inertial to viscous flow regime and is presented in time units.